Western Australian School of Mines: Minerals, Energy and Chemical Engineering

Feasibility of Multi-component Seismic for Mineral Exploration

Pouya Ahmadi

This thesis is presented for the Degree of
Doctor of Philosophy
of
Curtin University

December 2018

Declaration

To the best of my knowledge and belief, this thesis contains no material previously published by any other person except where due acknowledgement has been made.

This thesis contains no material, which has been accepted for the award of any other degree or diploma in any university.

Signature: ……Ranya Ahmadi……

Date: ……07/12/2018……

To my wife, parents and sister.

Abstract

The mineral industry traditionally uses potential field and electrical geophysical methods to explore for subsurface mineral deposits. These methods are very effective when exploring for shallow targets. As shallow deposits are now largely depleted, alternative technologies need to be introduced to discover deeper targets or to extend known resources deeper. Only the seismic reflection method can reach the desired depths as well as provide the high-definition images of the subsurface that are required. Conventional seismic reflection methods make use of only one component (vertical) of the wave field (P-wave) which is very effective in resolving complex structural shapes but less so for rock characterisation. The proposition of this work is that the utilisation of the full vector field (3 component seismic data (3C)) could provide additional information that will help in rock identification, classification and detection of subtle structures, alteration and lithological boundaries that are of crucial importance for mineral exploration. Shear wave splitting, polarisation changes and velocity differences between polarised modes have at present undefined potential in resolving lithological changes, internal composition of shear zones, subtle faults and fractured zones. However, this additional information is difficult to extract from 3C data. This study investigates different ways of shear wave analysis and utilisation for mineral exploration since no commercial approach or methodology as yet exists. The investigations presented pave the way for a routine application of multi-component (3C or more) methodologies for exploration of mineral deposits. The utilisation of the method is viewed in a commercial sense that would be acceptable to the mineral industry. The findings of the study are hoped to inspire further 3C studies and to provide a foundation for further advancement of the application of multi-component seismology in the mineral sector.

Acknowledgements

I would like to express my deepest appreciation to my supervisor, Associate Professor Dr. Milovan Urosevic, who provided me the opportunity to follow my dreams and his continuous supports, valuable advices and productive suggestions had the most impact on this thesis. A special thanks goes to him for the time he spent reviewing my thesis and providing constructive feedbacks.

I have to appreciate the rest of my supervisory panel, Professor Dr. Andrej Bóna (co-supervisor), Dr. Konstantin Tertyshnikov (co-supervisor), Mr. Louis Polomé (Industrial Supervisor) and Professor Dr. Maxim Lebedev (chair) for their support and their valuable time they have spent for me during all stages of this research work.

Besides my supervisory panel, I would like to thank Dr. Mahyar Madadi for kindly sharing his knowledge and productive discussions and suggestions. Without his technical contribution this thesis would not have been possible.

I am indebted to Mr. Aleksandar Dzunic for generously sharing his immense knowledge and experience in seismic processing. His caring, continuous support both technically and emotionally, patience, encouragement and enthusiasm toward science truly impressed me and showed me the light at the end of the tunnel. I will be grateful to be able to call him a friend.

I am profoundly grateful to Mr. David Fursman who have generously given up his valuable time reviewing my thesis and providing instructive comments and constructive feedbacks.

Very special thank goes to administrative and technical staff of the “so called” Department of Exploration Geophysics Ms. Deirdre Hollingsworth, Ms. Nichole Sik, Mr. Dominic Howman and Mr. Robert Verstandig for keeping the department alive. I would like to thank Dr Andrew Greenwood and Mr. Dominic Howman for passing their valuable experience and the great time during the field trips.

It is necessary to acknowledge the Department of Exploration Geophysics and Curtin University for financial support through a Curtin University International Postgraduate

Research Scholarship (CIPRS), purchase the licenses for necessary software and to attend workshops and conferences.

I am grateful to Halliburton Landmark (SeisSpace), Tesseral technologies (Tesserel Pro), MathWorks (MATLAB) and Department of Physics, Geophysical Institute of Karlsruhe Institute of Technology (SOFI3D) for providing software packages under their university program grants.

I want to send my gratitude to Ashley Grant and BHP Billiton for providing 3D/3C seismic data for this study. Core samples were kindly provided by Dr. Adrian Fabris (Geological Survey of South Australia) and the acoustic measurements were conducted in the rock physics laboratory by Dr. Maxim Lebedev.

This work has been supported by the Deep Exploration Technologies Cooperative Research Centre (DET CRC) whose activities are funded by the Australian Government's Cooperative Research Centre Programme.

This work was supported by resources provided by the Pawsey Supercomputing Centre with funding from the Australian Government and the Government of Western Australia.

I will always remember and appreciate all my friends, office-mates, colleagues and all the staffs of the Department of Exploration Geophysics throughout my PhD journey.

Finally, I want to express my gratitude to my beloved family, my wife Nazli Aliasghari, my mother Khadijeh Babaki Rad, my father Ghahraman Ahmadi and my sister Roja Ahmadi for their understanding, their endless love and encouragement in my life specially during past few years.

Table of Contents

List of Figures

List of Tables

List of Abbreviations

2D	Two Dimensional
3C	Three Component
3D	Three Dimensional
4C	Four Component
9C	Nine Component
ACP	Asymptotic (common) Conversion Point
AGC	Automatic gain control
ASEG	Australian Society of Exploration Geophysicists
AVO	Amplitude Versus Offset
BHP	Broken Hill Propriety Company Ltd
BP	Band-Pass
BR	Bittali Rhyolite
C-wave	Converted-wave
CBM	Coal Bed Methane
CCP	Common Conversion Point
CDP	Common Depth Point
CMP	Common Mid-Point
CREWES	Consortium for Research in Elastic Wave Exploration Seismology
Cu	Copper
CVS	Constant Velocity Stack
DEG	Department of Exploration Geophysics
DET CRC	Deep Exploration Technologies Cooperative Research Centre
DMO	Dip Move-Out
EM	ElectroMagnetic
ER	Eucarro Rhyolite
FWS	Full Waveform Sonic
GA	Geoscience Australia
GRV	Gawler Range Volcanic
GSSA	Geological Survey of South Australia
IVA	Interactive Velocity Analysis
MASW	Multichannel Analysis for Surface Waves
MD	Moonaree Dacite

MSDP	Mineral Systems Drilling Program
Ni	Nickel
NMO	Normal Move-Out
P-wave	Primary (compressional) wave
PAI	Pseudo Acoustic Inversion
PD	Pondanna Dacite
PESA	Petroleum Exploration Society of Australia
PSTM	Pre-Stack Time Migration
QC	Quality Control
RCP	Reservoir Characterization Project
RGB	Red, Green and Blue
RMS	Root Mean Square
S-wave	Secondary (shear) wave
SNR	Signal to Noise Ratio
SOFI3D	Seismic mOdeling with FInite differences
SUS	Stack-UnStack
TAR	True Amplitude Recovery
USA	United States of America
USSR	Union of Soviet Socialist Republics
VMS	Volcanogenic Massive Sulphide
VSP	Vertical Seismic Profiling
VTI	Vertically Transversely Isotropic
WA	Western Australia
WD	Waganny Dacite
YD	Yardea Dacite
Zn	Zinc

Chapter 1 Introduction

1.1 Background

The mining industry plays an important and fundamental role in the Australian economy. Discovering new mining prospects as well as expanding current productive mines significantly contibutes to the sustainable and productive growth of the industry. To achieve this, various geophysical methods has been tested and employed by the industry.

Historically, potential field (magnetics and gravity) and electrical methods (induced polarisation and electromagnetics) have been used to detect and locate possible minerilised zones and relatively shallow resources for exploration purposes. These methods are successful for shallow targets but suffer from low spatial and depth resolution. Moreover, the presence of a weathered overburden layer (regolith) often results in poor performance, particularly reduced sensitivity. A huge increase in mineral commodity prices and a decrease in discovery of new mineral deposits, has forced the industry to explore for deeper targets. Figure 1-1 shows the increase in depth of major discoveries all over the world from 1900 to 2016 (Schodde, 2017). Clearly, new techniques must be proposed to identify deeper targets. Reflection Seismic is the only surface method that can penetrate to the required depths with the required spatial and depth resolution (Malehmir et al., 2012b; Urosevic, 2013).

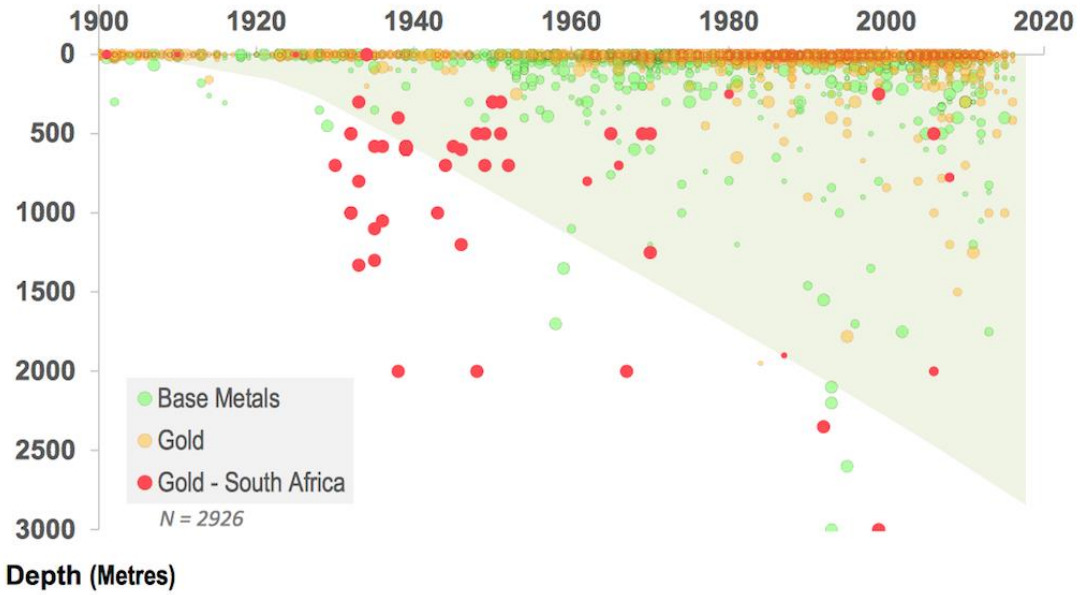

Figure 1-1 Depth of cover and year of discovery for gold and base metals. The size of the circles depicts the discovery size (moderate, major and giant) between 1900 and 2016 all over the world. This graph shows that the industry is looking deeper over time (Schodde, 2017).

The use of the reflection seismic method for exploration of minerals has been researched and documented in numerous scientific publications (Eaton et al., 2003; Malehmir et al., 2012a). Many companies have been using both 2D and 3D surface seismic for site characterisation and exploration purposes all over the world as shown in Figure 1-2 (Malehmir et al., 2012a). However, only recently have modern seismic acquisition techniques, in particular 3D seismic, been accepted and used in the mining industry to map predominantly deep structures of interest for mineral targeting. The effectiveness of the method is highly site and geology dependent (Pretorius et al., 2003; Malehmir et al., 2012a) and the frequency of application in different parts of the world varies greatly mainly due to factors such as the cost of acquisition, difficulty of processing and the difficulty of interpretation of the resulting images and the ability of the images to provide meaningful geological results. As a result, the reflection seismic method has not been a primary method used for mineral exploration within the mineral industry (Urosevic et al., 2017).

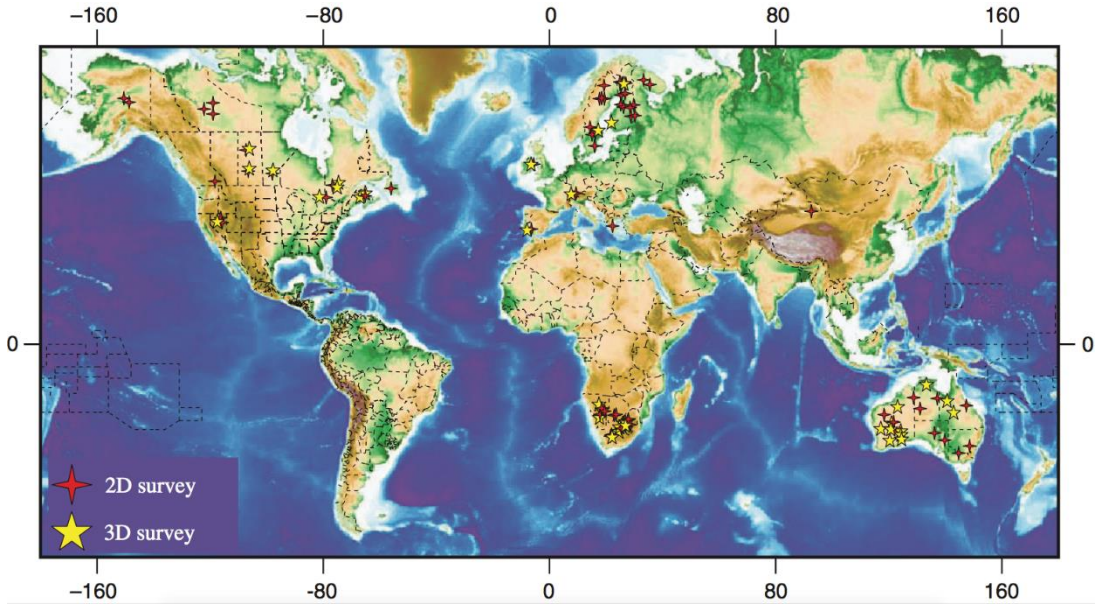

Figure 1-2 Location of 2D and 3D surface seismic surveys for site characterisation and mineral exploration purposes (Malehmir et al., 2012a).

1.2 Seismic Methods for Mineral Exploration

Historical Perspective

The reported origins of seismic go back to 1851 when Robert Mallet used a dynamite source to measure the speed of propagated waves in surface rocks (Dewey and Byerly, 1969; Prodehl and Mooney, 2012). In 1878, Ferdinand Fouquè conducted experiments to detect granites in basement (Tertyshnikov, 2014). In 1906, a significant advancement in recording instrumentation occurred when Emil Wiechert made a portable seismograph. This seismograph was used to measure and amplify signal emanating from the horizontal component of ground movements in Göttingen, Germany (Prodehl and Mooney, 2012). In 1908, Mintrop used the seismograph in combination with a weight drop source to record the first seismogram with details of P and S body waves (called precursor waves at that time) (Prodehl and Mooney, 2012). For more information, Prodehl and Mooney (2012) provide a summary of the use of controlled-source seismology to study the upper-most mantle and Earth's crust from the nineteenth century up to 2005.

Application of seismic methods applied to hard rock geology started in Russia (former USSR) dating back 1920 when they were used to investigate ore deposits near Krivoi Rog (nowadays Ukraine). In the 1940s a large-scale seismic refraction investigation of the crystalline basement was conducted (Gamburtsev et al., 1952). In mid 1950s an early attempt was made to use high-frequency seismics to map vertically layered media and investigate ore deposits (Berson, 1957).

From the mid-1950s, the use of surface, underground and/or downhole reflection seismics has been investigated and trialled over different types of mineral deposits (Schmidt, 1959; Price, 1974; Nelson, 1984; Mutyorauta, 1987; Gendzwill, 1990; Juhlin et al., 1991; Friedel et al., 1995; 1996; Urosevic and Evans, 1998; 2000).

Downhole Applications

Downhole applications of the seismic method including cross-hole techniques and Vertical Seismic Profiling (VSP) have been utilised to estimate elastic and mechanical properties of the rocks (Cosma, 1983; Wong et al., 1983; Gustavsson et al., 1984; Wong et al., 1984; Peterson et al., 1985; Harman et al., 1987; Duncan et al., 1989;

Sinadinovski et al., 1995; Cao and Greenhalgh, 1997; Bierbaum and Greenhalgh, 1998; Wong, 2000; Cosma et al., 2003; Greenhalgh et al., 2003; Perron et al., 2003; Bellefleur et al., 2004a; 2004b; Xu and Greenhalgh, 2010).

Borehole seismology has been used to image around the borehole. In a hard rock environment this has amounted to imaging steeply dipping sub-vertical structures (Spathis et al., 1985; Juhlin et al., 1991; Frappa and Molinier, 1993; Adam et al., 2000; Greenhalgh et al., 2000; Urosevic and Evans, 2000; Cosma et al., 2005).

Hard Rock Applications

Seismic reflection methods have been tested in the area of proposed nuclear waste repository sites (located in a hard rock environments) to image fracture zones and discontinuities (Noponen et al., 1979; Mair and Green, 1981; Green and Mair, 1983; Juhlin et al., 1991; Juhlin, 1995; Cosma et al., 2001; Juhlin and Stephens, 2006).

Further development of reflection seismic method to image complex and challenging geological structures (particularly for a crystalline environment) was necessary to further advance mineral exploration (Milkereit et al., 1992; Juhlin et al., 1995; Milkereit et al., 1996; Milkereit and Eaton, 1998; Eaton et al., 2010).

Surface Seismic Methods for Mineral Exploration

The use of seismic reflection methods for mineral exploration, can be traced to the 1980s when extensive 2D seismic surveys were carried out with the aim to map structures for gold exploration in South Africa (Campbell and Peace, 1984; Durrheim, 1986; Pretorius et al., 1989). It was soon recognised that the 2D seismics couldn't properly image the complex hard rock environments and that 3D imaging was required (Urosevic, 2013). The first 3D seismic survey for mineral exploration was conducted in South Africa in 1987 (Campbell et al., 1990; Campbell, 1994). A further survey was carried out by Hall and deWet in 1994 (Urosevic, 2013). In 1995, 3D seismics were used for mineral (Ni-Cu) exploration in the Sundbury complex, Canada (Milkereit et al., (1996); Milkereit et al., (2000). The first succesful use of 3D seismics for mine planning and development was conducted and reported by Pretorius (1997). The first report of success in the delineation of deeply seated (1.2km) massive sulphide deposits

came from the Bathurst Mining Camp in the Halfmile Lake area, Canada (Matthews, 2002; Bellefleur et al., 2004b; Malehmir and Bellefleur, 2009).

In Australia, after a number of trials in the 1970s, Geoscience Australia (GA) acquired several large scale seisimic surveys in the 1990s over the Eastern Goldfeilds area of Western Australia to image crystalline rocks down to Moho (Drummond et al., 2000). Geoscience Australia also conducted deep crustal investigations in 1999 as reported by Goleby et al., (2002) and Evans et al., (2003). Encouraging results using high-resolution reflection seismic methods for kimberlite exploration were reported by Urosevic and Evans (2000). High-resolution studies on a mine scale were also conducted in 2002 (Stolz et al., 2004; Williams et al., 2004). A comprehensive 2D experimental seismic survey was conducted over gold mine sites in Western Australia with very encouraging results reported by Urosevic et al., (2005); Urosevic et al., (2007). The aim of these early studies was to investigate the applicability of the high-resolution seismic reflection method for mapping complex structures in hard rocks as well as stratigraphic units.

The use of 3D seismic methods for exploration started in Kambalda, Western Australia (WA) in 2006, over massive ore (Volcanogenic Massive Sulphide) deposits (Urosevic et al., 2009). They have since become more popular than the 2D approach. Application of the 3D seismic method in Australia started with several small surveys acquired by Department of Exploration Geophysics (DEG), Curtin University (Urosevic et al., 2017).One of the most successful of these surveys, which led to significant mineral discoveries, was conducted and acquired over the Beta Hunt deposits in 2007 (Urosevic et al., 2012). In 2009 HiSeis P/L was formd by DEG to meet the need of the industry for hard rock sesmic exploration. HiSeis have since acquired processed and interpreted numerous 3D surveys (Urosevic et al., 2017). The use of 3D seismic methods for gold exploration was limited in the early 2010s. However, by 2018 over 16 high-resolution 3D surveys have been conducted by HiSeis P/L all over the world mostly over gold deposits (Urosevic et al., 2017).

Multi-Component Methods

Historically seismic reflection surveys for mineral exploration in hard rock environments have been confined to the conventional single component (P-mode) method utilising only one (scalar) component of the wave field. Multi-component methods (usually 3 component (3C)) utilise the full vector field and will provide additional information relating to better definition of subtle structures, rock alteration and lithological boundaries that will be of crucial importance for mineral exploration for deeper targets. There have been a limited number of studies carried out using multi-component seismics for this purpose (Urosevic and Evans, 2000; Bohlen et al., 2003; Bellefleur et al., 2004a; Snyder et al., 2009; Malinowski and White, 2011; Bellefleur et al., 2012; White et al., 2012).

Conventional vertical P-wave imaging will be required, but it will be complemented by the horizontal shear wave (S-wave) images. Specific phenomena related to the propagation of shear waves, such as variation of Poisson's ratio, shear wave splitting, polarisation changes and velocity differences between polarised modes, will provide valuable information related to features such as lithological change, shear zone composition, subtle faulting and fractured zones. Such information is very important when exploring for any type of mineral deposits.

3C methods using a vertical force source while recording three mutually orthogonal components produce more parameters than a conventional 1C survey. These additional parameters can be used to provide results with greater confidence when exploring for mineral deposits (Thomsen, 1999; Stewart et al., 2002, 2003).

Some field studies have produced encouraging results (Bohlen et al., 2003; Snyder et al., 2009; Malehmir et al., 2010; Bellefleur et al., 2012; Malehmir et al., 2012a). They have shown that the S-wave velocity contrast of most mineral deposits with their host rocks is higher when compared to the P-wave velocity contrast (Salisbury et al., 2003; Duff et al., 2012; Malehmir et al., 2013; 2015). This is significant as the resultant higher reflection coefficient using S-wave data is likely to provide better imaging capability.

The first multi-component experimental surveys date back to early 1970s when Conoco started to test a horizontal vibrator. However, no significant developments

occurred until the late 1980s when studies were carried out by a number of academic institutions (CREWES Project at the University of Calgary, Canada; RCP Colorado School of Mines, United States; and Delphi at Delft University, Netherlands). These studies were limited to the oil and gas industry and were aimed specifically at sedimentary environments (Farfour and Yoon, 2016).

In Australia, the first experimental 3C seismic reflection survey for coal exploration was conducted in 1994 as a joint venture between BHP Illawarra coal and Curtin University. Some results were reported in Urosevic and Evans (1996). The objective of the BHP colliery teams was to detect intensly fractured zones hazardous to long-wall mining operations. P-wave results were mainly used for coal seam mapping while S-waves were used to characterise the host rock and detect fracture swarms and other dislocations (Urosevic and Evans, 1996; Urosevic, 2000). Over the first decade of 2000, the use of the S-wave profiling for near surface investigations significantly increased as the potential of high-resolution multi-component seismic methods to observe and characterise the physical parameters of the shallow subsurface was better defined (Pugin et al., 2009; 2010).

1.3 Motivations and Challenges

There are four main factors that are contributing to a slow acceptance of multi-component seismic (Chopra and Stewart, 2010):

1. High cost
2. Complexity of processing and analysis of the full wave field
3. Lengthy and involved interpretation requiring high level calibration
4. Uncertain prospect of success

During the last decade significant technological improvements and software developments have made multi-component technology more robust and reliable. It can now be used and tested even in the extreme geological environments that are often found in mineral exploration. S-waves (which travel slower with shorter wavelengths than conventionally used P-waves) can be utilised to address the challenge of hard rock charcterisation (Garotta, 1999; Polom et al., 2010; Pugin et al., 2010; Pretorius et al., 2011; Inazaki, 2012; Krawczyk et al., 2012; Bansal and Gaiser, 2013; Malehmir et al., 2013; Pugin et al., 2013); this was emphasised when Stewart (2009) stated:

"One of the reliable techniques, which provide extensive details on prospect areas, is multi-component seismic. This method uses analysis of one-component P-wave and two-component S-wave data and has lots of benefits such as: better structural picture, further stratigraphic details, indication of rock types, petrophysical properties, a description of faults/fractures/cracks, a notion of the stress regime and estimate of the fluid content, which have become available by the help of the measurements of the shear-wave information.".

Even so, such information is difficult to extract from 3C seismic data. No commercial approach or methodology exists as yet for processing 3C seismic data, particularly in hard rock environments. The purpose of this research is to pave the way for a future where conventional application of multi-component methodologies for exploration of mineral deposits is routine. The key outcome of this feasibility study is to evaluate the true value of multi-component seismic and help further develop its application for exploration of complex mineral systems and deposits.

The enormous technological advances in processing and interpretation of 3C seismic data in the past decade have made it a feasible method. Compared to conventional P-

wave processing, there are still challenges. Most of the published multi-component experiments and studies have been accomplished in sedimentary basins for oil and gas exploration purposes. Such environments constitute “simple systems” as they are characterised by horizontal or sub-horizontal layers, usually with significant continuity, good reflectivity and high signal to noise ratios (SNR). None of these conditions usually occur in a hard rock environment commonly characterised by complex geological structures, abrupt changes, rock alteration in complex ways, intrusion by dykes, differing fault patterns, fractures and shear zones. Most structures are steeply dipping or sub-vertical. Scattering, distortion and absorption of seismic energy is commonplace due to the presence of the regolith. Near surface and complex hard rock environments are typified by data with low SNR and as a consequence low quality imaging.

Processing of converted S-waves is much more involved than processing of P-waves. Extra steps are required to deal with issues such as a polarity changes related to the shear wave geophone directivity, possible splitting and re-conversions to P-mode. Particular difficulties also relate to the derivation of a converted wave (PS) static solution, data rotation, calculation of the depth dependant conversion points and imaging in general. S-wave velocity determination from a PS-wave image is also complicated by a number of factors such as the effects of anisotropy, shear wave splitting and the occurrence of different kinds of surface waves adversely affecting the horizontal components. These challenges will be discussed in detail as part of the next chapter.

From the few hard rock multi-component seismic examples available, it appears that the three components (vertical, inline and crossline) have different characters in terms of frequency, amplitude and apparent seismic events. Figure 1-3 shows a sample 3C test shot acquired in Western Australia. Complex and different wave patterns occur for each component. This information can be used to benefit exploration.

a)

b)

c)

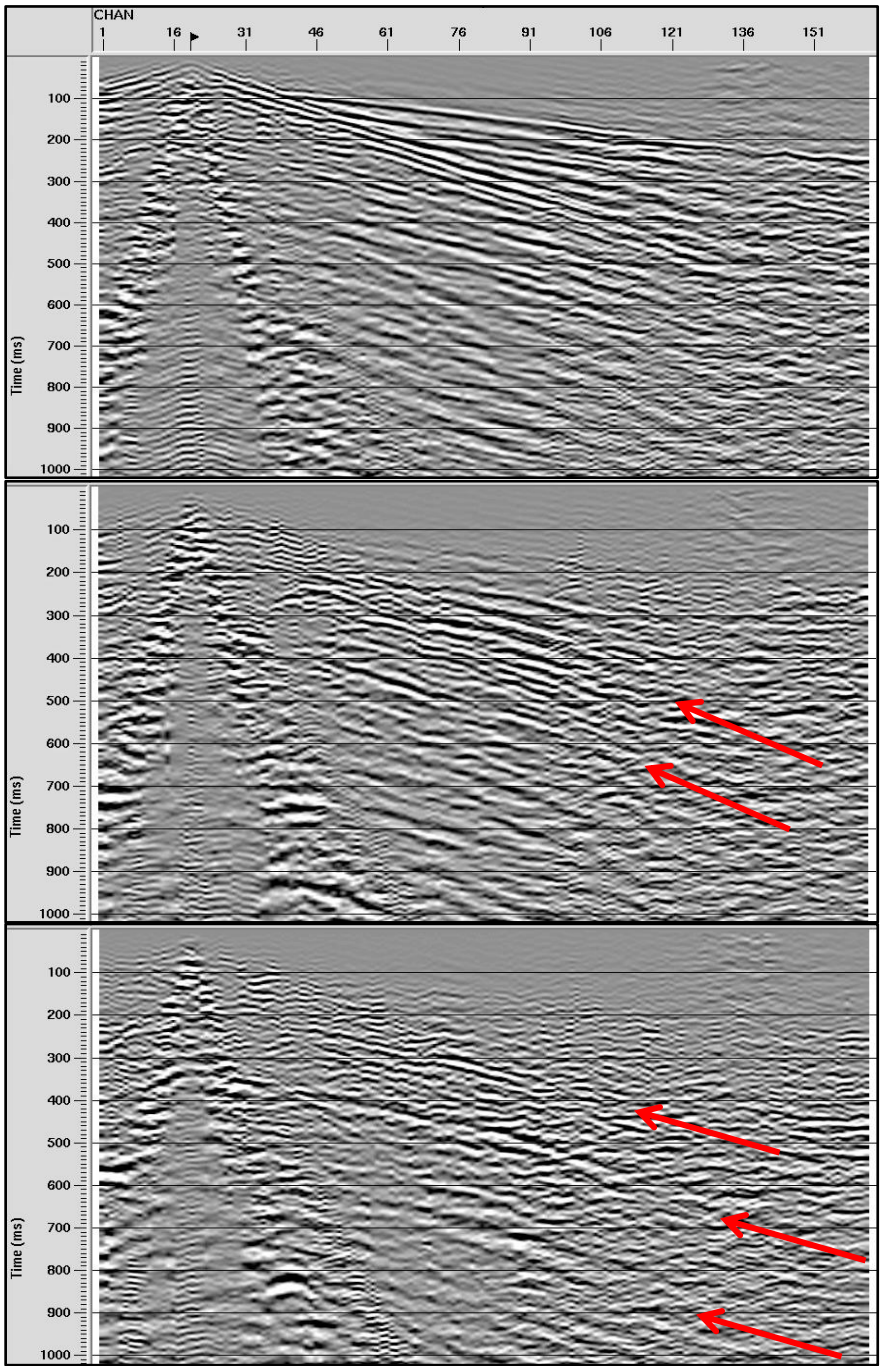

Figure 1-3 A sample 3C test shot acquired in Western Australia to uncover the potential of 3C seismic. a) vertical component, b) inline horizontal component c) crossline horizontal component. Red arrows denote continuous reflected events that are easier to identify on the inline and crossline components than on the vertical component.

1.4 Research Objectives

The applicability of the multi-component seismic method as a viable methodology for the mineral exploration in a hard rock environment is untested. This study aims to address this issue by analysing all stages of a multi-component survey from survey

design and acquisition to data processing analysis and interpretation. The main objective of this research is to understand and evaluate the potential and applicability of multi-component seismic for exploration of mineral resources.

This objective will be achieved by conducting studies using modelled data followed by the analysis of field data. A comprehensive assessment and evaluation of three component (3C) seismology for the purpose improving the mineral exploration will be carried out including:

- Analysis of the raw wavefields recorded by vertical and horizontal geophones
- Optimisation of the processing algortihms and interpretation/analysis of the resultant images

1.5 Methodology

For this study three different multi-component surface seismic data sets have been used:

- Modelled 3D data based on the Kevitsa deposit (Finland)
- 2D Field data (MSDP10 data set)
- 3D Field data (ROYHILL data set)

The field data will have a much lower signal to noise ratio (SNR) than the modelled data. This being so, initial investigations will use the modelled data to develop concepts of processing to analyse complex wavefields and understand how to best analyse them. These concepts will then be tested and refined on the field data.

To efficiently handle shear wave polarisation, it will be necessary to develop new rotation analysis algorithms, or improve existing ones, for 3C data processing in the low SNR environments typically encountered in hard rock settings.

Polarisation Panel Analysis proposed by Urosevic (2000) will be utilised to determine the most likely symmetry for the area (assuming simple anisotropic models) resulting from in situ asymmetric stress.

Travel time delay (statics) estimate in the near surface (regolith) represent a significant challenge for P-wave surveys. Determining a statics solution for S-wave data is far

more difficult mainly as the relevant arrivals are not first breaks and not easily identified. Special attention will be devoted to testing different static correction models and methods. One of the approaches to be evaluated on the ROYHILL dataset combines Multichannel Analysis of Surface Waves (MASW) with a reference picked horizon to compute static corrections.

1.6 Thesis Outline

This thesis is organised into five chapters: *Introduction*, *Multi-component Methodology*, *2D/3C MSDP10 case study*, *3D/3C ROYHILL case study* and *Conclusions and Recommendations.*

Introduction: lists the objectives of this project and the methodology. It provides the significance of the multi-component methodology and a brief review of background research of seismic methods for exploration purposes.

Multi-component Methodology: fundamentals of the methodology are discussed in detail. Special attention is devoted to the challenges that were encountered during testing and parametrisation of the flows for the 3C data processing.

2D/3C MSDP10 case study: the applicability of the method using a 2D/3C data set is shown. A new rotation analysis algorithm to utilise the additional information contained in multi-component data is discussed.

3D/3C ROYHILL case study: the applicability of the full range of processing steps tested using the modelled data is shown. The use of Polarisation Panel Analysis to find the optimal angle of rotation for the data set and confirm anisotropy is demonstrated. Different converted wave statics solutions are tested, and the results presented.

Conclusions and Recommendations: conclusions and recommendations are provided.

Chapter 2 Multi-component Methodology

2.1 Introduction

In the following chapter the fundamentals and principles of the multi-component technology will be discussed. The physics of the technology will be analysed in terms of the particle displacement vectors of different modes of the seismic wavefield. Basic concepts covering wave propagation in hard rocks will be used within the text and are introduced and defined.

2.1.1 Definition and Background

Multi-component seismic data have the potential for application in exploration for mineral resources as the different wave modes will provide additional information about the subsurface.

Multi-component seismic is not routinely utilised in exploration programs due to the complexity and difficulty in extracting information provided by more than one component. Its potential has been tested on soft (sedimentary) rocks in the oil industry, and there is the potential to transfer the technology to other sectors such as mineral exploration. The use of multi-component seismic is simply untested in the mineral sector. Interpretation of even single component (P-wave) seismic data is challenging in overly complex hard rock environments. Hence it is not surprising that interpretation of three or multi-component data is not favoured by the industry at present. In future this could change by transferring some of the technologies developed for soft rock exploration such as elastic wavefield seismic stratigraphy, three component attribute analysis and similar.

2.1.2 Wave Propagation

Seismic waves are generated by some kind of impulsive source such as an explosion or an earthquake and travel through the Earth's interior (body waves) or along the surface (surface waves). The spreading of the wavefield generated by a source can at any one time be described by the shape of the wavefront. The wavefront is the surface over which the phase value remains the same, while the propagation direction is perpendicular to the wavefront (Yilmaz, 2001). If the disturbance remains the same everywhere on a plane normal to the propagation direction, the wave is assumed to be a plane wave. A plane wave assumption is made if the receiver is far enough away

from the initial disturbance (far field). This assumption is often used to solve wave equations exactly. Moreover, superposition of the plane waves can also approximate a curved wavefront. A line representing the propagation direction is called the raypath.

There are two types of body waves, P-wave (pressure or primary wave) and S-wave (shear or secondary wave). They are nondispersive, meaning that they travel with the same velocity at all frequencies. The P-wave (also known as the dilatational, longitudinal, irrotational, compressional wave) is faster than the S-wave (also known as the transverse, rotational wave (Sheriff, 2002)) as it occurs first on a seismogram with the S-wave occurring second.

Surface waves are confined to the ground surface and lose their energy rapidly with depth. Rayleigh waves are the most important surface waves in exploration seismology because they propagate between a boundary and a free surface and retain their energy over large distances. They have much higher amplitude than body waves and mask the body wave energy where they occur. Love waves are a second type of surface wave. They are generated when the shear wave velocity of the surface layer is lower than that of underlying layer (Kearey et al., 2013). They occur where the upper finite layer (with low horizontal velocity) terminates at a free surface and the underlying layer is an elastic semi-infinite solid medium. The propagation velocity of the Love waves approaches that of S-waves in the surface for very high frequencies or short wavelengths and is similar or the same as S-waves for low frequencies or very long wavelengths (Dobrin, 1951).

All the above waves have different particle motion along their propagation path (Figure 2-1). P-wave particle motion is parallel to the direction of propagation. S-waves travel with particle motion perpendicular to the propagation direction (Pujol, 2003). S-waves have two degrees of freedom and as a consequence polarise in two orthogonal planes - horizontal (SH) and vertical (SV). SH and SV waves have the same velocity of propagation in isotropic media. However, in reality where anisotropy occurs, they may have different velocities and polarisation vectors that are not orthogonal to the direction of propagation. SH and SV waves may make the wave picture more complex, however, the potential benefit of analysing their propagation is likely to be significant for exploration. Each body wave mode provides different information (contained in the reflected wavefield) about the subsurface geology.

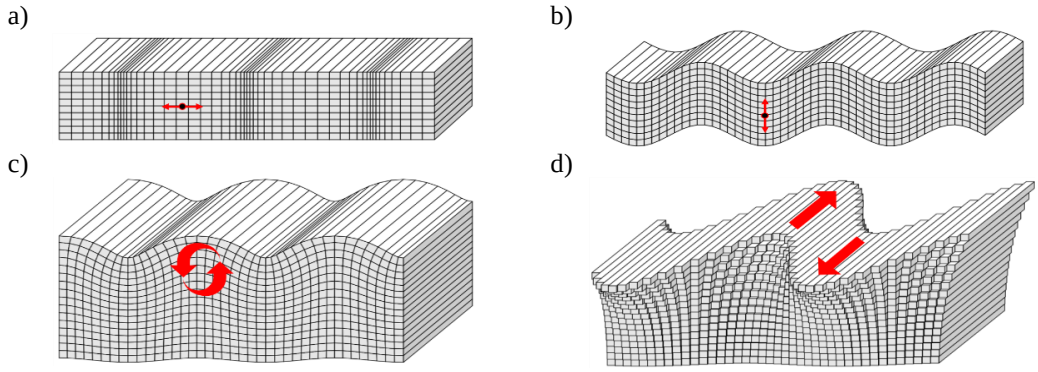

Figure 2-1 Seismic waves cause disturbance of the ground particles as they travel through the elastic earth materials. a) P-wave propagation will result in volume change in the material while b) pure S-waves cause shape change with no change in volume. c) Rayleigh wave propagation causes vertical and radial motion (elliptical, retrograde) d) Love waves are characterised by purely transverse motion. For the examples above, the propagation direction is to the right and the red arrows are the particle motion associated with each wave type (after (Shearer, 2009)).

2.1.3 Seismic Reflectivity

In reality, at a boundary, a portion of an incident P-wave will be converted to shear waves with both waves partly transmitted and reflected from the boundary (Yilmaz, 2001). A geometrical relationship between the various modes is illustrated in Figure 2-2.

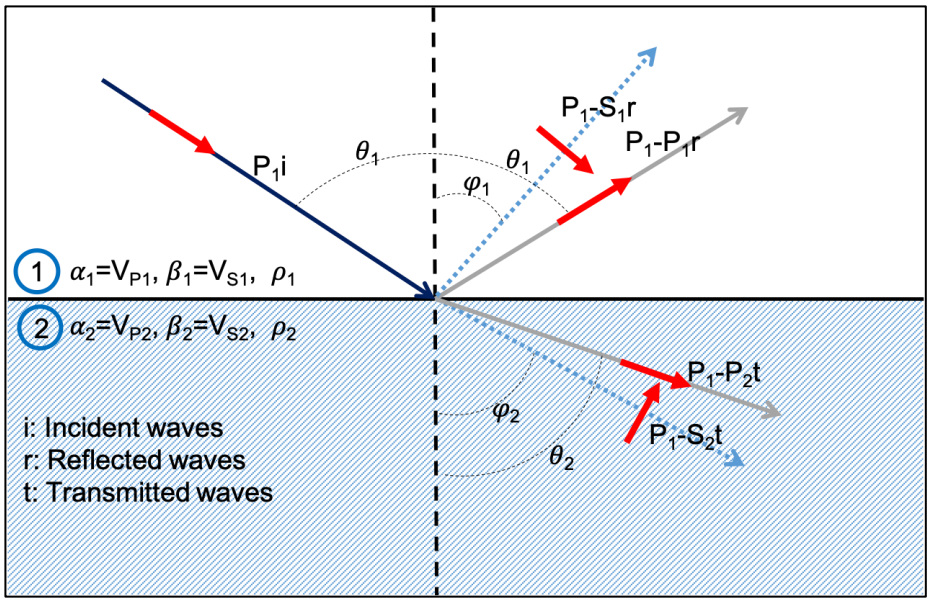

Figure 2-2 A simple two-layer model showing the incident P-wave and the transmitted and reflected P and S-waves (after (Yilmaz, 2001)). Red arrows depict the polarity that should be assumed for the converted S-wave (SV) reflected and transmitted waves (assuming the acoustic impedance of the lower layer is greater than that of the upper one).

According to Snell's law the relationship between these modes is:

$$p = \frac{\sin\theta_1}{\alpha_1} = \frac{\sin\theta_2}{\alpha_2} = \frac{\sin\varphi_1}{\beta_1} = \frac{\sin\varphi_2}{\beta_2}, \tag{2-1}$$

where p is the ray parameter, $\theta_1$is the angle of incidence and reflection and θ_2 is the angle of the transmitted P-wave, $\varphi_1$is the angle of reflected S-wave and φ_2 is the angle of transmitted S-wave, α is V_P and β is V_S of each layer.

Each mode will have a proportion of the initial wave energy. Karl Bernhard Zoeppritz (Zoeppritz, 1919) studied this partitioning of the energy for isotropic media and showed that the dependence of the reflection coefficient to the incident angle is non-linear. This is described by a set of linear equations that can be written in a form:

$$\begin{pmatrix} \cos\theta_1 & \frac{\alpha_1}{\beta_1}\sin\varphi_1 & \frac{\alpha_1}{\alpha_2}\cos\theta_2 & -\frac{\alpha_1}{\beta_2}\sin\varphi_2 \\ -\sin\theta_1 & \frac{\alpha_1}{\beta_1}\cos\varphi_1 & \frac{\alpha_1}{\alpha_2}\sin\theta_2 & \frac{\alpha_1}{\beta_2}\cos\varphi_2 \\ -\cos 2\varphi_1 & -\sin 2\varphi_1 & \frac{\rho_2}{\rho_1}\cos 2\varphi_2 & -\frac{\rho_2}{\rho_1}\sin 2\varphi_2 \\ \sin 2\theta_1 & -\frac{\alpha_1^2}{\beta_1^2}\cos 2\varphi_1 & \frac{\rho_2\beta_2^2\alpha_1^2}{\rho_1\beta_1^2\alpha_2^2}\sin 2\theta_2 & \frac{\rho_2\alpha_1^2}{\rho_1\beta_1^2}\cos 2\varphi_2 \end{pmatrix} \begin{pmatrix} A_1 \\ B_1 \\ A_2 \\ B_2 \end{pmatrix} = \begin{pmatrix} \cos\theta_1 \\ \sin\theta_1 \\ \cos 2\varphi_1 \\ \sin 2\varphi_1 \end{pmatrix}, \tag{2-2}$$

where A_1 is the reflected and A_2 is the transmitted P-wave amplitude, B_1 is the reflected and B_2 is the transmitted S-wave amplitude. These sets of equations are normalised by the incident wave amplitude of $A_0 = 1$ and can be solved for four unknowns. However, this formulation is non-intuitive and further simplifications are required for its application in exploration with some of most useful linearization and approximation of the Zoeppritz equation provided by Aki and Richards (1980), Shuey (1985) and Thomsen (1990). Note that this scalar formulation governing two wave modes needs to be expanded to vector wave analysis for the application of multi-component seismic.

Changes in acoustic impedance (Z), which is the product of the seismic velocity and the density of the rock units, result in seismic reflectivity. A seismic wave propagating within a medium experience these changes when crossing different rock formations. The ratio of the differences of the amplitudes of the reflected wave to the incident wave will govern the amount of energy to be reflected or transmitted at the contact of two rocks (layer boundary in soft rock terminology). This ratio is called the reflection coefficient (R) and for a normal incidence wave it is defined as:

$$R = \frac{\rho_2 V_2 - \rho_1 V_1}{\rho_2 V_2 + \rho_1 V_1} = \frac{Z_2 - Z_1}{Z_2 + Z_1}, \tag{2-3}$$

where Z_i is the acoustic impedance, ρ_i is the density and V_i is the velocity of the individual layer *i*. It should be noted that based on this equation, the reflection coefficients are calculated separately for P and S-waves.

2.1.4 Vector Sources

For a vector source in a half space, a full wavefield will be generated comprising three orthogonally polarised displacement vectors within the medium. The three modes created by the source are captured by vector sensors with the same alignment as each mode. Different modes travel through the medium at different velocities, distorting the medium in their own respective direction. For a scalar source, the full displacement vector is generated but only the time-dependent function of the particle displacement is captured at the sensor. For a full-vector source, two seismic properties are measured: the time-dependent function of the particle displacement and the direction of motion. Thus, the difference between a scalar and a vector source is their usage and not their functionality. Figure 2-3 illustrates the relation between the propagation direction and the orientation directions of the three modes' displacement vectors in an isotropic medium.

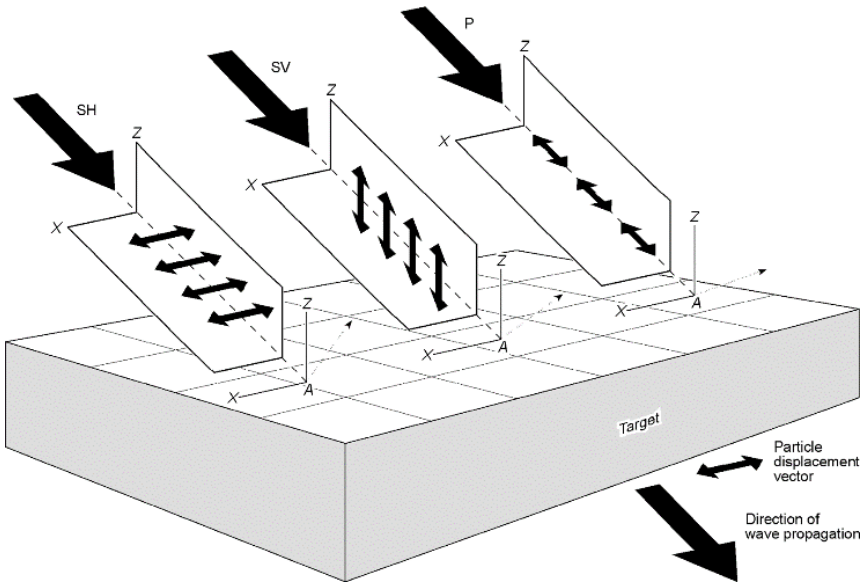

Figure 2-3 A schematic view of a full-elastic seismic wavefield propagating in an isotropic medium and all the related modes (P, SV and SH). The difference between each mode is its particle displacement vector along the propagation path. (after (Hardage et al., 2011)).

Figure 2-4 depicts the SV and SH relative positions in an imaginary plane containing both source and observation points (sagittal plane).

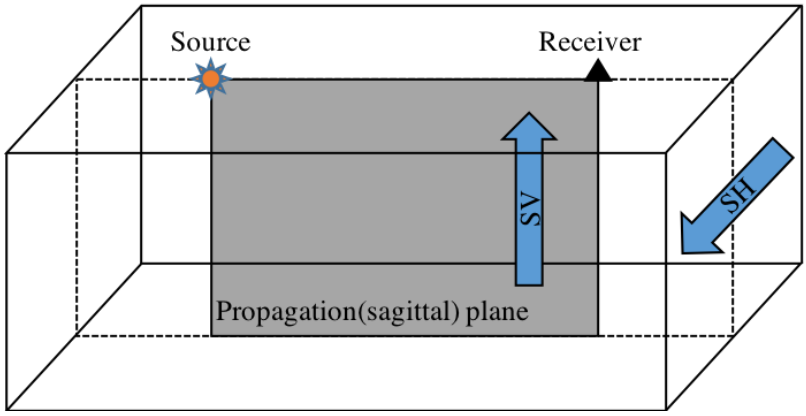

Figure 2-4 SV wave propagation versus SH propagation in an isotropic medium. SV displacement occurs in the vertical plane that passes through the source station and the observation point. SH displacement is normal to this plane.

2.1.5 Elastic Waves for Rock Characterisation

Conventional seismic surveys utilise the vertical component only. All other modes are suppressed during processing. The information obtained is the time-dependent function of the particle displacement (wave amplitude). The speed or velocity of the propagating wave is given by:

$$V_P = \alpha = \sqrt{\frac{\lambda + 2\mu}{\rho}}, \tag{2-4}$$

where μ is the modulus of rigidity or shear modulus, λ is the Lamé's constant and ρ is the density. From the definition of the bulk modulus (κ) (the ratio of the hydrostatic stress to the volumetric strain) we have:

$$\kappa = \lambda + \frac{2}{3}\mu. \tag{2-5}$$

Solving equation 2-5 for λ and substituting into equation 2-4, the expression for the compressional-wave velocity in terms of bulk modulus (κ) and shear modulus (μ) is:

$$V_P = \alpha = \sqrt{\frac{\kappa + \frac{4}{3}\mu}{\rho}}. \tag{2-6}$$

Even if the amplitude and velocity of a compressional wave is precisely measured it

cannot uniquely characterise the medium through which it was measured. The three elastic constants contained within V_P would assist greatly in the analysis. However, to obtain these constants more measurements are required.

Shear wave velocity is defined by the simple equation:

$$V_S = \beta = \sqrt{\frac{\mu}{\rho}}. \tag{2-7}$$

By measuring shear wave velocity and combining it with the P-wave velocity and acquiring density information from other sources, all elastic constants for an anisotropic medium can be defined. Based on the generalised Hook's law which is valid for anisotropic, linear and elastic media, and using Voigt notation, C_{IJ} (stiffness) matrix can be written (Mavko et al., 2009). Stiffness matrix and its components (referred as elastic constants here) is widely adopted when discussing elastic anisotropy. Elastic constants for an isotropic medium using two indices notation can be expressed as:

$$C_{IJ} = \begin{bmatrix} C_{11} & C_{12} & C_{12} & 0 & 0 & 0 \\ C_{12} & C_{11} & C_{12} & 0 & 0 & 0 \\ C_{12} & C_{12} & C_{11} & 0 & 0 & 0 \\ 0 & 0 & 0 & C_{44} & 0 & 0 \\ 0 & 0 & 0 & 0 & C_{44} & 0 \\ 0 & 0 & 0 & 0 & 0 & C_{44} \end{bmatrix}, C_{12} = C_{11} - 2C_{44}\,. \tag{2-8}$$

For the case of isotropic linear elasticity, C_{IJ} can be written based on elastic Lamé coefficients (λ and μ). These are related to the isotropic elastic coefficients ($C_{11} = 2\mu + \lambda$, $C_{12} = \lambda$ and $C_{44} = \mu$):

$$C_{IJ} = \begin{bmatrix} (2\mu+\lambda) & \lambda & \lambda & 0 & 0 & 0 \\ \lambda & (2\mu+\lambda) & \lambda & 0 & 0 & 0 \\ \lambda & \lambda & (2\mu+\lambda) & 0 & 0 & 0 \\ 0 & 0 & 0 & \mu & 0 & 0 \\ 0 & 0 & 0 & 0 & \mu & 0 \\ 0 & 0 & 0 & 0 & 0 & \mu \end{bmatrix}. \tag{2-9}$$

Hence, there are only two independent elastic constants that can be estimated by measuring P and S (either SV or SH) wave modes.

In an anisotropic medium the propagation of the waves is more complex predominantly as wave velocities (and amplitudes) are directionally dependent. Even

for the highest common symmetry (hexagonal) 5 independent elastic constants are required:

$$C_{IJ} = \begin{bmatrix} C_{11} & C_{12} & C_{13} & 0 & 0 & 0 \\ C_{12} & C_{11} & C_{13} & 0 & 0 & 0 \\ C_{13} & C_{13} & C_{33} & 0 & 0 & 0 \\ 0 & 0 & 0 & C_{44} & 0 & 0 \\ 0 & 0 & 0 & 0 & C_{44} & 0 \\ 0 & 0 & 0 & 0 & 0 & C_{66} \end{bmatrix}, C_{12} = C_{11} - 2C_{66}\,. \tag{2-10}$$

In anisotropic media, three modes of propagation are defined: quasi-longitudinal (V_P), quasi-shear (V_{SV}) and pure shear (V_{SH}). For the highest common symmetry (hexagonal), in any plane containing the symmetry axis (Mavko et al., 2009), these modes are defined as:

Quasi-longitudinal

$$V_P = \left(C_{11}\sin^2\theta + C_{33}\cos^2\theta + C_{44} + \sqrt{M}\right)^{1/2}(2\rho)^{-1/2}, \tag{2-11}$$

Quasi-shear

$$V_{SV} = \left(C_{11}\sin^2\theta + C_{33}\cos^2\theta + C_{44} - \sqrt{M}\right)^{1/2}(2\rho)^{-1/2}, \tag{2-12}$$

Pure shear

$$V_{SH} = \left(\frac{C_{66}\sin^2\theta + C_{44}\cos^2\theta}{\rho}\right)^{1/2}, \tag{2-13}$$

where $M = [(C_{11} - C_{44})\sin^2\theta - (C_{33} - C_{44})\cos^2\theta]^2 + (C_{13} + C_{44})^2\sin^2 2\theta$, and θ is the angle between the wave vector and vertical axis ($\theta = 0^\circ$ for propagation in vertical direction).

All three wave modes should be measured to describe wave propagation in an anisotropic medium to come close to characterising the medium. Apart from C_{13} each elastic constant is related to a particular wave mode. Hence, as Tsvankin (2012) described, for the vertical direction:

$$V_P(\theta = 0^\circ) = \sqrt{\frac{C_{33}}{\rho}}, \tag{2-14}$$

$$V_{SV}(\theta = 0^\circ) = \sqrt{\frac{C_{55}}{\rho}}, \tag{2-15}$$

and for the horizontal direction:

$$V_P(\theta = 90^{\circ}) = \sqrt{\frac{C_{11}}{\rho}}, \tag{2-16}$$

$$V_{SV}(\theta = 90^{\circ}) = V_{SV}(\theta = 0^{\circ}) = \sqrt{\frac{C_{55}}{\rho}}. \tag{2-17}$$

For V_{SH}:

$$V_{SH}(\theta) = \sqrt{\frac{C_{66}\sin^2\theta + C_{55}\cos^2\theta}{\rho}}. \tag{2-18}$$

From equation 2-18, V_{SH} for propagation in a vertical direction ($\theta = 0^{\circ}$) will be $\sqrt{\frac{C_{55}}{\rho}}$ and in a horizontal direction ($\theta = 90^{\circ}$) will be $\sqrt{\frac{C_{66}}{\rho}}$. Therefore, the difference between C_{55} and C_{66} will directly affect the strength of velocity anisotropy of the SH-waves. From the above equations all the "wave" constants have physical bounds with the exception of C_{13} which is not related directly to any wave mode.

Since the real-earth is anisotropic, different results can be obtained depending on the direction of wave propagation. Weak anisotropy is often measured in sedimentary rock formations (Thomsen, 1986). In hard rocks the degree of anisotropy is generally unknown. Very rare measurements indicate that anisotropy is non-negligible (Ahmadi and Malehmir, 2013) and should be considered for upcoming analysis. Possible causes of anisotropy in hard rocks include the orientation of the minerals, alignment of the fabric, structural factors (shear zones). The degree of seismic anisotropy may be different between different wave modes. In soft rocks, P-wave propagation depends on rock matrix properties such as grain cementation, porosity and pore fluid. S-wave propagation is dependent on the rock frame and grain cement only. In hard rocks, porosity is usually close to zero. This being so, the propagation of both wave modes is governed by the rock frame and/or crystal properties. As a result, it should be expected that there will be no significant difference in the degree of anisotropy between various wave modes. However, this has not been established well particularly for hard rocks.

To understand seismic anisotropy, consider a simple thin layered system (often found

in soft rock environments) with the dominant seismic wavelength much larger than the thickness of each layer. When the wavelength becomes 8 or more times longer than the layer thickness the whole system becomes effectively anisotropic. The symmetry of such a system is referred to as having transverse isotropy with a vertical axis of symmetry (VTI or sometimes TIV). A model to illustrate this is shown in Figure 2-5.

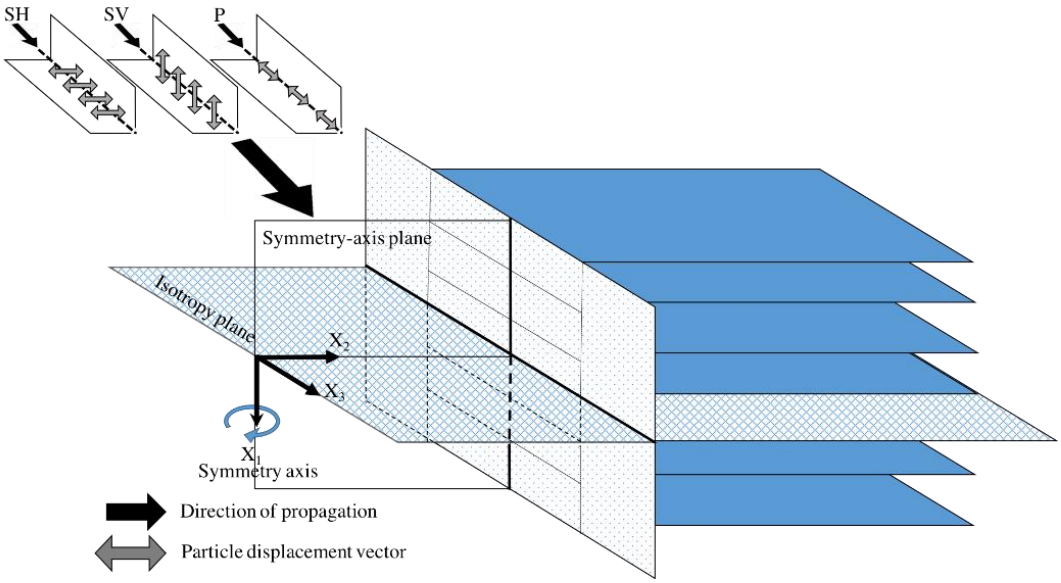

Figure 2-5 Schematic view of a VTI model (isotropic model with horizontal layering).

P- and SV-waves remain coupled but their velocities exhibit different behaviour in different directions. For example, in the horizontal direction the P-waves will propagate with a faster velocity than in the vertical direction as they utilise more consolidated constituents of the model. In the vertical direction P-waves will propagate through the layers with an "average" velocity of the system (since they probe all constituents equally). SV waves have a particle oscillation that is polarised in a vertical plane and will propagate through the system in both horizontal and vertical directions in the same way with the same velocity. SH wave propagation is decoupled from both the P- and SV-waves in all cases. SH waves (with particle displacements parallel to the layers), will be similar to the P-waves in that velocities in the horizontal direction will be faster than those in the vertical direction. The wave surface for SH-waves will have a simple elliptical shape. However, propagation paths for P- and SV-waves may result in complex wave surfaces including wavefront cusping (Postma, 1955; Urosevic and McDonald, 1985). Wave propagation in a VTI medium is governed by five elastic constants rather than two in an isotropic medium. To determine the three extra constants, even for this simple geological model, a three-component recording system

is required.

Three-component data are recorded using an arrangement of three orthogonally aligned recording sensors. An impact (P-wave) source (used to generate the down-going wavefield) will generate both P and SV waves. Further complication occurs when SV-waves split on entering an anisotropic medium. Even pure P-waves generated using a vibroseis source will result in mode conversion (to SV) at an interface when propagating in any direction away from vertical. Mode conversion becomes more pronounced as the velocity contrast across an interface becomes larger. When recording, only the vertical and in-line oriented sensors will record energy with the assumption that what is captured are separated pure modes. In reality, further complications are expected, but to keep it simple it is assumed that P and SV wave propagation will produce various mode conversions such as P to SV and SV to P. This being so, processing of 3C data is much more involved in comparison to conventional P-wave (single vertical component) data processing as it is necessary to analyse the two pure modes as well as all converted modes.

P- and S-waves have different velocities and propagate in different ways. P-wave propagation depends on the framework of the rock and the fluid in the pore spaces. S-wave propagation is largely unaffected by the fluid in pore space. However, the fluid type can change the bulk density and as a result make a marginal change in the velocity. As a consequence, P- and S-waves provide different information about the rock. Their reflectivity functions may be different depending on the P- and S-wave impedance contrasts across interfaces. Some interfaces can produce measurable S-wave reflectivity and no P-wave reflectivity at normal incidence and vice versa. To add complication, this may change as the angle of incidence changes.

As S-waves have two degrees of freedom (horizontal (SH) and vertical (SV)), in an anisotropic medium they can exhibit complex propagation patterns. For example, when an S-wave enters an anisotropic medium, it can split into two modes (a fast-S mode and slow-S mode) that propagate with different velocities (Crampin, 1981). The fast-S mode displacement vector (S1 (or qS1; as quasi shear-wave)), is approximately parallel with the plane of isotropy, which in turn is parallel to the maximum horizontal stress or the vertical discontinuity. The slow-S mode displacement vector (S2 (or qS2; as quasi shear-wave)) is perpendicular to the plane of isotropy (Crampin, 1981;

Hardage et al., 2011). Whilst each mode provides additional information, their relationship is also of interest for exploration. Possible mode conversions are shown in Table 2-1.

Table 2-1 Example of acquisition options for multi-component seismic data and the generated seismic modes for an isotropic and anisotropic medium in which there is S-wave splitting. Subscript 1 and 2 are fast-S and slow-S mode respectively. X = radial, Y=transverse, Z=vertical and H=hydrophone components; A is an airgun.

	Source	Receiver	Captured modes (Isotropy)	Captured modes (Anisotropy)
1C	Z	Z	P-P	P-P
3C	Z	X, Y & Z	P-P, P-SV	P-P, P-SV_1, P-SV_2
4C	Z/A	X, Y, Z & H	P-P, P-SV	P-P, P-SV_1, P-SV_2
6C	Y and Z	X, Y & Z	P-P, P-SV, SH-SH	P-P, P-SV_1, P-SV_2, SH_1-SH_1, SH_2-SH_2
9C	X, Y and Z	X, Y & Z	P-P, P-SV, SV-SV, SV-P, SH-SH	P-P, P-SV_1, P-SV_2, SV_1-SV_1, SV_2-SV_2, SV_1-P, SV_2-P, SH_1-SH_1, SH_2-SH_2

Based on the Zoeppritz equations a unique reflectivity equation is available for each wave mode listed in Table 2-1. These equations define the relationship between the elastic impedance of the medium and its reflection amplitude and the phase of each mode. The same equations can be expanded for anisotropic media (Schoenberg and Protazio, 1990; Rüger, 1997; Vavryčuk and Pšenčik, 1998).

The terminology of Aki and Richards (1980) shown in Table 2-2 will be used to denote various wave mode conversions. Every wave mode in Table 2-1, has a distinct equation for reflectivity. The P-wave velocity represented by V_P (α), and the S-wave velocity by V_S (β).

Table 2-2 Mathematical terms used by Aki and Richards (1980).

Variables	Cosine-dependent terms
$a = \rho_2(1 - 2\beta_2^2 p^2) - \rho_1(1 - 2\beta_1^2 p^2)$	$E = b\frac{\cos\theta_1}{\alpha_1} + c\frac{\cos\theta_2}{\alpha_2}$
$b = \rho_2(1 - 2\beta_2^2 p^2) + 2\rho_1\beta_1^2 p^2$	$F = b\frac{\cos\varphi_1}{\beta_1} + c\frac{\cos\varphi_1}{\beta_1}$
$c = \rho_1(1 - 2\beta_1^2 p^2) + 2\rho_2\beta_2^2 p^2$	$G = a - d\frac{\cos\theta_1}{\alpha_1}\frac{\cos\varphi_2}{\beta_2}$
$d = 2(\rho_2\beta_2^2 - \rho_1\beta_1^2)$	$H = a - d\frac{\cos\theta_2}{\alpha_2}\frac{\cos\varphi_1}{\beta_1}$
	$D = EF + GHp^2$

The equations shown in Table 2-2 include a number of parameters such as density(ρ), horizontal slowness or ray parameter (p), V_P (α) and V_S (β). Other parameters are defined as part of Figure 2-2.

Three-component (3C) seismic can be acquired using any kind of downgoing wave. However, in conventional applications a P-wave source is used with the PS-waves generated by mode conversion. When a P-wave source is used, there are two constitutive equations for the reflectivity of P and the converted PS modes. Using the terminology defined in in Table 2-2, these are:

$$P_1\text{-}P_1r = \left[\left(b\frac{\cos\theta_1}{\alpha_1} - c\frac{\cos\theta_2}{\alpha_2}\right)F - \left(a + d\frac{\cos\theta_1}{\alpha_1}\frac{\cos\varphi_2}{\beta_2}\right)Hp^2\right]/D \quad (2\text{-}19)$$

$$P_1\text{-}S_1r = -2\frac{\cos\theta_1}{\alpha_1}\left(ab + cd\frac{\cos\theta_2}{\alpha_2}\frac{\cos\varphi_2}{\beta_2}\right)p\alpha_1/(\beta_1 D) \quad (2\text{-}20)$$

Based on Snell's law, horizontal slowness remains unchanged regardless of the medium symmetry and for every reflected (r)/transmitted mode (t) (Sheriff, 2002). Subscript 1 refers to the layer over the interface and subscript 2 refers to the layer below the interface.

The solution for reflectivity equations associated with seismic modes (other than the SH-SH mode as it is assumed SH is not generated) requires that the particle-displacement vector polarities of the incident and transmitted P and SV waves are known at an interface. In Figure 2-2, where impedance has a downward increase, the assumed polarities by Aki and Richards (1980) are illustrated. For this study, a positive sign will be assigned to any particle-displacement vector if the direction conforms with that depicted in Figure 2-2. Conversely, opposite directions will be assigned a negative sign.

Some of the principles of multi-component data in isotropic media are:

- 3C data are a subcategory of 9C data.
- For 3C data there is one S-wave mode (P-SV), whereas in 9C data there are three S-wave modes (P-SV, SH-SH, and SV-SV).
- The reflectivity equations and solutions for the three S-wave modes (P-SV, SH-SH, and SV-SV) are different, resulting in different subsurface images.
- Only P and SV modes are coupled (exchanging energy throughout reflection). The SH mode is independent exchanging no energy with either the P or SV

mode. Hence to generate SH mode, an SH source is required. This type of source is not available for 3C or 4C data.

- The reflectivity of SH-SH data is usually easier to interpret as it is mathematically less complicated than the reflectivity of P-SV and SV-SV.
- For 3C data, the only available P-wave mode is P-P. For 9C data there are two (P-P and SV-P).

The mathematical derivation for each modes' reflectivity equation is different. Consequently, the response of each mode to the elastic properties of the subsurface is different. This being so, the resulting seismic images are different for each allowing better characterisation of the subsurface.

2.1.6 P-wave Source and P-SV Mode Conversion

Mode conversion of P to SV creates different S-wave radiation patterns than those from an SV-wave source. Using a P-source, P-waves propagate from the surface source station and it is possible at every point along the propagation path for conversion to SV.

For 3C with a P-wave source, the orientation direction of the particle-displacement vector (assuming an isotropic medium), changes according to azimuth. However, in an isotropic medium, the orientation of the SV particle-displacement vector (indicative of the S-wave propagation) is in the radial direction of the P-wave propagation path. In an anisotropic medium two shear waves will be present. These are quasi shear-waves as particle oscillation is not orthogonal to the energy propagation (Crampin, 1985).

The following conclusions can be made:

- The only products of a P-wave source in an isotropic medium are P-waves and mode converted SV-waves.
- For 3C illumination, where there is a 180-degree difference between two propagation azimuths, the SV-wave has an opposite polarity in its particle displacement vector.
- The converted SV-wave illumination intensity in 3C acquisition, is independent of azimuth direction.

Figure 2-6 illustrate the polarisation of SV vectors in each acquisition quadrant for a P-wave source and 3C receivers. Polarisation of the SV mode is depicted as two vector components (inline/crossline and radial/transverse) used in each of the quadrants for Figure 2-6a and Figure 2-6b respectively.

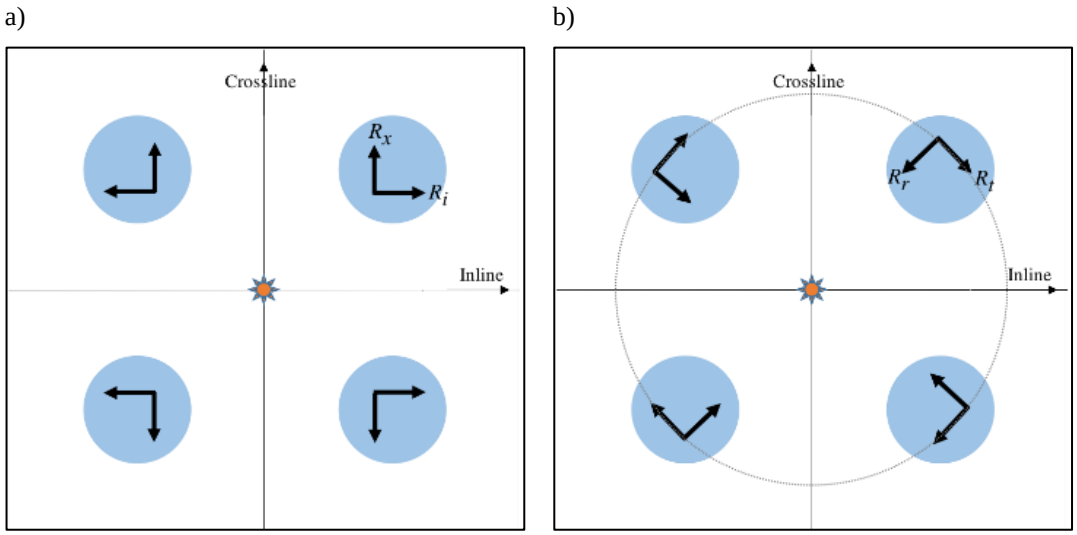

Figure 2-6 Difference between SV-mode polarisation in each acquisition quadrant for a) inline (*Ri*) / crossline (*Rx*) coordinates and b) radial (*Rr*) / transverse (*Rt*) coordinates.

2.1.7 P-wave Source and Generated Waves Types

In land seismic data acquisition, a P-wave source using vertical vibrators, weight drops, thumpers or explosives is most frequently used. These sources distort the subsurface vertically. Even though vertical sources are called P-wave sources, they generate more SV than P-wave energy. This being so, direct SV energy is considerably more robust than the P energy (Hardage and Wagner, 2014). The energy distribution between P and SV-waves using a vertical (P-wave) source is shown in Figure 2-7. From Figure 2-7 it can be seen that the zone vertically below the P-wave source is poorly illuminated by the SV radiation.

To detect and use direct SV mode energy generated by vertical sources, 3C geophones should be used and recording times must be lengthened to allow for the later arrivals of slower SV data when compared to faster P data. In practice it is necessary to design a specific survey geometry to accommodate and also utilise the differences in P and SV wave radiation patterns to achieve improved illumination of the subsurface.

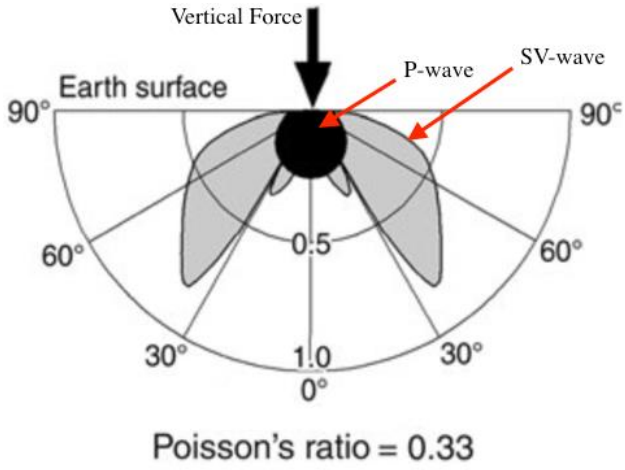

Figure 2-7 P and SV radiation patterns (direct-P and direct-SV waves) produced when a vertical force is applied to the surface of an isotropic earth (horizontally traveling energy along the earth-air interface is ignored). Although the vertical-sources are viewed as P-wave source, they produce more SV energy than P energy. Note that the area beneath the source is not illuminated by SV radiation. (after (Hardage and Wagner, 2014)).

2.1.8 Potential for Improved Spatial Resolution

Theoretically, an image with better spatial resolution should be captured using the S-wave data in comparison to P-wave data of the same frequency bandwidth. For any given frequency *f*, the wavelength λ, of S and P-wave data are:

$$\lambda_S = {}^{V_S}/_{f}, \tag{2-21}$$

and

$$\lambda_P = {}^{V_P}/_{f}. \tag{2-22}$$

As S-waves are slower than P-waves, they have shorter wavelengths in comparison with P-waves (and potentially better spatial resolution). However, the S-wave bandwidth is usually narrower than the bandwidth for P-waves due to:

$$Q_P > Q_S, \tag{2-23}$$

where Q_P and Q_S are quality factors (inverse of attenuation) for P- and S-waves respectively. As a result, the wavelength as well as spatial resolution of both can be similar. This is the case for surface sources. For downhole surveys (VSP and particularly cross-hole) most of the propagation paths are through fresh rock with high Q values for either mode. Even for reflection surveys there are instances where the S-wave data have roughly the same frequency bandwidth as their companion P-wave

data resulting in the S-wave data generating images with higher spatial resolution than those of P-wave data ((Malehmir et al., 2015; Brodic, 2017).

2.2 Multi-component Data Processing

For 9C data (isotropic media), there are no differences between P-wave and S-wave data processing as the common-midpoint (CMP) concept used for P-waves (with an assumption that the velocity of the downgoing and upgoing waves are the same) is still valid for the processing of pure SH-SH and SV-SV data.

For 3C data, the velocity of the P-waves (downgoing wavefield) is not equal to the velocity of the converted SV-waves (traveling upwards). Hence, the principles of CMP processing are not valid. A different common-reflection point gathering strategy is required. This is achieved through the application of the common-conversion-point (CCP) concept.

The ability to process CCP data is limited to a few service companies and research groups. It has not progressed as much as CMP data processing making future advancements in CCP data processing a necessity for 3C and 4C technology. Moreover, the effectiveness of the CCP concept in complex hard rock environments has not been fully evaluated (Thomsen, 1999; Stewart et al., 2003; White et al., 2012; Malehmir et al., 2015; Brodic, 2017).

To process the S-wave data in a multi-component dataset a mathematical rotation of the source and receivers to a fixed direction is required. For an isotropic media, this rotation is from inline/crossline space to radial/transverse space. For inline/crossline (data-acquisition) space a mix of SV and SH modes are recorded, whereas in radial/transverse space SV and SH modes will be separated as pure modes.

2.2.1 CMP vs. CCP Processing

Historically, particularly in the oil and gas industry, CMP-based processing software has been developed and successfully utilised for single-mode P-P imaging (Yilmaz 2001). In simple terms CMP processing is applicable to any data in which the velocities for the down- and up-going waves are the same. Hence SV-SV and SH-SH data can be processed using conventional P-wave CMP-based seismic software.

Figure 2-8 illustrates the differences in the ray paths for CMP and CCP imaging in a horizontally-layered media. It is important to note that the CMPs are midway between the source and receiver whereas for CCPs their spatial position varies with depth. This is a result of the velocity of the downgoing wavefield (V_P) being higher than the upgoing wavefield (V_{SV}). As a layer boundary gets shallower, based on Snell's law, CCPs get closer to the receiver station (Figure 2-8b). The data comprising a CMP can be summed together (stacked) to improve the signal to noise ratio. However, as CCPs are not midway between the source and receiver, summing is not possible.

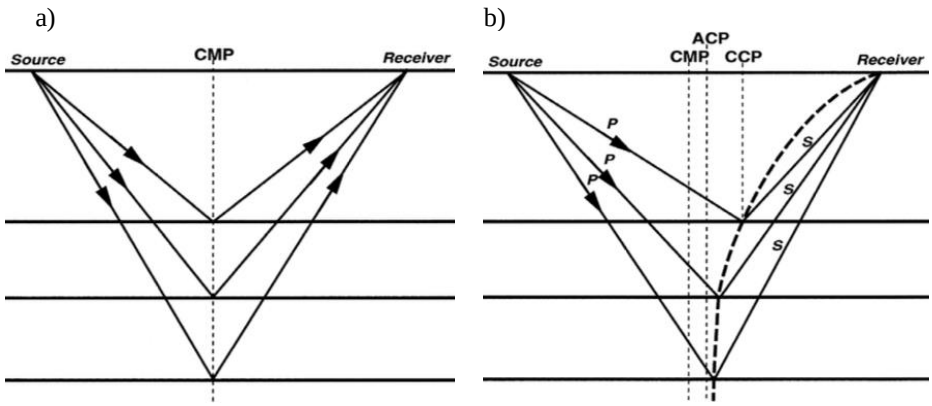

Figure 2-8 Geometry of a) CMP image points (vertical dashed line), and b) CCP image points (curved dashed line)**.** For deeper conversion points the difference between Asymptotic (common) Conversion Point (ACP) and CCP will be reduced. (After (Yilmaz 2001))

By convention, a "positive offset" occurs when the receiver is located ahead of the source, in the shooting direction. For the SH-waves the right-hand rule is commonly used (Urosevic, 2000). However, any rule can be used as long as it is consistently applied to all available data.

Having a knowledge of the propagation direction from the source station to the receiver station is helpful in understanding the distinction between CMP and CCP data velocity analyses.

Using a simple dipping layer model emphasises the significance of respective positioning of the source and receiver (Figure 2-9). As P- and SV-wave velocities (V_P and V_{SV}) are different and they travel along different raypaths, a different methodology is needed for the CCP S-wave velocity estimation than the ones used for CMPs.

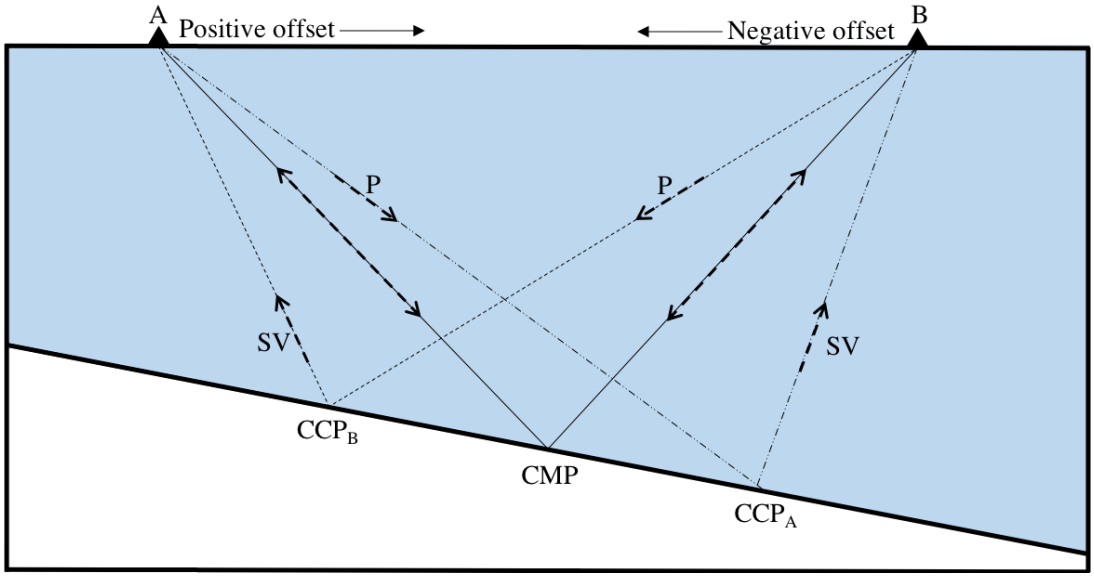

Figure 2-9 Difference between travel times for CMP and CCP locations and their associated raypaths. Note that there are two CCP locations for positive and negative offsets as a result of the P and SV following different raypaths.

Figure 2-9 shows that for CMP velocity analysis the velocities and the travel times of the raypath will be the same for negative and positive offset directions even if the source and receiver positions are swapped. This being so, the stacking and migration velocities for positive-offset and negative-offset directions in CMP image processing will be the same. For CCP velocity analysis, the raypath geometry is different. Figure 2-9 illustrates the ray paths for the P-SV mode in CCP imaging. The velocities of the downgoing (P) and upgoing (SV) waves are different and they follow different raypaths for positive- and negative-offset directions. The CCP positions are different for both offset directions. This being so, different CCP stacking and migration velocities and stack positions (CCP_A and CCP_B) will be required for positive-offsets and negative-offsets.

2.2.2 Source and Receiver Rotation

As stated above, for 3D/3C acquisition, a mathematical rotation of the source and receivers is required in order to separate the different modes (Figure 2-10). Inline and crossline terminology is derived with respect to the survey acquisition coordinates, referred to as H1/X and H2/Y, respectively.

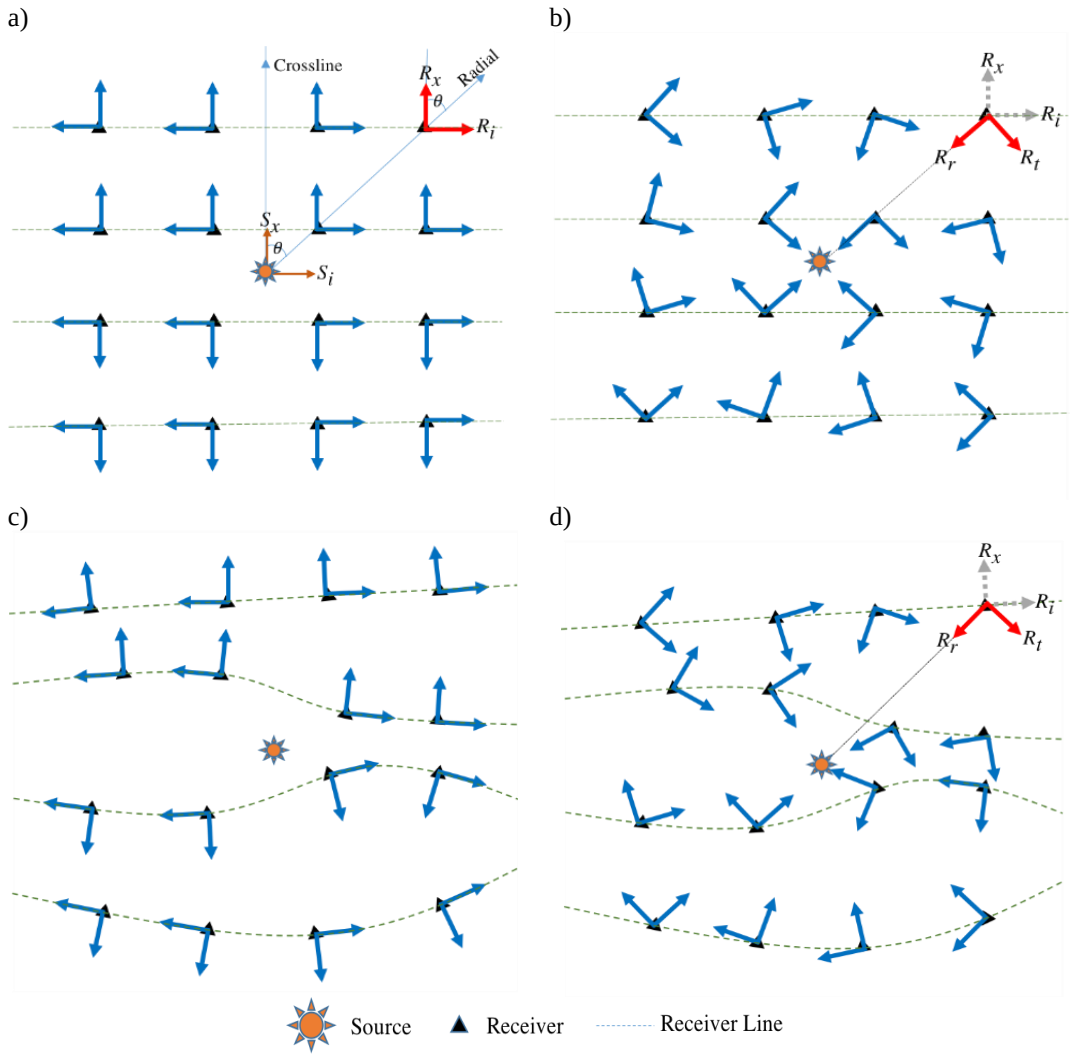

Figure 2-10 Rotation from inline(R_i)/crossline(R_x) data-acquisition coordinates, a) ideal case and c) actual case, to radial(R_r)/transverse(R_t) coordinates, b) ideal case and d) actual case. In order to separate the mixed SH and SV modes the rotation to radial/transverse data space should be performed, in which the radial component heads toward source location.

Figure 2-10a illustrates the model to depict the separation of SH and SV by a mathematical rotation for 3C/3D data.

The field data (F) can be denoted as a mix of two horizontal source vectors (S) and two horizontal receiver vectors R:

$$F = \begin{bmatrix} S_i R_i & S_x R_i \\ S_i R_x & S_x R_x \end{bmatrix}, \tag{2-24}$$

where i stands for the inline and x for crossline directions. The outcome of the rotation is D which is the radial/transverse coordinates data space:

$$D = \begin{bmatrix} S_r R_r & S_t R_r \\ S_r R_t & S_t R_t \end{bmatrix}, \tag{2-25}$$

where *r* stands for radial and *t* for transverse directions using the rotation matrix *M*,

$$M(\theta) = \begin{bmatrix} \cos\theta & \sin\theta \\ -\sin\theta & \cos\theta \end{bmatrix}, \tag{2-26}$$

where θ is the orientation angle. If the orientation angle is assumed to be equal in both inline and crossline directions, the forward model equation F in field coordinates is:

$$\boldsymbol{F} = [M(\theta)]\boldsymbol{D}[M^T(\theta)]. \tag{2-27}$$

From this equation it can be seen that there is a projection of *D* natural modes into the field-coordinate system defined by the orientations of source and receiver stations. The assumption for equations 2-26 and 2-27 is that the receiver lines are oriented from north to south and the measurement for the angle θ is clockwise from the north (Figure 2-10). θ will be calculated for all source and receiver stations.

The assumptions for the mathematical rotation described below are:

1. Source and receiver vectors are orthogonal
2. S_i is aligned with R_i and S_x is aligned with R_x
3. 3C geophones are right-handed and orthogonal with a set of *XYZ* sensors and the *Z* axis pointing downward.

Consider the properties of the rotation matrix *M*:

$$M^T(\theta) = M^{-1}(\theta) = M(-\theta), \tag{2-28}$$

D can be calculated from *F* as:

$$\boldsymbol{D} = [M^T(\theta)]\boldsymbol{F}[M(\theta)]. \tag{2-29}$$

In order to apply an inversion onto the projections of equation 2-27, $M^T(\theta)$ is responsible for rotating the receiver coordinate system, which are the columns in matrix *F*, and *M(θ)* is responsible for rotating the source coordinate system which are the rows of matrix *F*. Assuming orthogonality between source and receiver vectors, an interchange can be applied to the rows and columns of *F* and *D*, as well as *M* and M^T matrices without changing the result. MacBeth and Li (1996) describe a rotation

technique for non-orthogonal source and receiver vectors.

When considering a P-wave (vertical displacement) source, the downgoing P-wave as well as its companion SV-mode, propagate in all azimuths uniformly. There is no need to rotate source vectors since the source propagation is symmetrical. Hence *F* can be simplified to:

$$\boldsymbol{F} = \begin{bmatrix} \boldsymbol{SR_i} \\ \boldsymbol{SR_x} \end{bmatrix} \tag{2-30}$$

where S is the downgoing P-wave. Therefore, for 3C data, only the receiver coordinates are required to be rotated from inline/crossline coordinates to radial/transverse coordinates:

$$\boldsymbol{D} = [M^T(\boldsymbol{\theta})]\boldsymbol{F}. \tag{2-31}$$

2.2.3 CMP vs. CCP Stacking

In seismic processing, stacking is one of the most important steps to improve the signal to noise ratio. This is vital where large amounts of noise occur; commonly the case in a hard rock environment.

CMP based algorithms are predominantly used in the industry. This being so, most commercially available data processing software packages provide different and robust CMP based stacking algorithms. CCP based algorithms are still under development and there are very few commercially available software packages available, which include CCP stacking algorithms.

Figure 2-11 shows a vector source generating SV at the source station. The downgoing and upgoing raypaths will be the same (SV) and CMP stacking concepts are applicable. For a source only generating P, the downgoing raypath will be different from the upgoing one (P and SV, respectively) and CCP stacking is required.

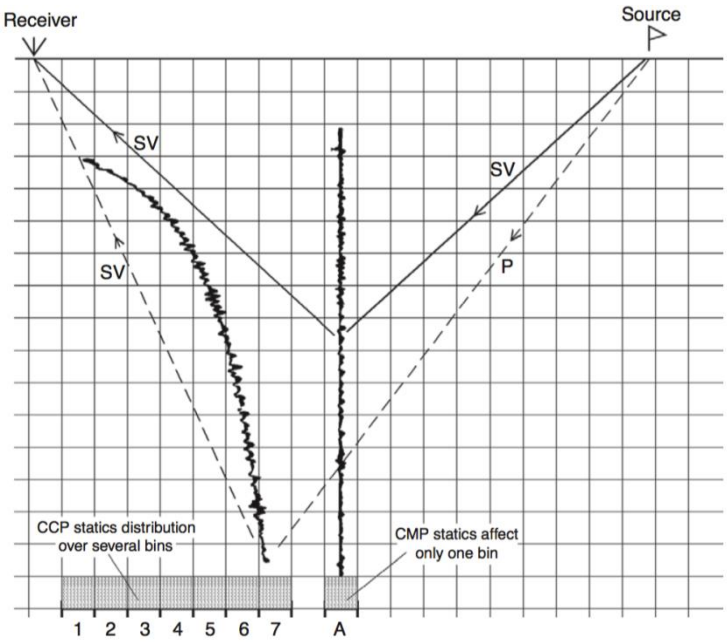

Figure 2-11 CCP imaging versus CMP imaging. Comparison of CMP image trace (confined to stacking bin A) and CCP image trace (curved across stacking bins 1 through 7). (After (Hardage et al., 2011)).

2.2.4 Asymptotic (common) Conversion Point (ACP) Binning

The example presented in Figure 2-11 shows that the CCP image trace is spread across bins 1-7. In CCP binning, bin numbers and coordinates (bins 1 to 7 in Figure 2-11) are placed into the trace headers which were initially used to store CDP numbers and coordinates for P-wave processing. Calculation of depth varying conversion points (CCP) is very complex and time consuming. It also requires very accurate estimation of V_P/V_S.

To reduce complexity, an asymptotic binning method is used as an approximation where ACP coordinates are calculated from CCP coordinates for the deeper data where the CCP image traces are almost vertical. In order to stack the data, all trace points are then aligned to ACP coordinates for a single bin (bin 7 in Figure 2-11). This approximation will not be valid for shallow data as the binning error will be higher than the deeper data. Figure 2-12 shows a comparison of CMP, ACP, and CCP concepts.

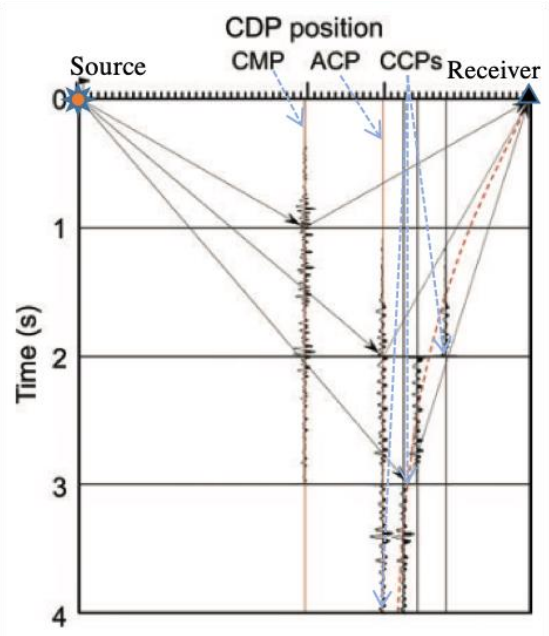

Figure 2-12 CDP gathering point locations for CMP, ACP, and CCPs. (after (Gaiser, 2016)).

2.2.5 Gamma Functions

The V_P/V_S ratio, commonly known as gamma for the CCP method, governs the curvature of CCP coordinates in 3C processing. In order to calculate depth varying CCP coordinates, the gamma functions should be known for each point. Moreover, gamma functions will be different for negative- and positive-offsets since the V_P and V_S velocities are offset dependant.

For a simple model in a homogeneous medium (Figure 2-13), based on Snell's law:

$$\frac{\sin\alpha}{\sin\beta} = \frac{V_P}{V_{SV}} \tag{2-32}$$

The following equation is valid for the raypath geometry:

$$\frac{\tan\alpha}{\tan\beta} = \frac{X_P}{X_{SV}} \tag{2-33}$$

where X_P and X_{SV} are the distances from source and receiver stations respectively. If the incident/reflection angles are small $\tan\alpha = \sin\beta$ and equation 2-34 can be derived.

$$\frac{X_P}{X_{SV}} \sim \frac{V_P}{V_{SV}} \tag{2-34}$$

This relation will be more complex for large angles of incidence/reflection.

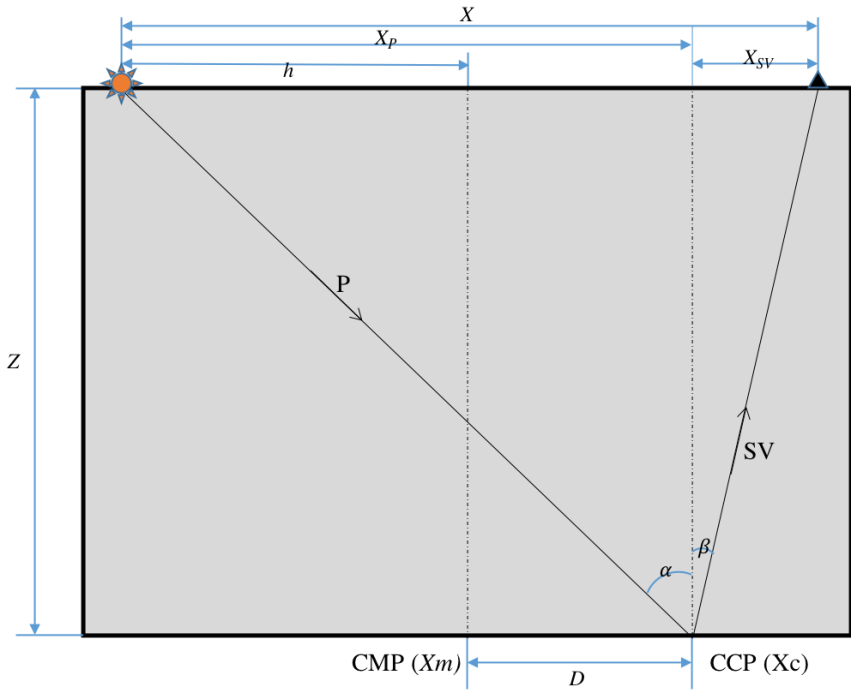

Figure 2-13 Simple, straight-raypath model showing that the position of the CCP is controlled by the V_P/V_S ratio.

2.3 Converted Waves - Processing Challenges in a Hard Rock Environment

The processing and interpretation of 3C data has become feasible with recent technological advancements. However, compared to conventional P-wave processing, there are still issues to be resolved such as the processing time to carry out CCP binning, polarity changes, receiver reorientation, static calculation, velocity analysis, depth conversion as well as improvement of imaging. The presence of anisotropy and shear wave splitting further complicates processing. Some of these issues are discussed below.

2.3.1 Data Polarity

For 3D split-spread acquisition, the horizontal component detectors, will record the data in opposite polarities in the inline direction either side of the source. In the crossline direction the polarity will change with lateral offset, centred around a traverse connecting the source to the receiver. Hence all receivers need to be rotated onto to

the inline-crossline coordinate system before the polarity can be reversed.

For 2D split-spread acquisition, it is only necessary to reverse the polarity of the data recorded on one side of the shot. Figure 2-14 illustrates the polarity differences for the vertical and horizontal components.

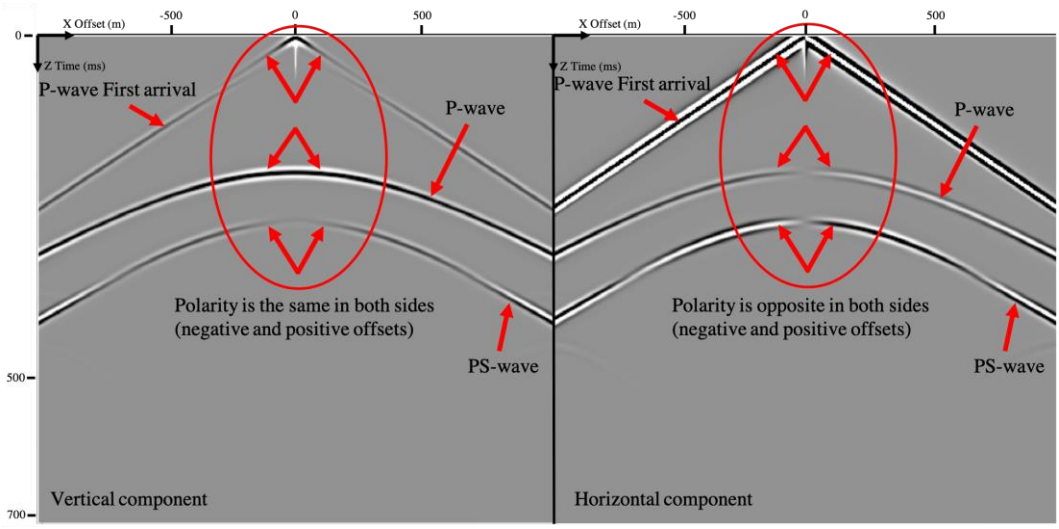

Figure 2-14 Polarity difference for reflected and converted waves. S-wave first arrivals are suppressed for illustration purposes.

2.3.2 Statics

For vertical processing, the static solution is calculated from the P-wave refracted arrivals and is refined using residual static corrections. After application of the statics, event coherency and continuity will be improved.

For converted wave (S-wave) statics, the identification and picking of refracted first arrivals is difficult as they occur after P-wave arrival(s). The calculation of residual statics is also made difficult as a result of variations in the CCP coordinates with depth. In favourable conditions which can be found in some parts of Yilgarn Craton of WA, converted wave statics may not be the issue due to a sharp contrast between regolith and the fresh rock, with no velocity gradient (Urosevic, 2018; personal communication).

Figure 2-15 shows an example for P (PP) and PS static solutions for a 2D line. PS detector statics vary between ±150 ms whereas the PP detector statics are less then ±10 ms.

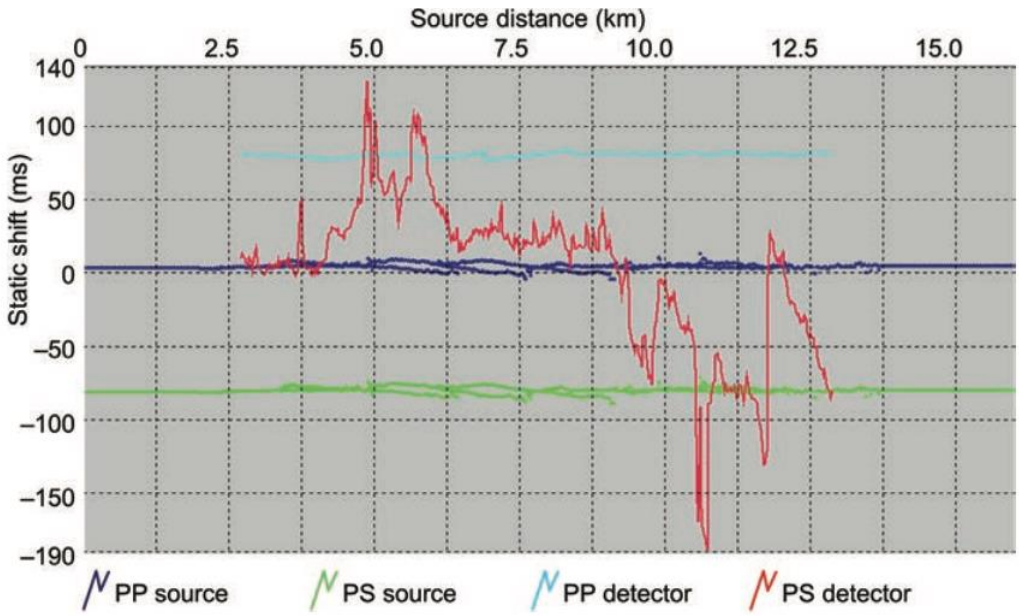

Figure 2-15 Difference between P- and converted S-wave static solutions (after (Gaiser, 2016)). Note - for display purposes, 80ms has been added to the PP detector solution, and 80ms has been subtracted from the PS source solution.

It can be seen from Figure 2-15 that the source statics can be correlated for P and S static calculation. However, S-wave receiver statics are occasionally large with short wavelength variations and totally uncorrelated to P-wave receiver statics. One way to estimate the S-wave statics is to consider a V_P/V_S ratio and calculate the S-wave receiver statics from the P-wave receiver statics. This approach will not fully resolve the issue. However, mixing this approach with some corrections applied on the final image will improve the quality of the final image.

Another way to calculate near-surface S-wave velocity models for land data is to invert surface waves using multichannel analysis of surface waves (MASW). This approach can provide a reasonably accurate S-wave velocity model in the near surface. However, the S-wave static solution may not correlate well with the equivalent PS-wave statics solution (Muyzert, 2000).

2.3.3 PS Binning

A number of approaches to compute the exact CCP locations have been proposed since the 1980s.

From Figure 2-13 X_m is the coordinate of the midpoint and the conversion point is X_C. For the depths (Z) much greater than the distance between the source and receiver (h)

in a simple horizontal and homogeneous medium (proposed by Fromm et al., (1985) and derived by Tessmer and Behle (1988)):

$$X_p = \frac{X}{1+r}, \tag{2-35}$$

where $r = \frac{V_S}{V_P}$ and $X_C = X_M + D$, and D is the horizontal deviation from midpoint. Equation 2-32 can be also written as:

$$D = \frac{1-r}{1+r}h, \tag{2-36}$$

Equations 2-35 or 2-36 are commonly used to compute ACP points as well as first order approximations for CCP locations. It should be noted that *D* is independent of depth (*Z*). The exact positions of CCPs are derived from a fourth-order equation for *D* (equation 2-39). Based on Snell's law:

$$\frac{\sin\alpha}{V_P} = \frac{\sin\beta}{V_S}, \tag{2-37}$$

and in triangles SAX_C and RAX_C we have $\sin\alpha = \frac{h+D}{\sqrt{Z^2+(h+D)^2}}$ and $\sin\beta = \frac{h-D}{\sqrt{Z^2+(h-D)^2}}$, respectively. Then, assuming $r = \frac{V_S}{V_P}$ one can write:

$$\frac{r(h+D)}{\sqrt{Z^2+(h+D)^2}} = \frac{h-D}{\sqrt{Z^2+(h-D)^2}}. \tag{2-38}$$

If we square both sides of equation 2-33 the fourth order equation for D can be achieved (XU and MA, 2002):

$$D^4 + (Z^2 - 2h^2)D^2 - 2\frac{1+r^2}{1-r^2}Z^2hD + h^2(h^2+Z^2) = 0, \tag{2-39}$$

Equation 2-36 has only one real root on $\left(\frac{1-r}{1+r}h, h\right)$.

General analytical solutions to equation 2-39 are complicated and computationally time consuming. Moreover, for a series of layers a numerical approach is required. As a consequence, different iterative solutions have been developed.

Zhang and Robinson (1992) proposed a numerical approach to approximate the CCPs iteratively where $\gamma = \frac{V_P}{V_S}$:

$$X_C^{(new)} = \frac{\sqrt{\gamma^2 + \left(X_C^{(old)}/Z\right)^2 (\gamma^2 - 1)}}{1 + \sqrt{\gamma^2 + \left(X_C^{(old)}/Z\right)^2 (\gamma^2 - 1)}} X \,. \tag{2-40}$$

MA Zai-Tian (1997) approximated D more accurately based on Taylor's expansion:

$$D \approx \frac{1-r}{(1+r)\left[1-(4rh^2)/V_S^2 t_C^2\right]}, \tag{2-41}$$

where t_C is the travel time of a converted wave. This formulation does not work effectively and serious errors are encountered when $h > Z$.

XU and MA (2002) proposed a more accurate formulation for D as:

$$D \approx \left[1 + \frac{4rh^2}{(1+r)^2 Z^2 + 2(1-r)h^2}\right] \frac{1-r}{1+r} h \tag{2-42}$$

Tessmer and Behle (1988) proposed a formulation to compute Z as a function of γ (Falkovskiy, 2015).

$$Z = \sqrt{\frac{\gamma^2 - 1}{\frac{1}{(X - X_P)^2} - \frac{\gamma^2}{X_P^2}}} \,. \tag{2-43}$$

The explicit form of this formulation has been employed for this research project and was implemented by SeisSpace® software as a converted wave processing module.

It is apparent from the above that one of the main issues when binning CCP locations is a dependence upon the V_P/V_S ratio. This ratio is often unknown and cannot be inferred from conventional processing. As the quality of final section depends on the binning method and a knowledge of the V_P/V_S ratio, Schafer (1993) proposed the use of numerical modelling. A simple model was used to compare the different binning methods. An exact single layer formulation was used to calculate the correct CCP locations to re-position each sample point. Figure 2-16 shows Schafer's final results for a specific geological model using three different binning methods (CMP, ACP, and CCP).

a)

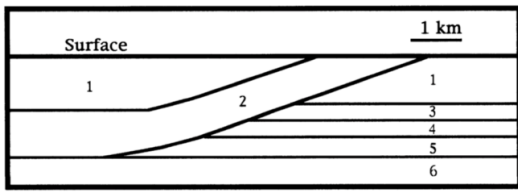

Formations	V_P(m/s)	V_S(m/s)	Density (kg/m^3)	Thickness (m)
2,6	5500	2894	2800	1000
1	3884	2044	2550	1200
3	4300	2529	2650	230
4	4000	2139	2600	270
5	4200	2545	2650	300

b)

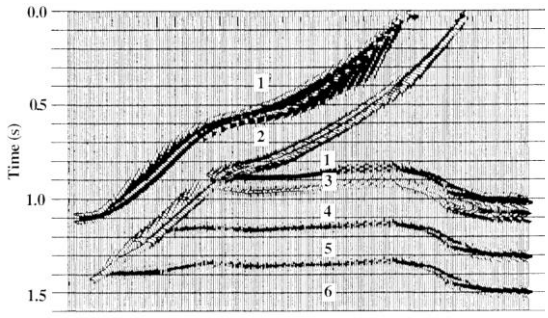

c)

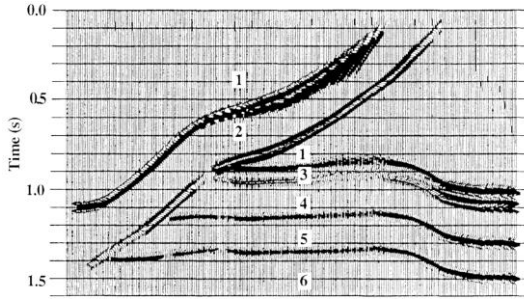

d)

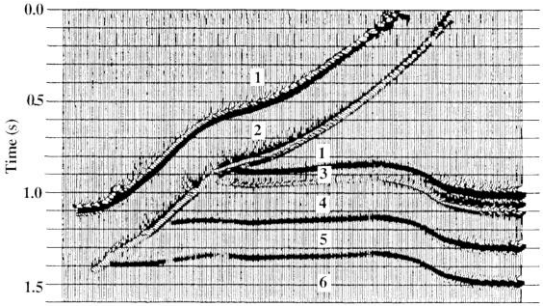

Figure 2-16 Comparison of different binning mechanisms using modelled data. (a) Thrust-fault model and the physical parameters of a simple P-SV synthetic-seismic model. Seismic section using (b) CMP binning, (c) ACP binning, (d) CCP binning. (after (Schafer, 1993)).

From Figure 2-16 it can be seen that the CCP binning method provided the best result compared to the other methods as it solved depth-dependent common conversion points. It should also be noted that the CMP and ACP methods produced acceptable results. This is related to the use of a simple model. In much more complicated real-world environments, smearing of the shallow data is very likely using the ACP method, static corrections will be difficult to resolve and the CMP method will not produce acceptable results.

2.4 Some Remarks

One of the most important factors to improve the signal to noise ratio is the number of traces (fold) in a gather that can be summed together (stacked). High fold is particularly important when processing data from a hard rock environment where there are usually high velocities with small velocity contrasts between geological structures below the near surface weathered zone, combined with high levels of coherent noise (surface waves), as well as a very high velocity contrast between the near surface

weathered zone and the fresh rock. Multiple energy further contaminates the converted refracted and reflected wave energy. This being so and the fact that the converted waves are more affected by above mentioned issues, converted wave processing is much more involved and sensitive to errors than P-wave processing.

2.5 Processing Flow

Following is a summary of the general processing flow used for the 2D and 3D case studies discussed below:

1. Read in the data and convert to the local format
2. Geometry assignment

This step is similar to the one used for conventional P-wave processing. However, more attention is required to separate the different components and correctly populate the trace headers (geo_comp in SeisSpace®) (Figure 2-17). Note - the geo_comp value for inline (X), crossline (Y) and vertical (Z) components were set to 1, 2 and 3 respectively.

3. Receiver orientation and rotation

The initial azimuths of the source and receivers (source–receiver azimuth) and inclinations were calculated and copied to the trace headers. These were then used to rotate the horizontal components of the receivers so that one component was aligned with the source and the other was perpendicular to the source. Any issues with the data polarity were resolved at this stage, and the different modes of S-waves (SV and SH) separated (assuming isotropy).

4. Refraction Statics

For the 2D case study, summation of the P-wave statics for the source and S-wave statics for the receivers (calculated from product of $\frac{V_P}{V_S} = 1.9$ and half of the P-wave receiver statics) was used.

For the 3D case study, the same procedure was used with $\frac{V_P}{V_S} = 1.6$. To improve the final results a combination of a hand-picked horizon and an estimation of an initial V_P/V_S using MASW was carried out on a sample cross line data from the horizontal component (X).

5. Other issues and conventional Pre-Processing

The polarity issue for the 2D data was resolved by reversing the polarity on positive side of the spread. Other pre-processing steps followed a conventional flow to remove coherent noise, suppress surface waves and balance the frequency of the data.

6. Construct PS velocity from P velocity

A constant $\frac{V_P}{V_S}$ ratio was used to create an initial PS velocity function from the P-wave velocity data. It was anticipated that there would be little variation in the ratio in a hard rock environment (Urosevic, 2017, personal communication).

7. PS binning

ACP binning was carried out on CMP gathers for the 2D case study. For the 3D case study, 3D CCP binning was used.

8. Normal Move-out (NMO)

For the 2D case study, NMO was applied using the P velocities. For the 3D case study, the PS velocities were used.

9. Stack

For the 2D case study data, an initial stack was generated using the converted wave data. Dip-moveout (DMO) was applied to the data to generate a DMO stack using the DMO STACK module.

The 3D STACK module was used for the 3D case study data.

10. PS to P time conversion

For the 3D case study data, the stack was transformed into P time domain using the assumed $\frac{V_P}{V_S}$ ratio of 1.6. For the 2D case study data the transformation was carried out post migration (depth conversion).

11. Migration

The maximised component (SV) for the 2D data and both horizontal components for the 3D data were migrated. Pre and post-stack time and depth migrations were trialled.

a)

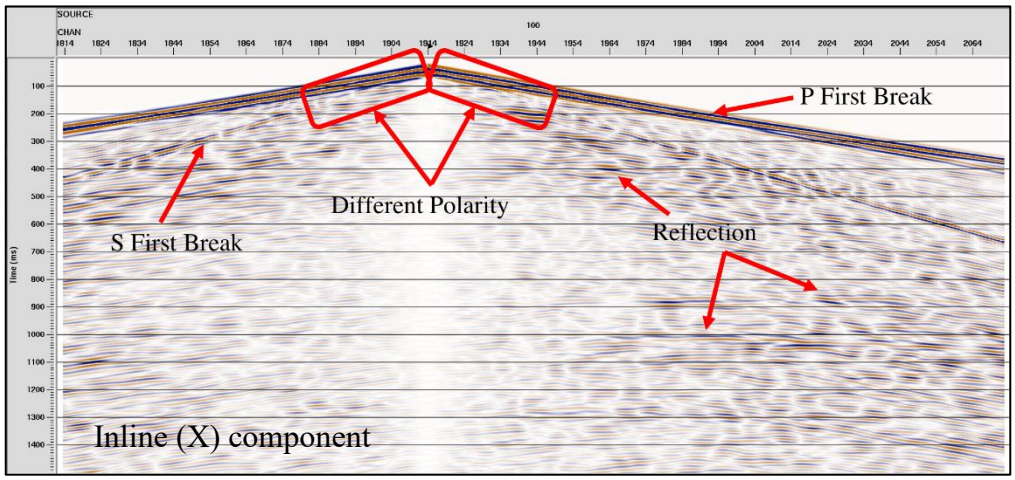

b)

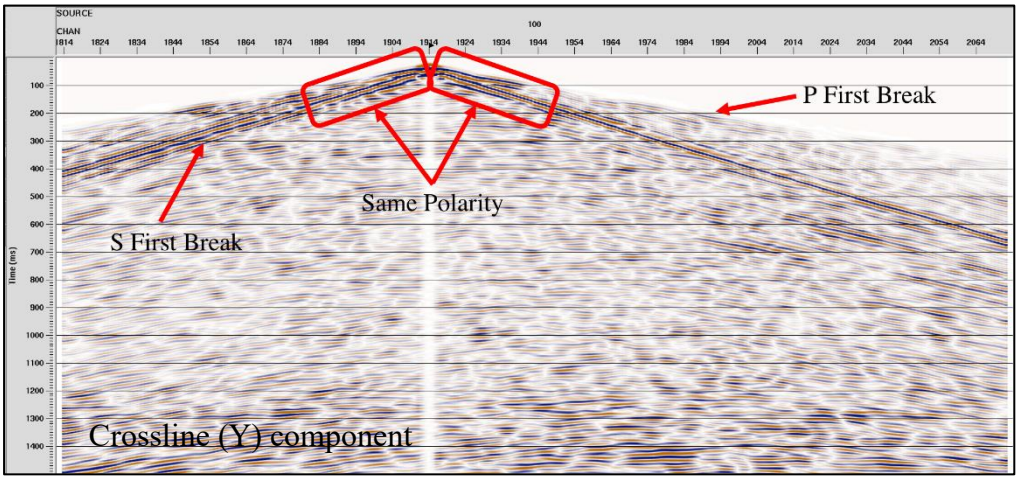

c)

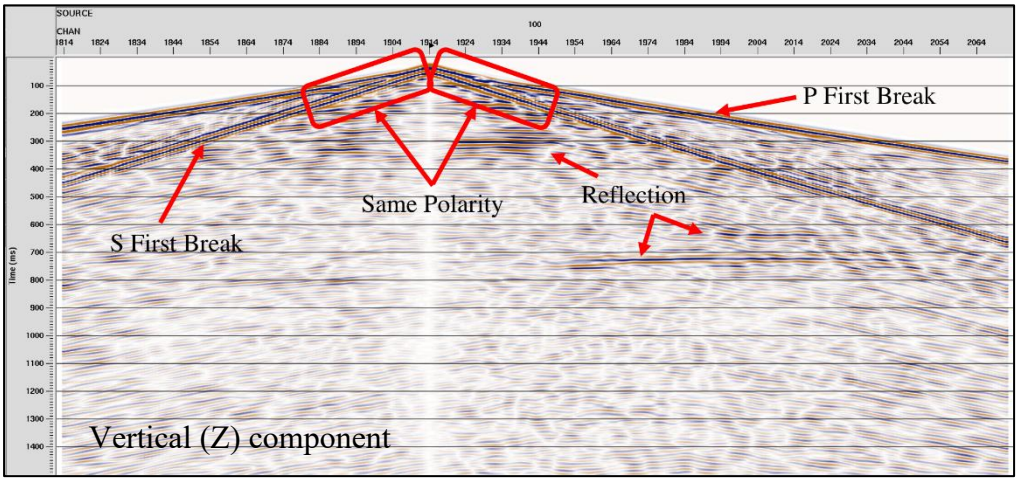

Figure 2-17 A sample synthetic 3C shot gather. a) inline (X) - geo_comp=1, b) crossline (Y) - geo_comp=2 and c) vertical (Z) - geo_comp=3. The following can be observed:

- The P first break amplitude is lowest in Y component,
- There is a polarity difference on either side of the shot point in X component (a).
- A marker reflector is shown by arrows in Z and X components.

Chapter 3 2D/3C MSDP10 Case Study

3.1 Introduction

Following is a case study using data from two 2D (3C) seismic lines.

A series of boreholes were drilled along the southern Gowler Ranges margin (South Australia) targeting electromagnetic (EM) anomalies (Figure 3-1c and d). This program was supported by DET CRC innovative technologies. In 2016, as a part of the programme, two parallel low impact 2D seismic lines (Figure 3-1d) were acquired passing over borehole MSDP10. The lines were located 10m apart either side of a local track. Both vertical and horizontal components of the seismic line located north of the track were processed. The southern line was processed using the vertical component.

The purpose of this is case study is to determine the potential and applicability of multi-component seismic for exploration of mineral resources by analysing all stages of a multi-component survey from survey design and acquisition to data processing and, to some extent, interpretation.

The author participated in the design of the survey and was involved in the acquisition of the data. Processing was carried out using Landmark SeisSpace® seismic processing software. Some additional code was developed and used in MathWorks' MATLAB software package.

3.2 Geological Setting

Fabris et al., (2017) stated: "The Gawler Range Volcanics (GRV) is considered in two main packages: the lower GRV and the upper GRV. The lower GRV includes dacitic to rhyolitic lavas and ignimbrites, tuffs, volcaniclastics and lesser mafics, and comprises successions at the southern Gawler Ranges margin (Waganny Dacite (WD) and Bittali Rhyolite (BR)). The upper GRV is less variable both compositionally and with respect to volcanic facies. It is volumetrically dominated by three regionally extensive felsic lava flows; the Eucarro Rhyolite (ER) and the Pondanna Dacite (PD) and Moonaree Dacite (MD) members of the Yardea Dacite (YD) (Allen et al., 2003)".

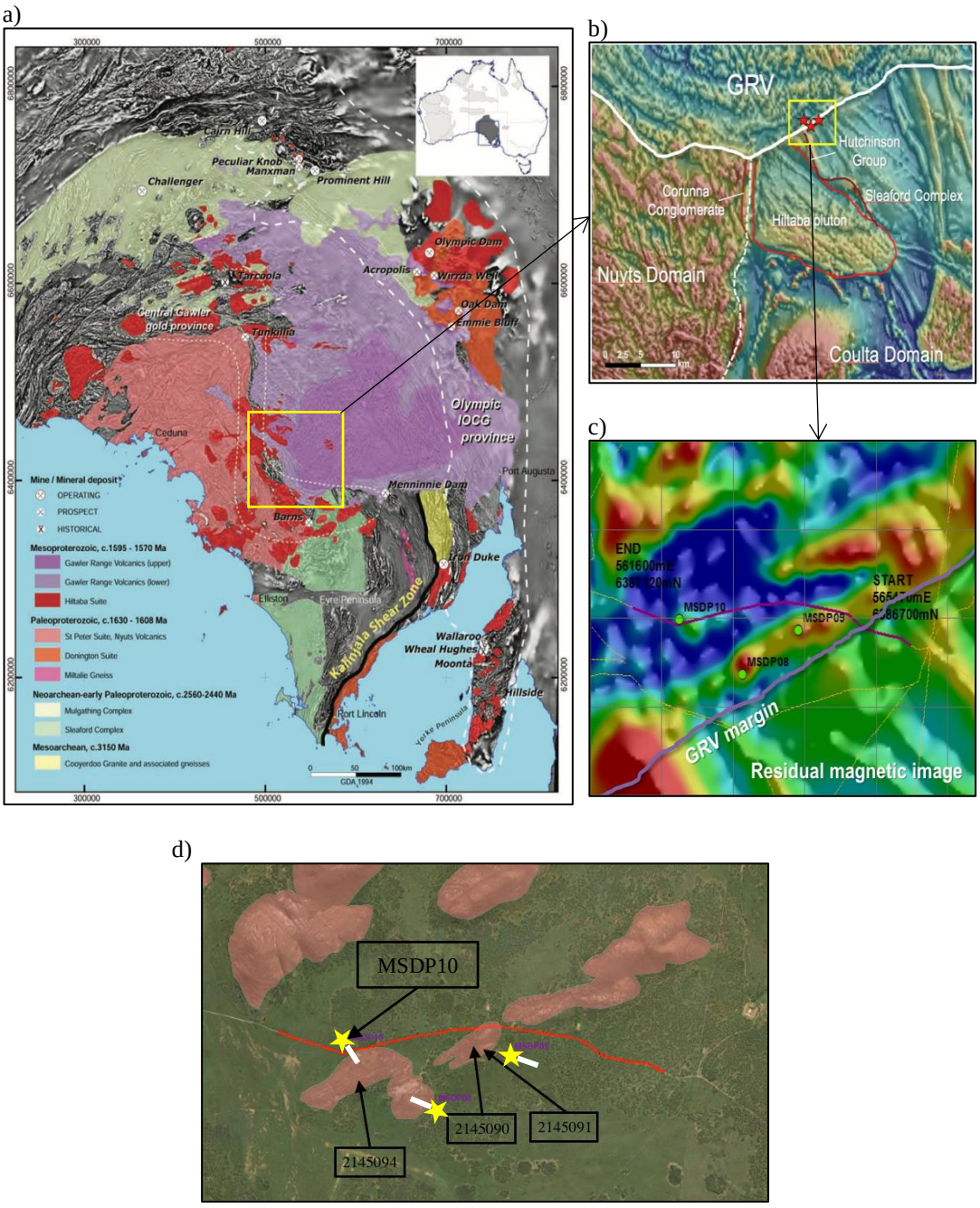

Figure 3-1 MSDP10 area of interest. (a) First derivative magnetic intensity map showing the geology of southern Gawler Craton, South Australia (Reid and Hand, 2012) (b) Aeromagnetic map (c) Residual magnetic image of the survey area. (d) Aerial view of MSDP10 2D lines (lines were located 10m apart either side of the track shown in red), and GRV outcrops (purple) showing sample locations.

The Mineral Systems Drilling Program (MSDP) was conducted in order to develop an improved understanding of the minerals systems formed some 1590 Ma ago during hydrothermal magmatism along the southern Gowler Ranges margin (Fabris et al., 2017) in the northern Eyre Peninsula, South Australia (Figure 3-1). In this region some parts of the basement units are exposed as visible outcrops ((Parker, 2005); Figure

3-1d). Some samples were collected from outcrops near to the area of interest by the Geological Survey of South Australia (Figure 3-2); (Fabris et al., 2017). The location of the outcrops where the samples were collected is shown in Figure 3-1d.

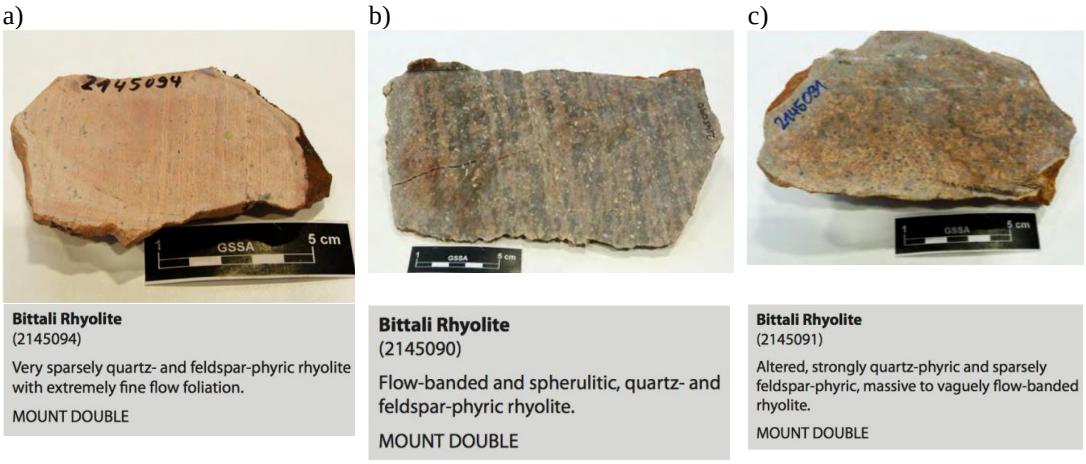

Figure 3-2 Examples of outcrop samples collected by the Geological Survey of South Australia (Krapf et al., 2016). The origin of the samples is shown in Figure 3-1d.

3.2 Acoustic Measurements

The success of converted wave processing can to some extent be estimated by comparing the result to P-wave images. However, this is not sufficient and additional information needs to be obtained from other sources such as borehole data and pre-existing geological models and core samples.

To obtain more information about the link of the geology to the seismic, seven core samples (mix of full and half core) obtained from borehole MSDP10 were provided by the Geological Survey of South Australia.

MSDP10 was drilled to a depth of 567m with an inclination of 60 degrees towards the south-east (Fabris et al., 2017). Drilling intersected Cenozoic alluvial sediments before penetrating brecciated rhyolitic lavas and volcaniclastics of the ER and BR. A diverse range of textures were evident in the BR, some of which were difficult to interpret (Fabris et al., 2017). Volcaniclastic rocks were increasingly common below ~494 m and were interpreted to be of autoclastic and pyroclastic origin. Examples of different textures of BR were observed from the outcrop samples (Figure 3-2) (Krapf et al., 2016). An average specific gravity measured in the borehole of 2.64 g/cc is comparable to the other measurements in nearby holes.

V_P and V_S acoustic measurements were made on the core samples by Dr. Maxim Lebedev in the Rock Physics Laboratory of the Department of Exploration Geophysics at Curtin University. Most of the samples came from zones deeper in the borehole where significant heterogeneity was encountered. Sample depth ranges and descriptions of the samples are shown in Table 3-1. The samples were dried and measurements taken at room temperature in atmospheric pressure. The effect of differential stress on P-wave velocities for compact hard rock samples is deemed as negligible so it was neglected for these measurements (Urosevic, 2017, personal communication). The ultrasonic measurement setup, as shown in Figure 3-3, consisted of two piezoelectric transducers used as a source and receiver (red arrows), a DPR300, Olympus Ltd pulse generator/receiver (blue arrow) and a digital Tektronix TDS 3034C, Olympus Ltd. oscilloscope (yellow arrow). A high frequency signal (1 MHz) generated by the pulse generator was transmitted through the sample using the piezoelectric transducers and then received by the receiving transducer. The waveform (green arrow) was analysed and saved using the oscilloscope. The experiment was carried out along the core (axial) and at three locations crossing the core (radial). The only exception was for sample number 2499659 (the shallowest sample (81m)) with only one measurement across the core due to the size limitation. The length of each sample and weight were recorded and are shown in Table 3-1.

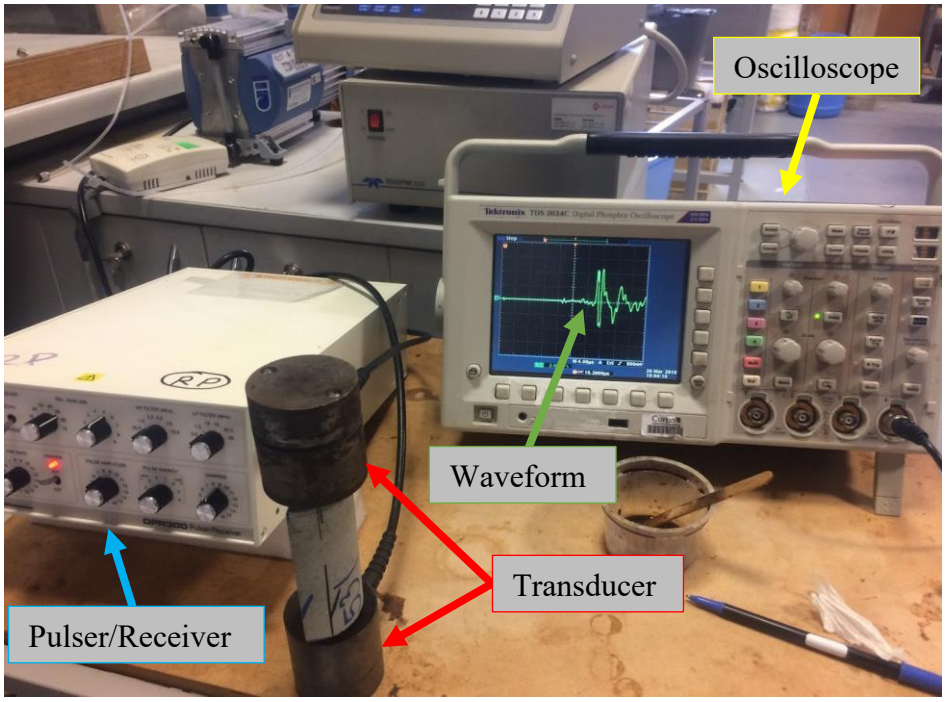

Figure 3-3 Apparatus employed for ultrasonic measurement. Example waveform shown on the oscilloscope is from sample number 2499663 (531m).

A summary of the results for each sample is shown in the Table 3-1. For sample number 2499660, in the axial direction, V_S measurements were unstable as too many reflections occurred. Further work carried out after this analysis is included as part of the discussion below.

Table 3-1 Sample Information. Measurement results and geological descriptions included in the table below were provided by the Geological Survey of South Australia (Adrian Fabris). Radial direction results for each sample are shown in blue.

Ref. Number	Depth (m)	Weight (g)	Vert. Length (mm)	Hor. Length (mm)	VP (m/s)	VS (m/s)	$\frac{V_P}{V_S}$	$\left(\frac{\rho}{\frac{g}{cm^3}}\right)$	Description
2499659	81	467.12	60.77	61.12	5868	3493	1.68	2.64	Red phenocrystic (abundant feldspar and Fe-Mg mineral) rhyolite
					5902	3458	1.71		
2499660	300	238.33	95.67	24.40	5928	-	-	2.65	Red phenocrystic rhyolite
					5970	3640	1.64		
					6055	3569	1.7		
					5925	3576	1.66		
2499661	389	256.16	97.97	25.42	5945	3581	1.66	2.64	Pink-green brecciated, sericite-chlorite altered, quartz-phyric rhyolite. Clasts>40 mm to 1 mm
					5939	3652	1.63		
					5939	3631	1.64		
					5857	3663	1.6		
2499662	490	216.94	103.02	21.34	5794	3560	1.63	2.64	Grey-green, chlorite-sericite-pyrite-fluorite altered, flow banded quartz-phyric rhyolite
					5831	3642	1.6		
					5767	3569	1.62		
					6028	3545	1.7		
2499663	531	200.98	87.62	23.01	5546	3480	1.59	2.62	Yellow sericite altered, quartz-phyric rhyolite with moderately intense, preferential alteration.
					5781	3641	1.59		
					5724	3584	1.6		
					5612	3486	1.61		
2499664	554	504.07	94.96	50.64	5688	3419	1.66	2.68	Fragmental volcaniclastic (volcanic breccia). Matrix-supported heterolithic breccia with angular to sub-rounded clasts. Feldspar-rich matrix.
					5567	3260	1.71		
					5744	3374	1.7		
					5567	3363	1.66		
2499665	566	405.98	77.51	50.68	5626	3397	1.66	2.63	Yellow-brown sericite-altered, brecciated quartz-phyric rhyolite. Clast-supported.
					5547	3477	1.6		
					5572	3385	1.65		
					5993	3733	1.61		

3.2 The MSDP10 Seismic Program

The different orientation directions of the particle displacement vectors of the P-waves and S-waves and the path that each wave uses to propagate explains why they can provide different amounts and types of information about the subsurface. The success of converted wave processing can to some extent be estimated by comparing the results to P-wave images.

The main objective of the 2D (3C) seismic lines was to map and determine depth to basement as available boreholes stopped short of basement. Acquisition parameters are described in Table 3-2.

A wireless recording system using 3C geophones was deployed and a 375 kg weight drop (attached to a bobcat excavator) used as a source (Figure 3-4). Photographs taken during data acquisition and of GRV outcrop are also shown in Figure 3-4.

Table 3-2 2D-3C data Acquisition parameters for the MSDP10 project.

Acquisition Parameters	
Date	May 2016
Geometry	2D line
Sample rate	1 ms
Recording length	3 s
Geophones	3C
Receiver spacing	10 m
Shot spacing	10 m
Source	375kg Weight drop
Shots	400
Active Channels	400
Data format	SEGD

Figure 3-4 Examples of pictures from the field work for MSDP10. (a) bobcat and the 375kg weight drop source, (b) shot point and the result after shooting showing the hardness of the ground. (c) planting 3C geophones, (d) a 3C geophone and the Sercel wireless recording system. (e) and (f) show examples of GRV outcrops, which the survey passed over.

3.2.1 P-wave (Vertical Z Component) Processing

To obtain a reference prior to carrying out the PS-wave processing, vertical component (P-wave) data were processed. The seismic data in SEGD format were reformatted using the SeisSpace® software package and output in SeisSpace® internal format, preserving the original data length of 3 seconds and a 1 ms sampling interval. An initial

assessment of the data quality and a check for the presence of converted waves showed that the data were contaminated by very significant amounts of ambient and coherent noise. Therefore, a key objective of the processing was to attenuate this noise prior to stacking and imaging.

The survey geometry was loaded to a data base and the trace headers. Subsequently a surface consistent deconvolution was applied, followed by a broad-band filter. Trace editing was carried out after the application of deconvolution. In order to avoid killing traces unnecessarily that were contaminated with high amplitude “mono-frequency” noise (emanating from working machines, vehicles, drilling rigs), analysis was carried out in the frequency-wavenumber (FK) domain to identify the coherent noise to be removed by applying an FK Filter. Such traces may be considered too noisy and may be cured, due to high dynamic range of 24-bit acquisition systems and retain for the stacking process.

First breaks to be used to generate an initial P-wave refraction statics model were manually picked within offset ranges ± 1000 m. A significant amount of editing and checking was required before a reasonable result was obtained.

Refractions static were computed utilising a Gauss-Seidel algorithm based on a single layer model. A weathering velocity of 2600 m/s was measured from shot records and a replacement velocity of 6000 m/s (refractor velocity) was estimated from offset ranges 100 m to 800 m. An example shot-gather before and after application of P-wave refraction statics is shown in Figure 3-5. After statics the continuity of all body waves was significantly improved.

a)

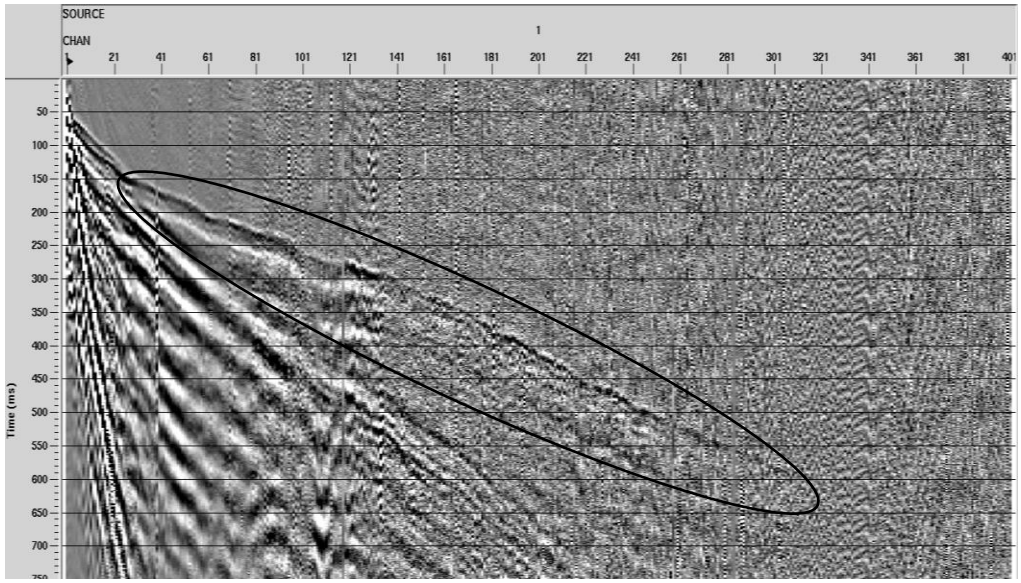

b)

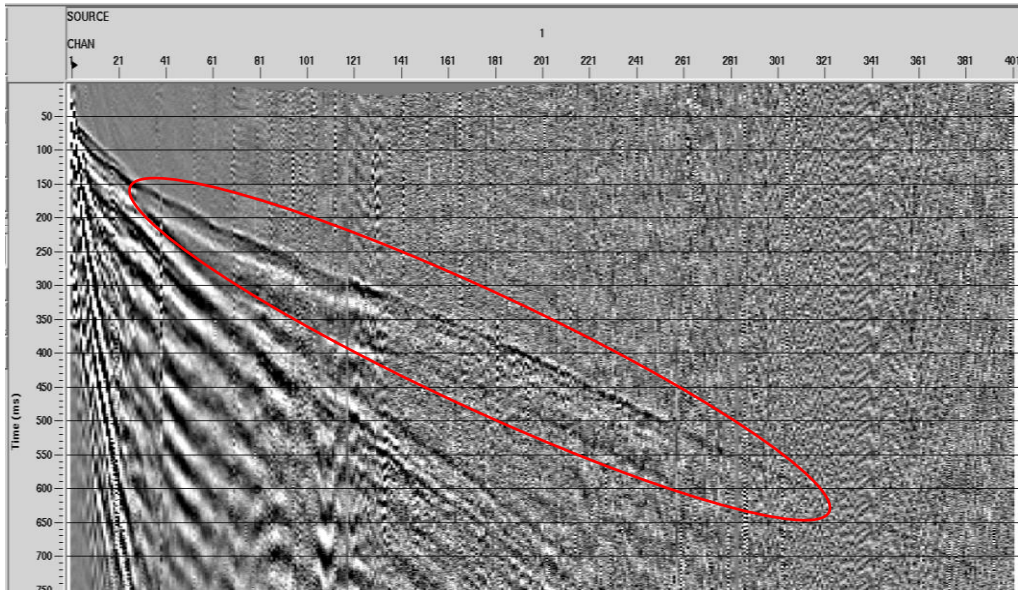

Figure 3-5 Example of a shot record (a) without refraction statics applied (b) with refraction statics applied. Irregularities of weathering thickness and/or lateral velocity changes visible on (a) are successfully corrected after application of statics on (b)

After static corrections were applied, surface waves were attenuated in the frequency domain (Surface Wave Noise Attenuation (SeisSpace®)).

To correct for amplitude decay, a spherical divergence correction was applied. To complete pre-processing, the air wave was surgically muted out. An example shot record before and after pre-processing is shown in Figure 3-6.

a)

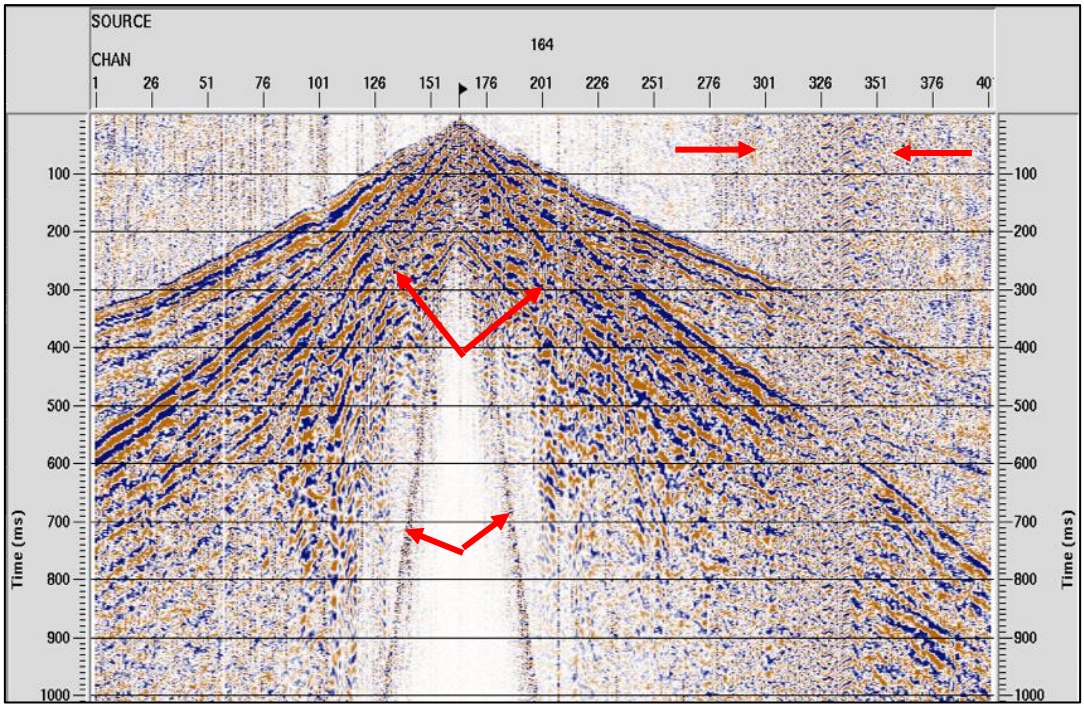

b)

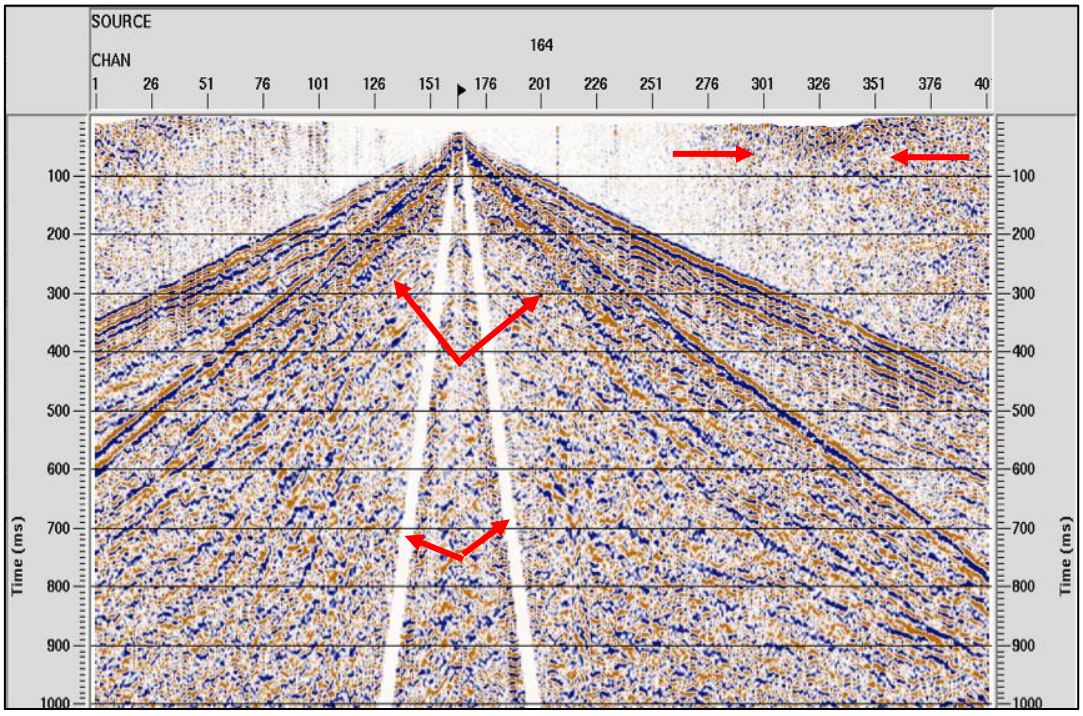

Figure 3-6 An example shot (a) before, and (b) after pre-processing. Red arrows show noise attenuated.

For velocity analysis, it was decided to use constant velocity stacks (CVS) rather than conventional interactive velocity analysis (IVA). The CVS approach is required in hard rock environment as the geology is complex and interactive techniques do not work well (Urosevic et al., 2007). CVS were computed in the velocity range 3000-

7500 m/s with steps of 250 m/s (Figure 3-7). An initial single velocity function was derived by analysing the CVS panels.

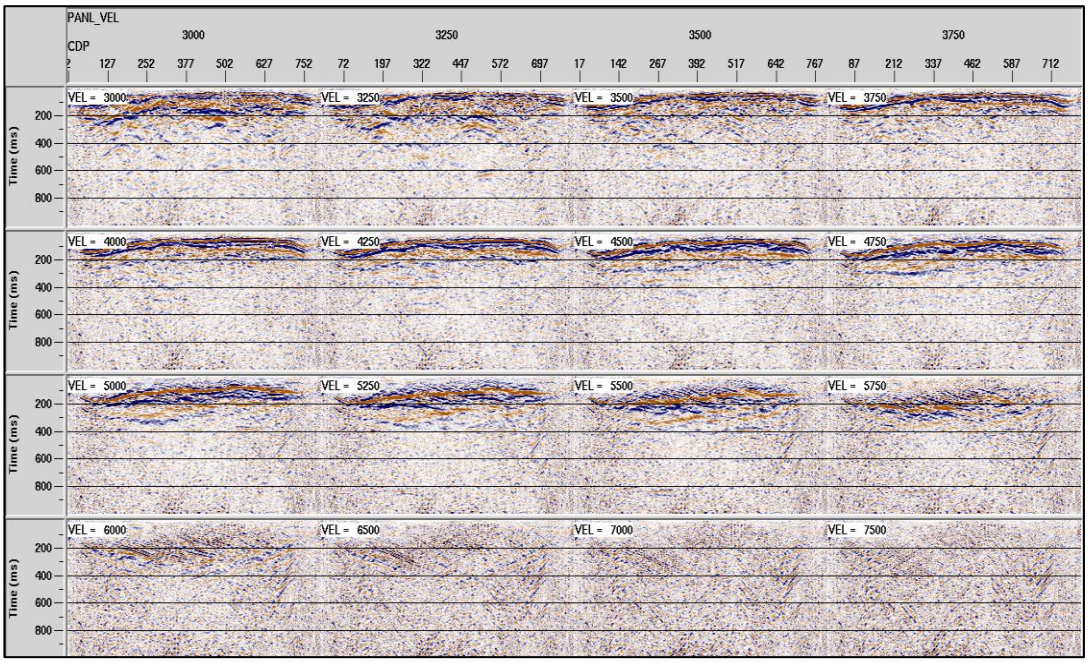

Figure 3-7 P-wave Constant Velocity Stacks (CVS): From 3000m/s to 7500m/s, with step 250 m/s.

A brute stack (Figure 3-8) was then run with a 500ms window robust amplitude scaling AGC (Automatic Gain Control) applied prior to stack. A single 800ms window centred around a target reflector was picked for computation of residual reflection static corrections. Computation of the surface consistent residual reflection statics was then carried out using 8 iterations with a maximum static correction allowed increased from 4 ms to 32 ms for successive iterations to ensure solution stability. A stack after application of residual reflection statics is shown in Figure 3-9.

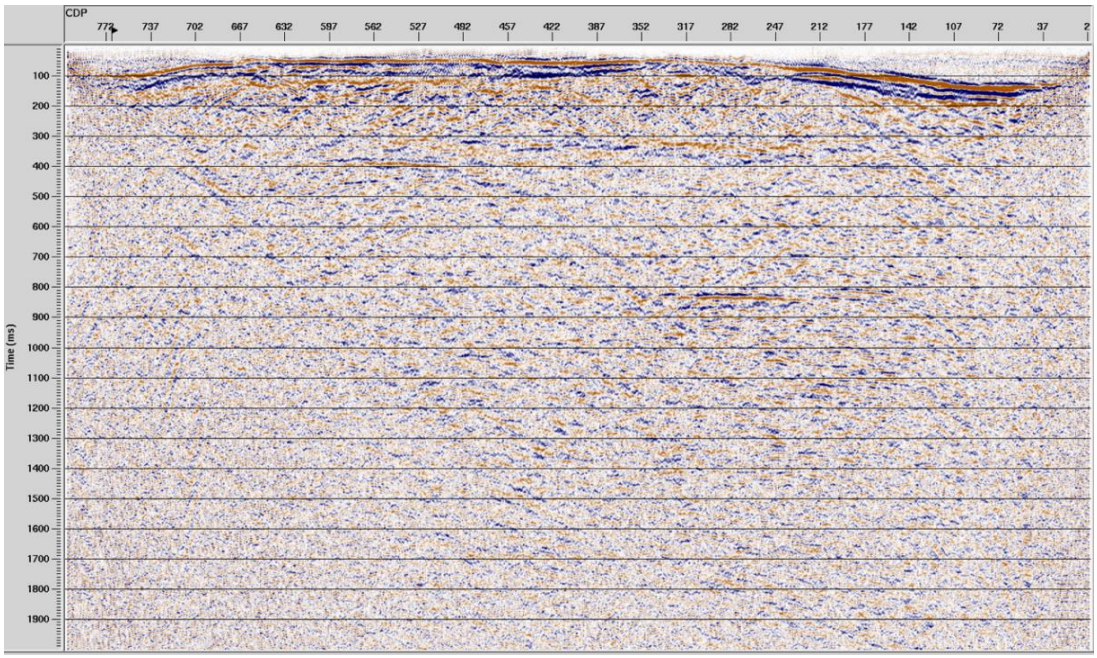

Figure 3-8 Conventional P-wave brute stack with NMO correction using a single velocity function derived from CVS panels.

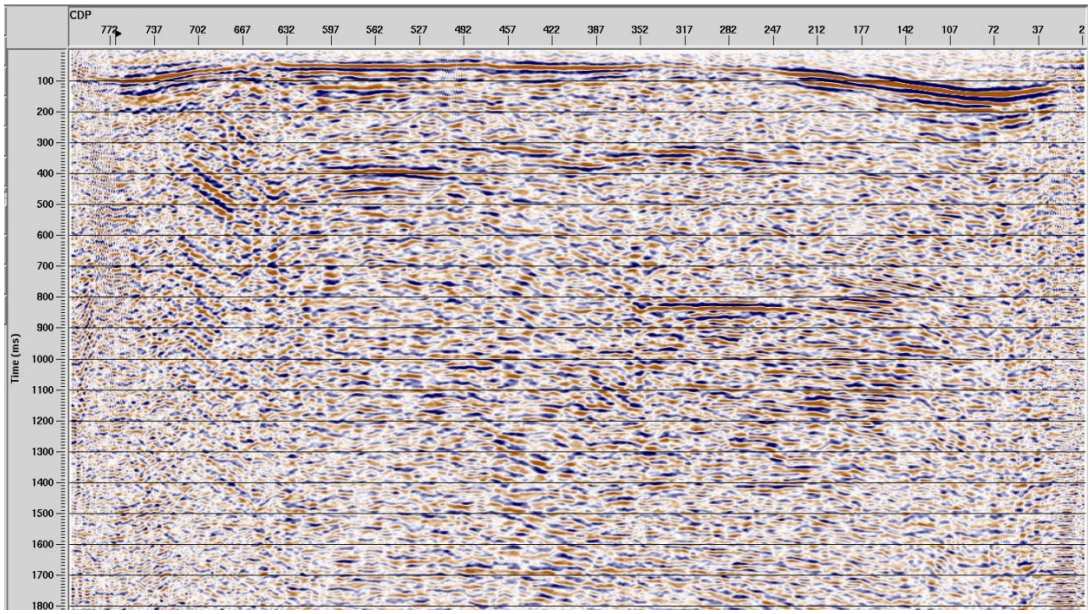

Figure 3-9 Conventional P-wave stack with residual static corrections applied.

A second pass of velocity analysis was carried out after the application of residual and static corrections. It was now possible to use IVA as the initial velocities derived using CVS were used as a guide function (Figure 3-10).

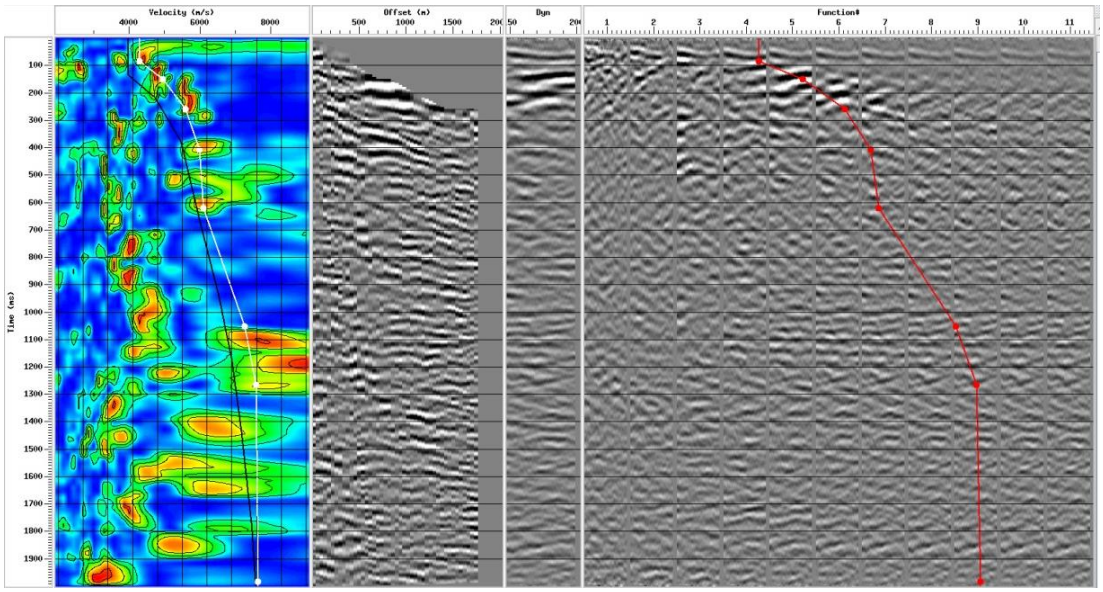

Figure 3-10 Selected CMP location for P-wave Interactive Velocity Analysis.

An AGC using a 350ms window was applied to NMO corrected gathers to equalise the trace amplitudes, and the data were stacked. To improve the SNR, post stack FX deconvolution was applied between 5Hz and 120Hz within a 1000ms window (Figure 3-11).

The stack data were then migrated using a Stolt-FK algorithm and smoothed second pass stacking velocities. Depth conversion was then carried out using the smoothed velocities scaled by 95% (Figure 3-12).

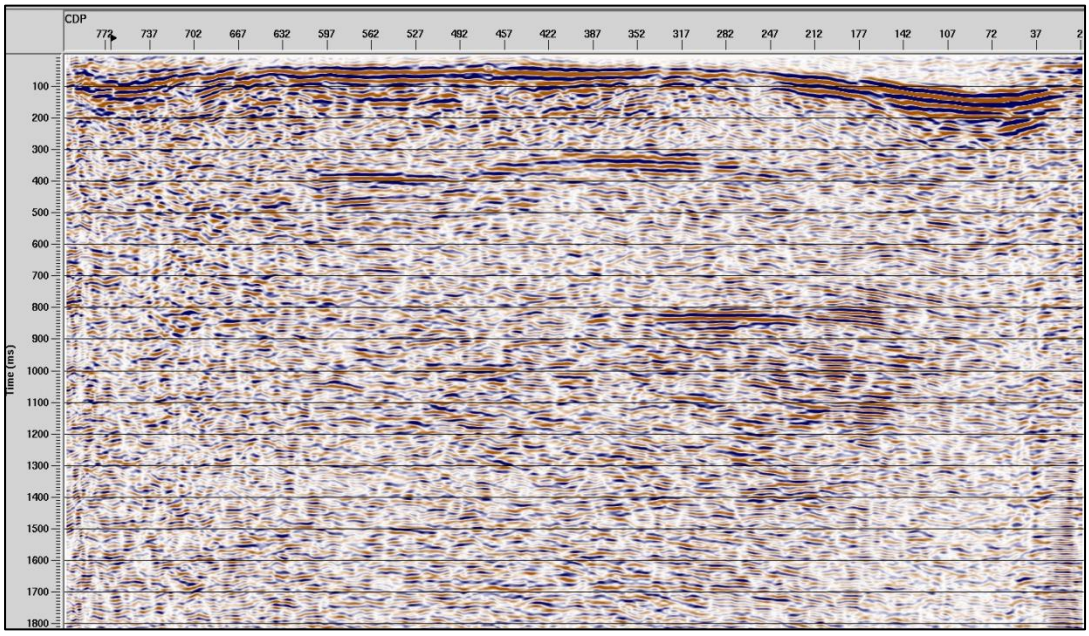

Figure 3-11 Final P-wave stack for MSDP10.

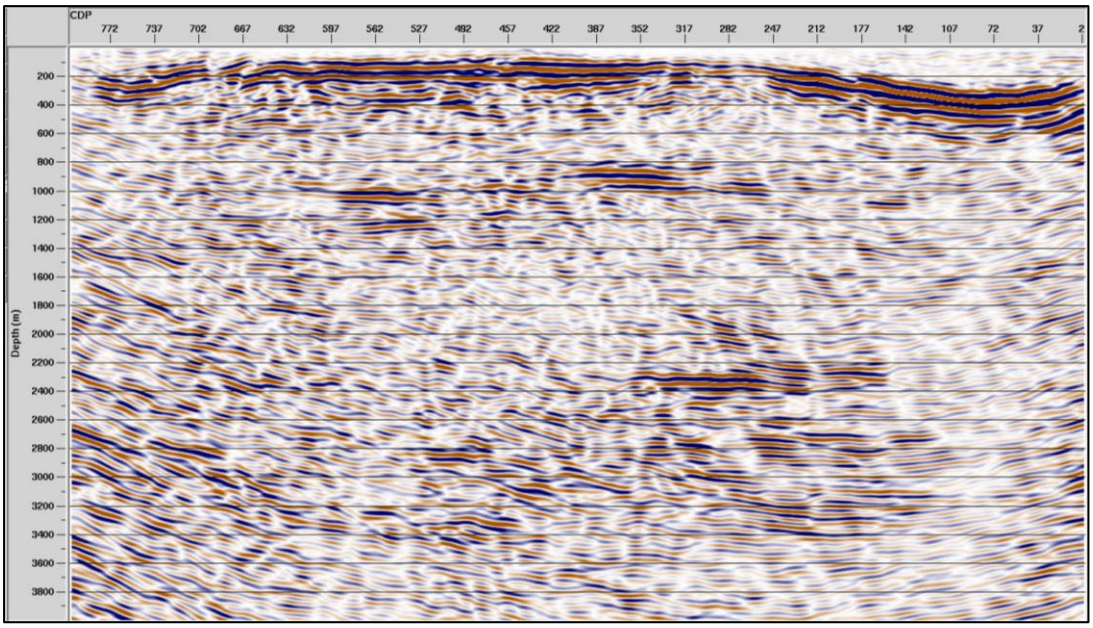

Figure 3-12 Final P-wave Migration in time for MSDP10.

Detailed analysis was carried out at each stage of the processing to ensure optimum parameters were chosen. This was particularly important as 50% of the line was acquired during very poor weather conditions with significant rain and wind adversely affecting data quality. The data were also contaminated with high amplitude ambient and coherent noise common in hard rock environments. Improvements in the data with each stage of the processing showed that the parameters chosen were effective and that maximum information was derived from the data to provide a very good result. Analysis of the data indicated that that S-waves had been generated and occurred even on the vertical components confirming that the data represented a good candidate for further converted-wave processing.

3.2.2 Key steps in the Converted-wave (PS-wave, Horizontal Components) Processing

The processing sequence employed to process the horizontal components (a schematic flow is shown in Table 3-3) is similar to the one used for vertical processing. However, the following are key differences:

- Two steps of receiver rotation analysis
- Refraction statics calculation and application
- ACP binning and polarity reversal prior to stack.

Table 3-3 2D-3C Horizontal processing flow for the MSDP10 project.

Schematic flow used for processing horizontal components
1. Segy_in 2. Merge geometry with seismic
3. Receiver rotation (an algorithm was used which searched for the maximum sum of squares of trace amplitudes.)
4. Refraction statics
5. Match polarity (reverse the polarity on one side of the spread)
6. Pre-processing
7. Construct PS velocity from P velocity (by using a V_P/V_S function)
8. NMO for Converted waves
9. Converted wave STACK
10. Converted wave DMO
11. Migration

Orientation analysis was carried out on the X and Y components based on maximum amplitude or amplitude optimisation with rotation angle. The best outcome was achieved by adjusting the optimisation window length around first arrivals. Example shot records before and after rotation are presented in Figure 3-13.

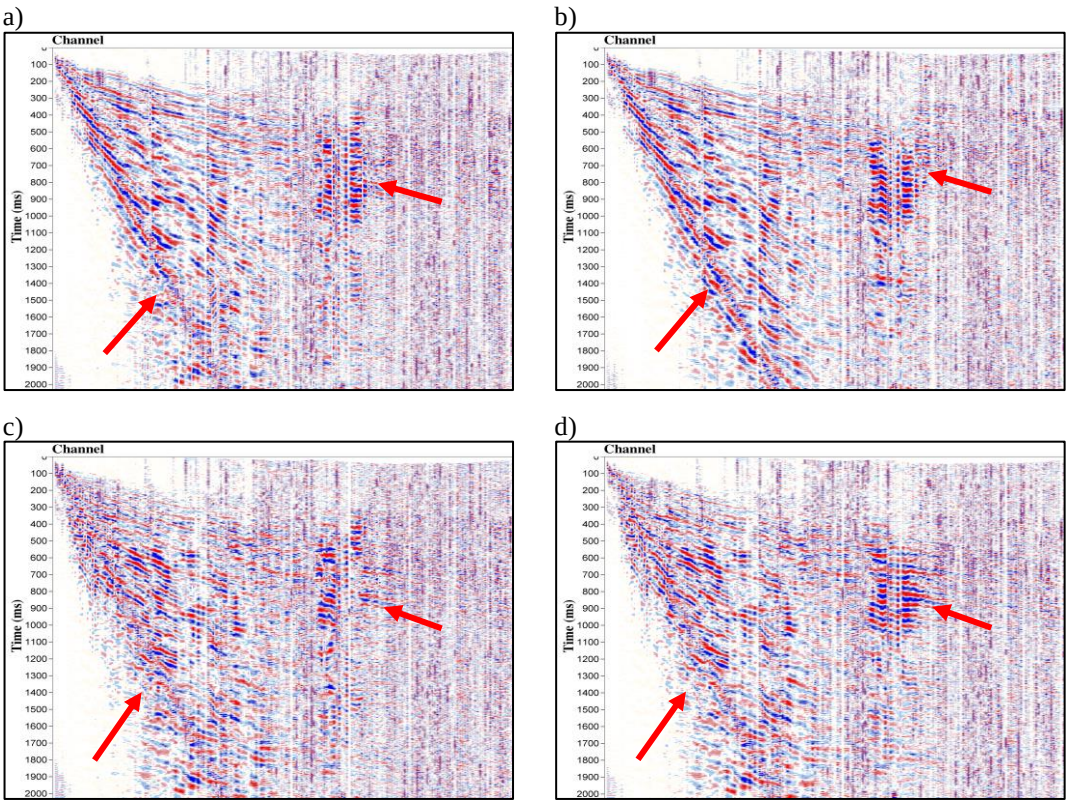

Figure 3-13 Example of a shot record before and after rotation. Horizontal inline component (X) (a) before and (b) after the rotation, and Horizontal crossline component (Y) (c) before and (d) after the rotation. Improved continuity of reflections and surface waves (red arrows) indicates that the rotation was successful.

The angles of rotation for all receivers and for all the shots as well as the RMS energy of traces (derived from arbitrary windows) were monitored. This will be discussed in more detail below in section “additional values of multi-component method” with regard to a better understanding of the subsurface geology and overall quality control of the data.

Converted wave refraction statics were calculated as the ratio of the previously computed P-wave refraction statics. A ratio of $V_P/V_S = 1.9$ was derived using refracted wave analysis (Figure 3-14). The P-wave statics were then applied to the source side, and S-wave statics to the receiver side.

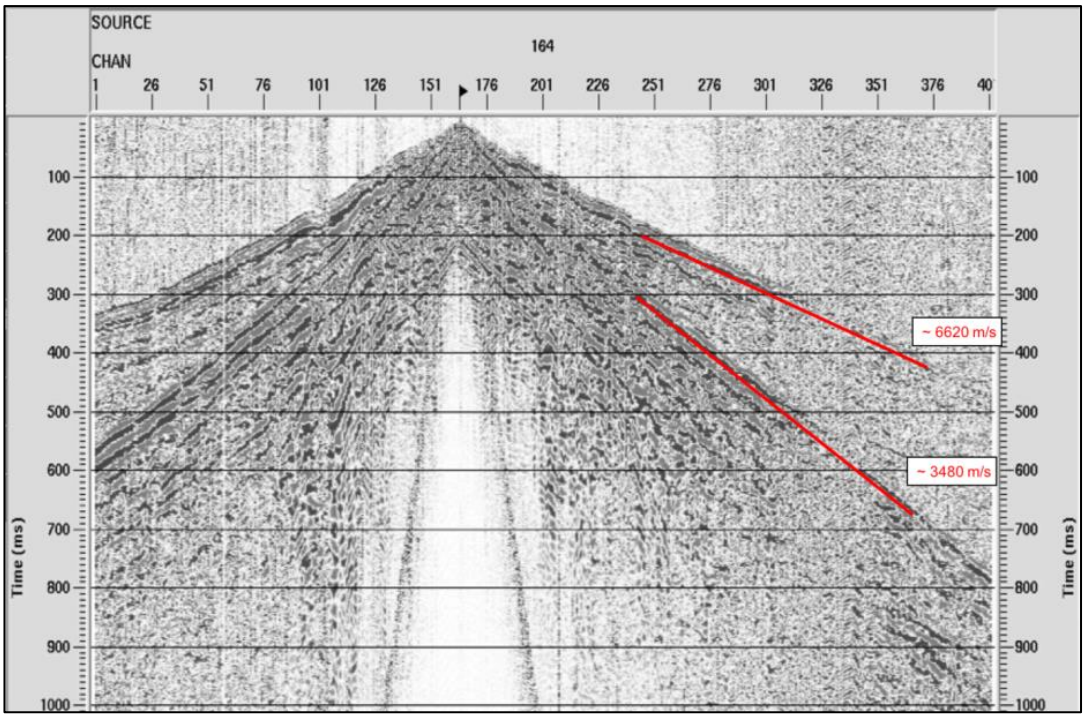

Figure 3-14 Measured P and S velocities to obtain the VP/VS ratio as a parameter used for further converted wave processing. Estimated V_P/V_S ratio was 1.9.

The next step was to determine the location of the P to S conversion points. The ACP binning method was used to create a conversion wave stacking map as s function of V_P/V_S ratio and offset.

Using the same processing sequence and parameters employed for the vertical processing, the horizontal components were stacked and then transformed from PS time to P time and migrated using the smoothed P wave migration velocity. The final results are shown in Figure 3-15.

a)

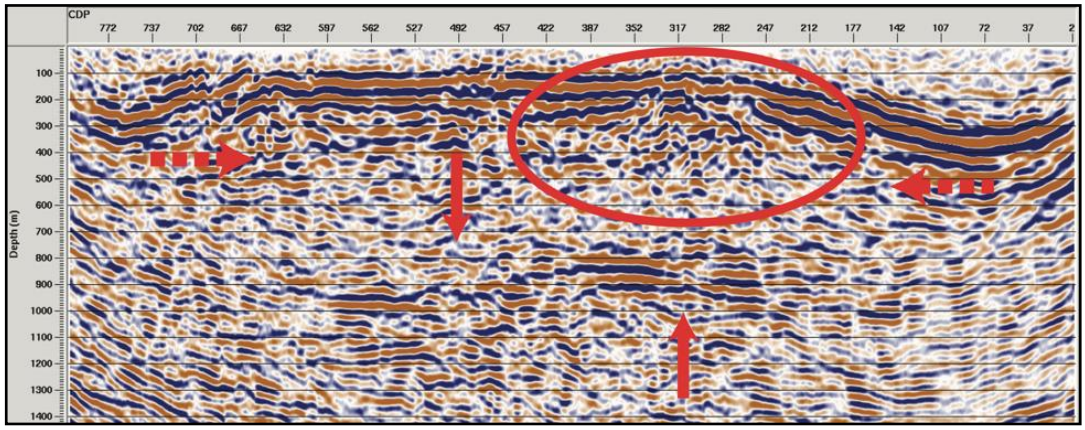

b)

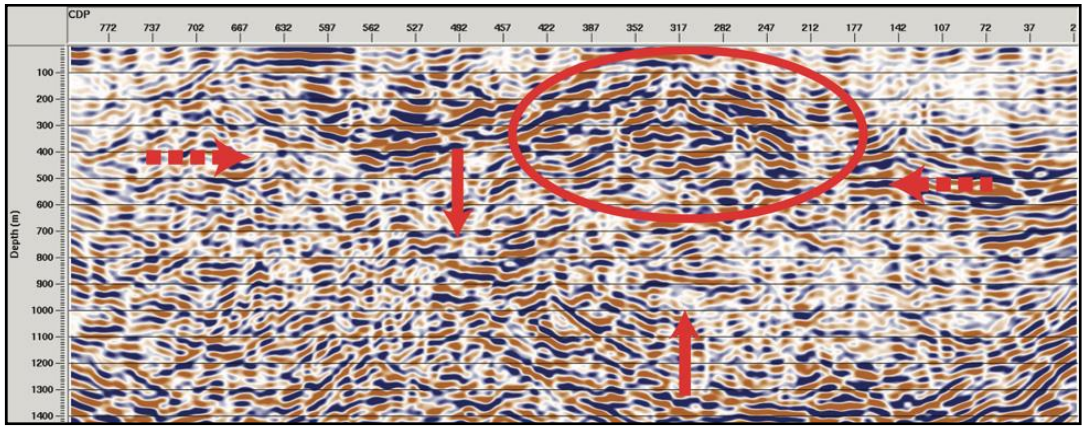

c)

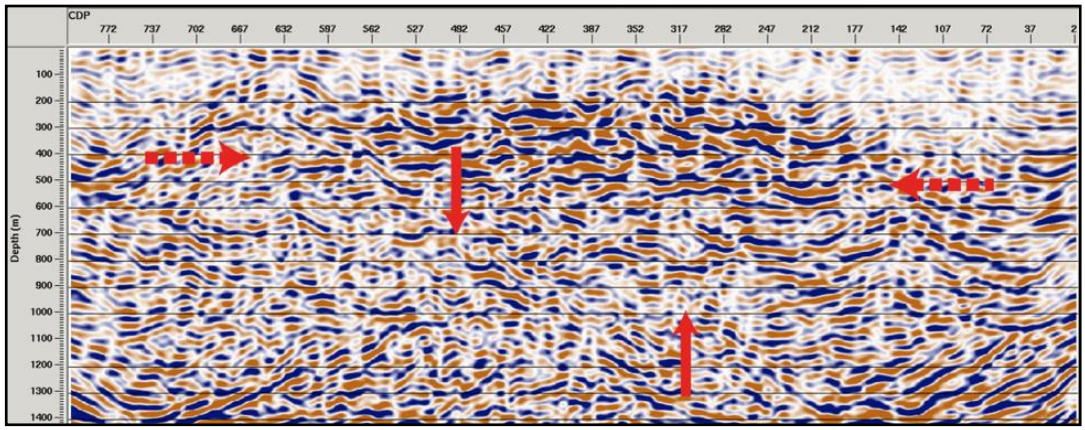

Figure 3-15 Migrated stacks: (a) conventional vertical, (b) horizontal inline (x), and (c) horizontal crossline (y) component. Reflections identifiable for both vertical and horizontal components are shown by red arrows. The converted wave reflectivity appears quite different from the vertical. There could be many geological reasons or deficiencies in processing could cause this. However, it is more important to observe that there is some expression of the structure for both components suggesting that a certain amount of shear wave splitting is present.

3.2.3 Additional Value of Multi-component Method

As part of the processing of the horizontal components, systematic patterns were identified by analysing the rotation angles calculated in MATLAB. The patterns exhibited were unexpected. To analyse these, specific displays were generated with the vertical and horizontal axes representing the number of shots and the number of receivers respectively. The horizontal axis is effectively a function of space and the vertical a function of time (the vertical axis is also a function of space, but it actually represents time as each vertical trace belongs to a shot and time passes for different shots). It was expected that the angle of rotation (Figure 3-16a) would coincide with the shot to receiver azimuth (Figure 3-16b) including random deviations caused by low SNR (ambient noise).

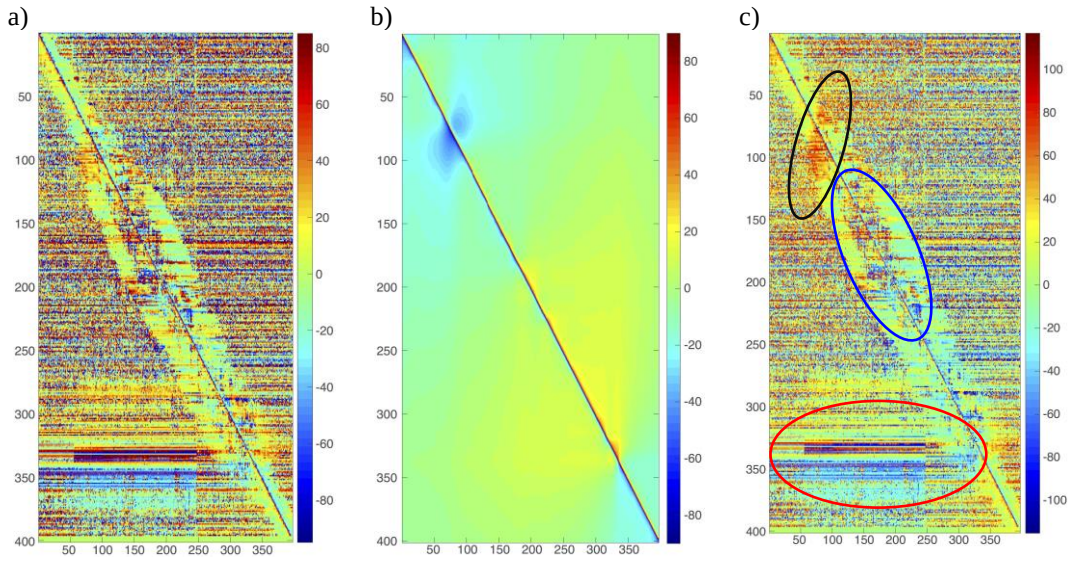

Figure 3-16 (a) calculated angle of rotation, (b) source to receiver azimuth, (c) residual angles obtained by subtracting (b) from (a). Y (time) and X (space) axes represent number of shots and the receivers respectively. the colour bars represent rotation angles/azimuth. Circled areas show systematic features that are a consequence of near surface geology and noise caused by poor weather condition.

The calculated angles of rotation are shown in Figure 3-16a. The source to receiver azimuths were computed from the location coordinates and are shown in Figure 3-16b. From Figure 3-16a, patterns can be observed in space (geological condition) and time (random or systematic noise). In order to eliminate the effect of line geometry, subtraction of the source to receiver azimuth from angles of rotation was carried out and the result representing residual angles of rotation is shown in Figure 3-16c. From Figure 3-16c, it can be seen that a relatively stable zone of variable width occurs near

to the shot and that areas with increased level of noise as a result of decaying levels of energy occur with increasing offset.

Inspection of Figure 3-16c shows that high energy occurs on the near offsets giving rise to relatively stable and cleaner results compared to far offsets. However, on the near offsets some patches with different angles of rotation (black ellipse) and patches with high levels of noise can also be identified (blue ellipses). These are likely to be an effect related to the near surface geology as well as curvature of the receiver line. A significant change in angle of rotation (red ellipse) is also identifiable from Figure 3-16c. This is likely to be associated with very strong winds that occurred during acquisition.

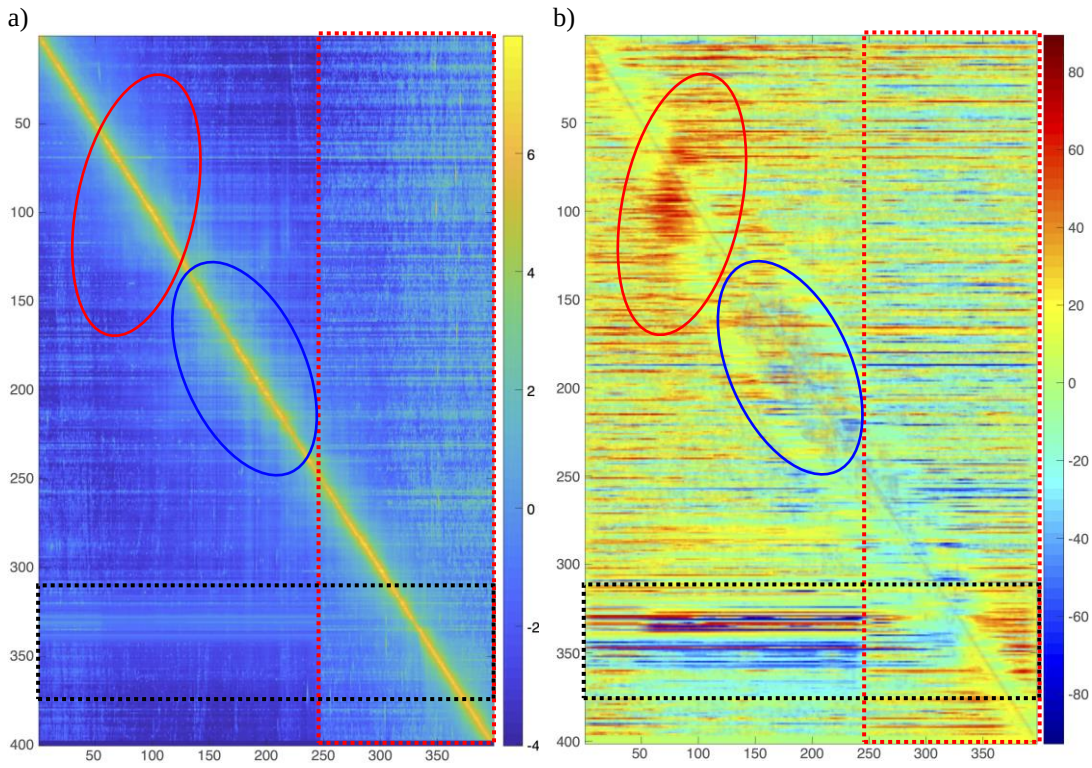

Figure 3-17 (a) energy attribute and (b) smoothed version of residual rotation angles. Y (time) and X (space) axes represent number of shots and the receivers respectively.

An energy attribute (maximum sum of squares of trace amplitudes) of the receivers for the horizontal components was calculated within a single non-variable window around the first breaks that were used to calculate the rotation angles is shown in Figure 3-17a. The red rectangle in Figure 3-17a shows a portion of the line with higher energy most probably an effect related to the near surface geology. The black rectangle shows relatively high levels of energy for the whole line, most probably a consequence of a

change in weather conditions during acquisition. The same features can be observed on a smoothed version of residual rotation angles (Figure 3-17b), However, additional features (blue and red ellipses) can be identified that do not occur in the energy attribute display. The length of the horizontally oriented smoothing operator was chosen carefully in order to remove the impact of random noise and preserve information related to subsurface geology.

Three attributes were derived from angle of rotation analysis:

- Residual rotation angle (red channel)
- Maximum energy of horizontal components (green channel)
- Source to receiver azimuth (blue channel)

These are shown in a colour composite attribute image (Figure 3-18). Despite some differences in each attribute pattern, their combination as a composite image clearly exhibits different subsurface-zones that can be analysed and correlated with the seismic section. It is also possible to perform characterisation along the line where the same colour describes a unique feature within the image. These features (zones) could be an indication of shear wave splitting directly affecting the rotation angles in the distinct zones. This can be tested and verified by testing the rock samples obtained from the outcrops.

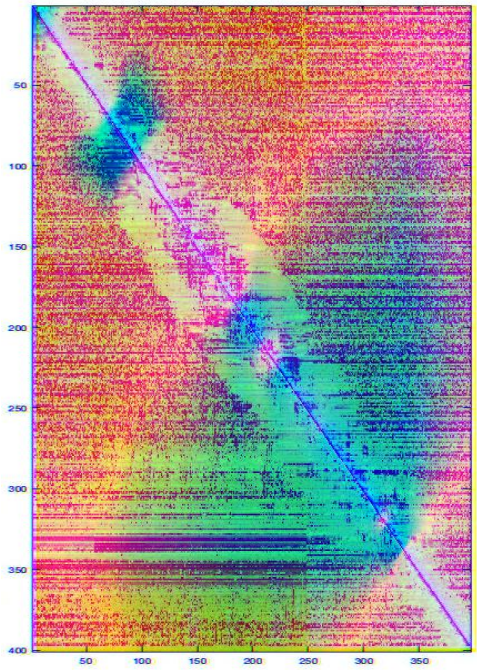

Figure 3-18 Colour composite plot of derived attributes: residual rotation angle (red), maximum energy of horizontal components (green), source to receiver azimuth (blue).

Figure 3-19 shows that subsurface geological structures can be correlated to the zones marked with red and blue ellipses in Figure 3-17 and Figure 3-19. The migrated stack (horizontal inline) is also included in the diagram to show that there is a correlation between the geology and the composite rotation attribute. These geological structures identified from the seismic data could cause the scattering features as well as the shear wave splitting giving rise to the zones identified from the residual rotation angles.

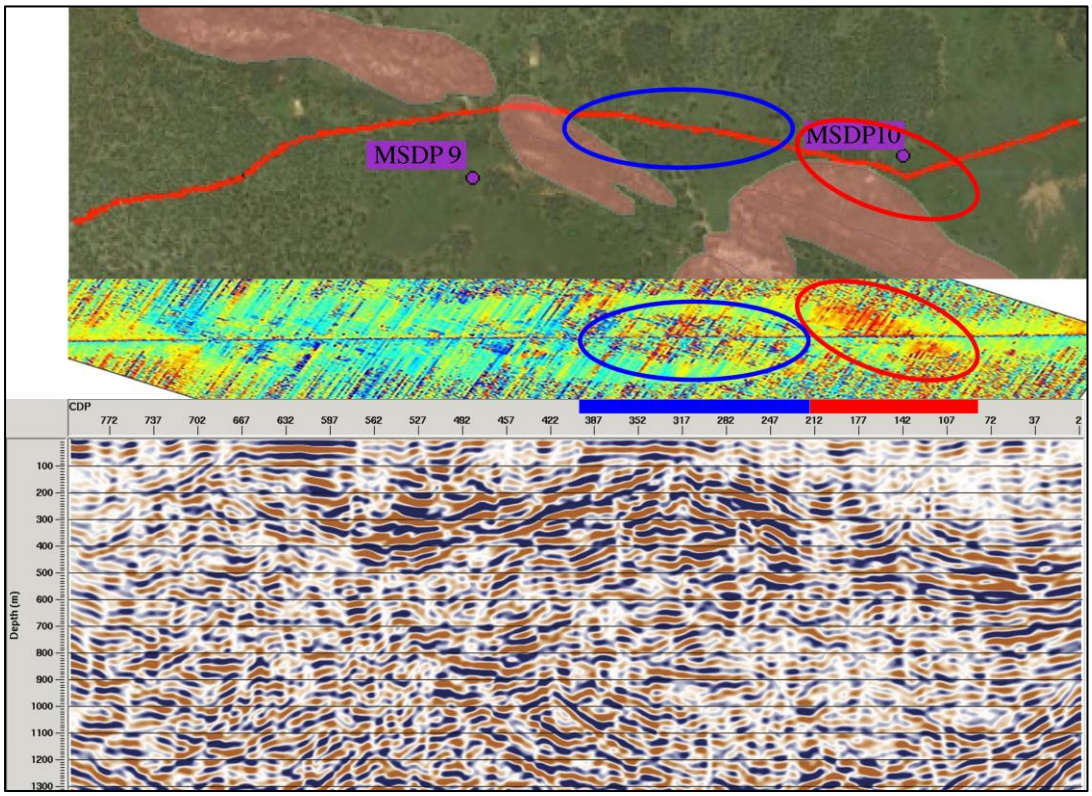

Figure 3-19 Migrated stack - horizontal inline component (bottom), residual rotation angle attribute (middle) and locations of outcrops (top). Blue and red lines above the seismic data, which coincide with marked zones in Figure 3-17b mark the surface locations where the rotation angle attribute and mapping confirmed the existence of outcrop.

3.3 Discussion

3.3.1 General Discussion about the Results

In order to translate seismic data into geological images, any available information such as VSP, Full Waveform Sonic logs (FWS), results of core sample analysis are needed. For this project, only a limited amount of information was available, comprising only density and mineralisation logs (Figure 3-21). Dr. Adrian Fabris of the Geological Survey of South Australia provided seven samples (mix of full and half

core) from borehole MSDP10. The results of analysis of these samples is provided in Table 3-4.

Table 3-4 Sample Information. Samples were provided by the Geological Survey of South Australia (Adrian Fabris). Radial direction results for each sample shown in blue.

Ref. Number	Depth (m)	V_P (m/s)	V_S (m/s)	$\frac{V_P}{V_S}$	$\rho \left(\frac{g}{cm^3}\right)$
2499659	81	5868	3493	1.68	2.64
		5902	3458	1.71	
2499660	300	5928	-	-	2.65
		5970	3640	1.64	
		6055	3569	1.7	
		5925	3576	1.66	
2499661	389	5945	3581	1.66	2.64
		5939	3652	1.63	
		5939	3631	1.64	
		5857	3663	1.6	
2499662	490	5794	3560	1.63	2.64
		5831	3642	1.6	
		5767	3569	1.62	
		6028	3545	1.7	
2499663	531	5546	3480	1.59	2.62
		5781	3641	1.59	
		5724	3584	1.6	
		5612	3486	1.61	
2499664	554	5688	3419	1.66	2.68
		5567	3260	1.71	
		5744	3374	1.7	
		5567	3363	1.66	
2499665	566	5626	3397	1.66	2.63
		5547	3477	1.6	
		5572	3385	1.65	
		5993	3733	1.61	

Figure 3-20 shows the V_P, V_S and the V_P /V_S ratio for the radial measurements of the samples. There are indications of anisotropy in particular for the deeper samples. For example, sample number 2499665 taken from a depth of 566 m, the maximum difference between the axial values for V_P is ~450m/s and for Vs is ~300 m/s. This is a good indicator of heterogeneity and hence anisotropy within the sample. Another feature to note from Table 3-4 is the difference between the radial and axial shear wave velocities This is an indicator of anisotropy giving rise to shear wave splitting within the samples for some depths. The Poisson ratio is included as part of Figure 3-20d. It is noticeable that the ratio starts to drop at around 490m with the lowest Poisson ratio of 0.17 occurring at 531m (sample 2499663).

a)

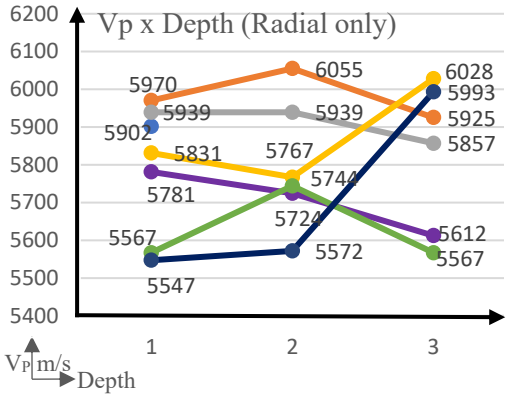

b)

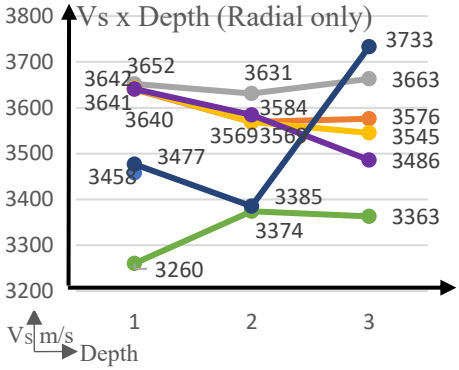

c)

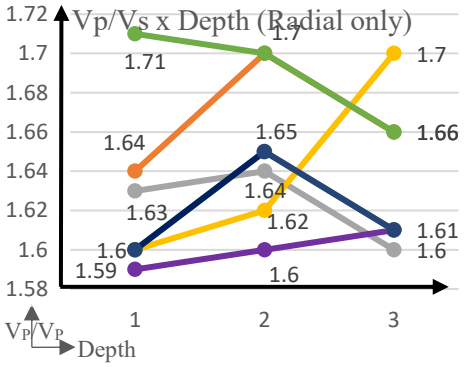

d)

Sample Ref. Number	Depth (m)	V_P/V_S (Axial values)	Poisson Ratio (Axial values)	
2499659	81	1.68	0.23	
2499660	300	-	-	
2499661	389	1.66	0.21	
2499662	490	1.63	0.20	
2499663	531	1.59	0.17	
2499664	554	1.66	0.21	
2499665	566	1.66	0.21	

Figure 3-20 Comparison of different radial acoustic measurements. a) V_P measurements b) V_S measurements, c) V_P/V_S ratio (radial values) d) V_P/V_S ratio (axial values) and Poisson Ratios (axial values). Different samples are shown in the colours defined in d). The differences observed in the radial values and axial values are a possible indicator of anisotropy which could have caused shear wave splitting and is an explanation for the zones observed in residual rotation angles (Figure 3-16c and Figure 3-19). Note the differences in measurements of V_P and V_S at the depth range 490-565 m.

It was reported by the Fabris et al. (2017) that the most significant mineralisation encountered in the area is found in borehole MSDP10. Elevated zinc (Zn) values and significant mineral rock alterations including frequent veining were detected between 490 m and 565 m. The laboratory measurements of V_P and V_S taken from 490 m to 565 m show that a drop in V_P and V_S occurs with depth for both the axial and radial measurements (Figure 3-21). The drop in Poisson ratio in the same depth range could be another indication of mineralisation. The drop in V_P and Poisson ratio is a powerful indicator of mineral alterations and should be further investigated and evaluated.

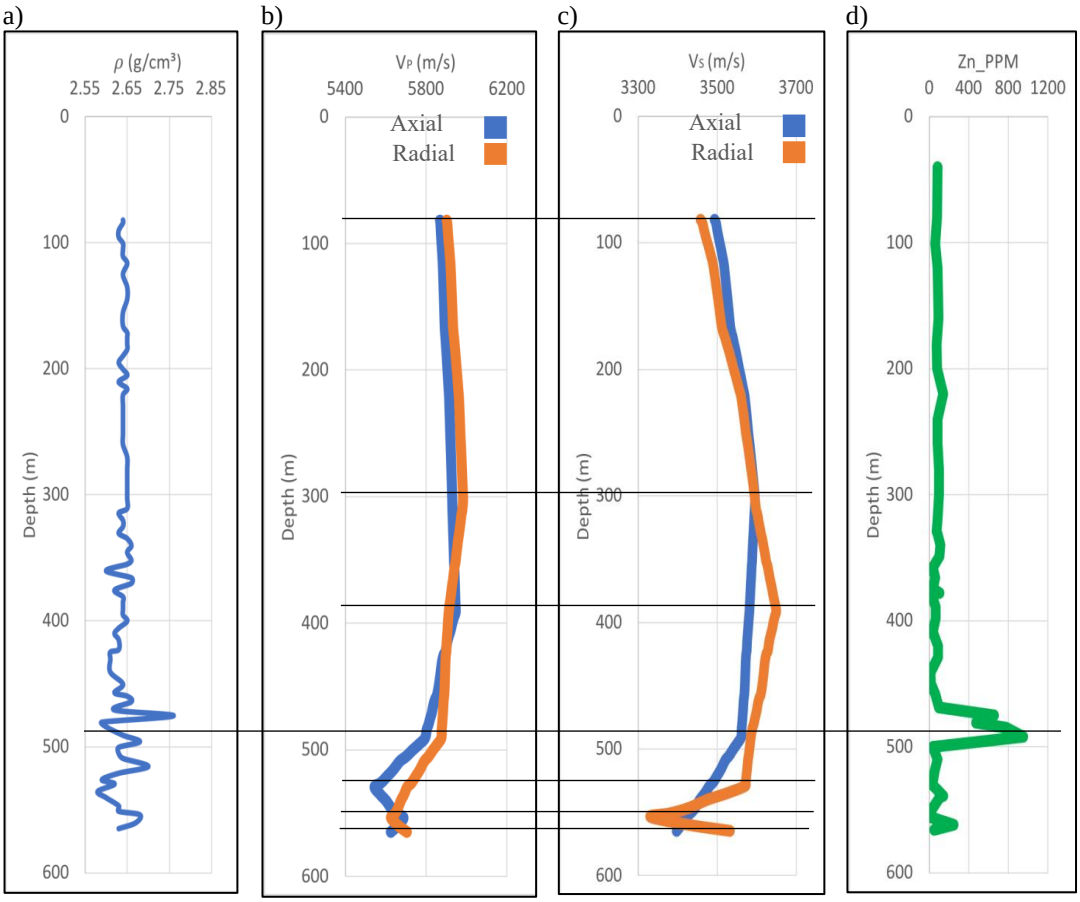

Figure 3-21 a) Density log from borehole MSDP10, b) V_P and c) V_S values (axial and radial) derived from the seven core samples (black lines show the depth of samples). Values in between interpolated in. d) mineralisation log for Zinc. Note that the drop in V_P and V_S values between 490 m and 565 m correlate with the elevated value of zinc measured in the borehole.

The reduction in velocity between 490m and 565 m can also be identified from the seismic data as a strong reflector. (Figure 3-22). As Fabris et al., (2017) also reported, this reflector is more evident in northern part of the seismic line nearest to the borehole. These results show that the acquisition of more seismic data is required to delineate the zone of high mineralisation potential. It is also clear that core sample measurements are important in understanding the seismic reflection pattern that could be related to mineral alteration zones in this area.

a)

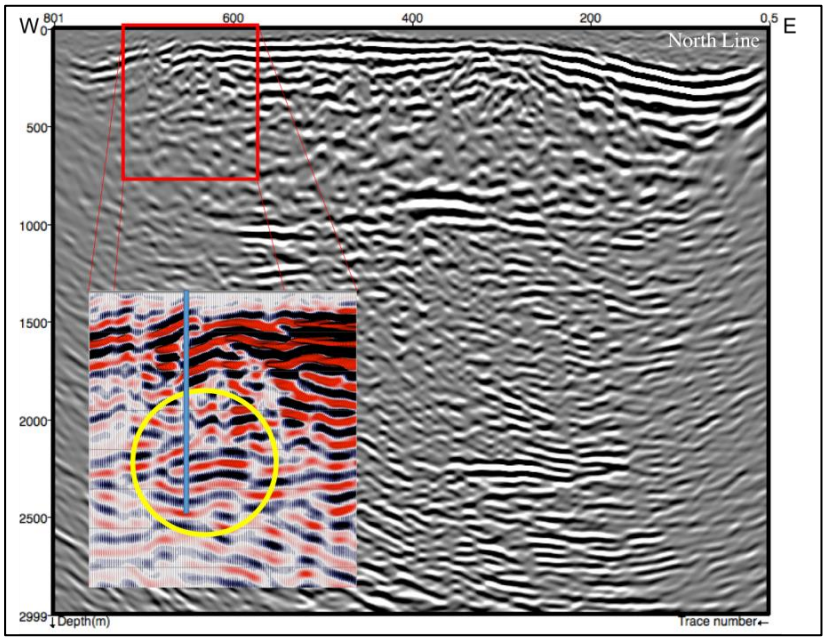

b)

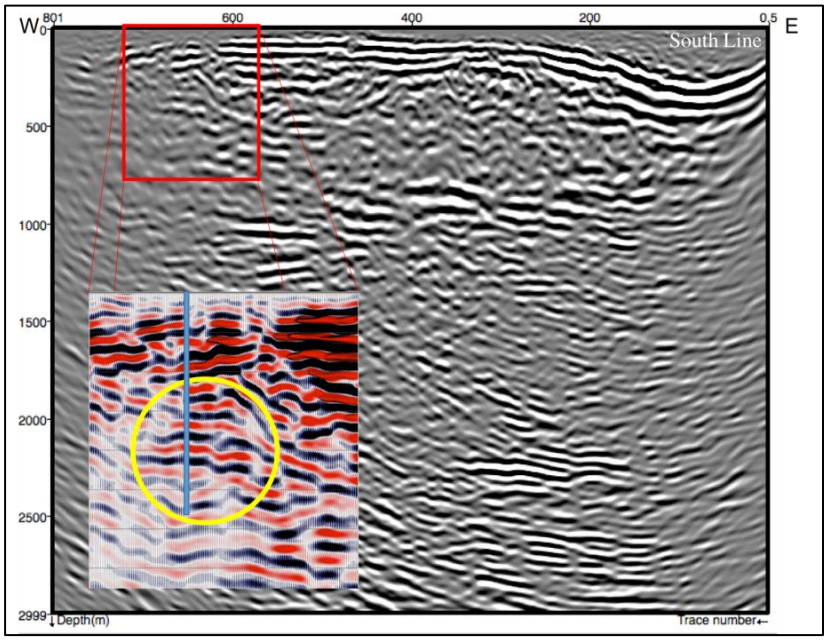

Figure 3-22 Comparison of migrated sections a) north and b) south lines. The red rectangle has been zoomed and displayed in colour to show which reflector is associated with mineralisation. The location of the borehole is also shown in the zoomed display

3.3.2 Sensitivity of Pre-processing in Hard Rock Environments

Effective three component processing is dependent upon achieving a good signal to noise ratio. Reducing noise is the biggest problem in hard rock seismic exploration. In the last decade, (in hard rock environments) thanks to technological advancements both in acquisition and computer power, the number of active channels has been increased resulting in a much larger number of traces contributing to CDPs (fold of

coverage). The main benefit of increased fold is a reduction in random noise when the data are stacked. 3C processing is dominantly focused on pre-stacked data. Therefore, great care must be taken when processing 3C data to avoid adversely affecting primary energy (signal) when attempting to attenuate random and coherent noise. Examples of coherent noise attenuation adversely affecting primary are shown in Figure 3-23 and Figure 3-24.

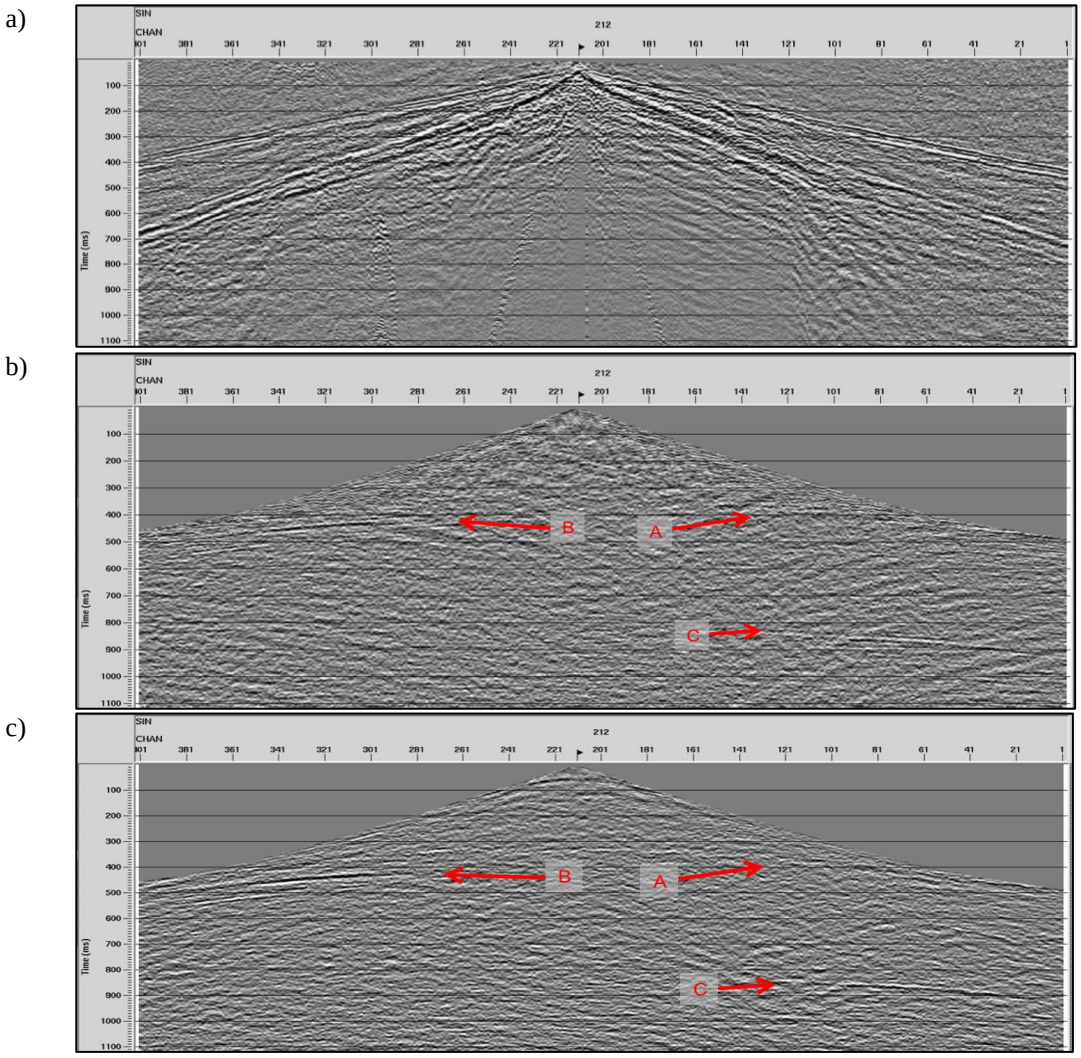

Figure 3-23 A typical hard rock shot gather. (a) raw, (b) after pre-processing adversely affecting primary energy (c) after optimal pre-processing using Stack-Unstack (SUS).

Figure 3-23 shows a typical hard rock shot gather a) before, b) after pre-processing (adversely affecting primary energy) and c) after optimal pre-processing including Stack-UnStack (SUS) resulting in the preservation of primary energy and a higher signal to noise ratio compared to b).

SUS (Dzunic et al., 2016) improves the SNR on a shot record by sorting the traces into the CDP domain, applying NMO and a simulation of Stacking-UnStacking procedure wherby a trace mix is used incorporating all the traces within a CDP to reduce noise (number of traces to mix is equall to the nominal CDP fold). The data are then sorted back to the shot domain with greatly improved SNR by nominal CDP fold. Such kind of shot is practically equivalent to portion of Stack where analysis of each pre-processing step will show impact on the signal. This step will allow greater control of subsequent processing to avoid adversely affecting primary energy. The SUS method was used to optimise the processing flow and produce the final images in this chapter (Figure 3-15 and Figure 3-22).

Examples of non optimal and optimal processing are shown in Figure 3-24 and Figure 3-25. Reflector A (Figure 3-25) is identifiable when SUS is added to the processing flow. However, reflector A is very poorly defined when a conventional processing sequence was used (Figure 3-24).

a)

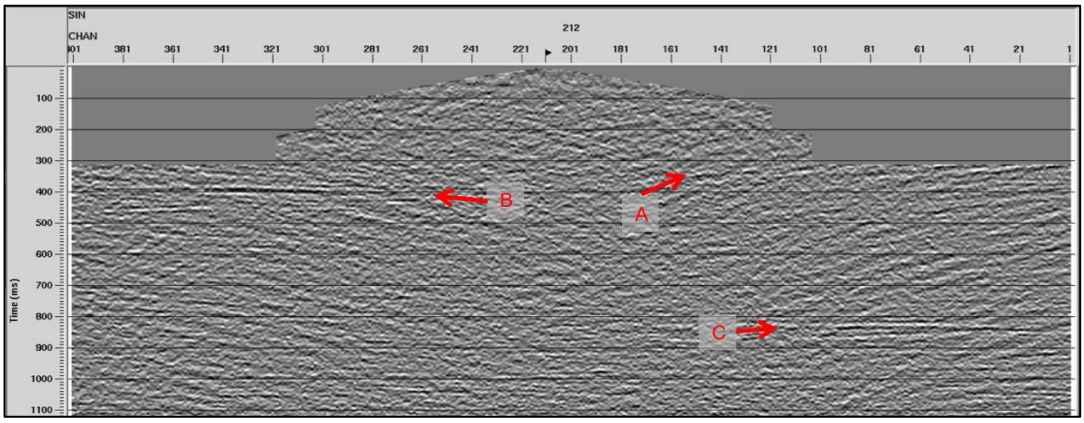

b)

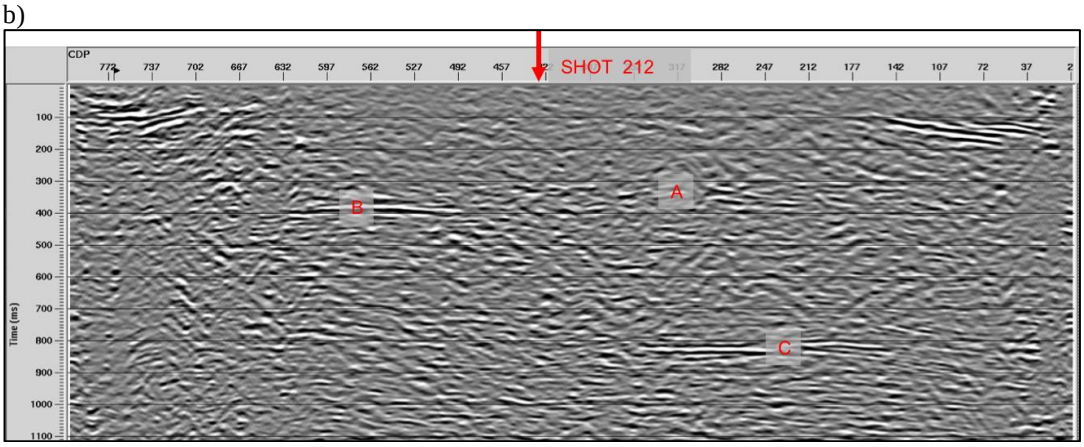

Figure 3-24 (a) NMO corrected SUS shot gather (non-optimal pre-processing), (b) final stacked section based on non-optimal pre-processing.

a)

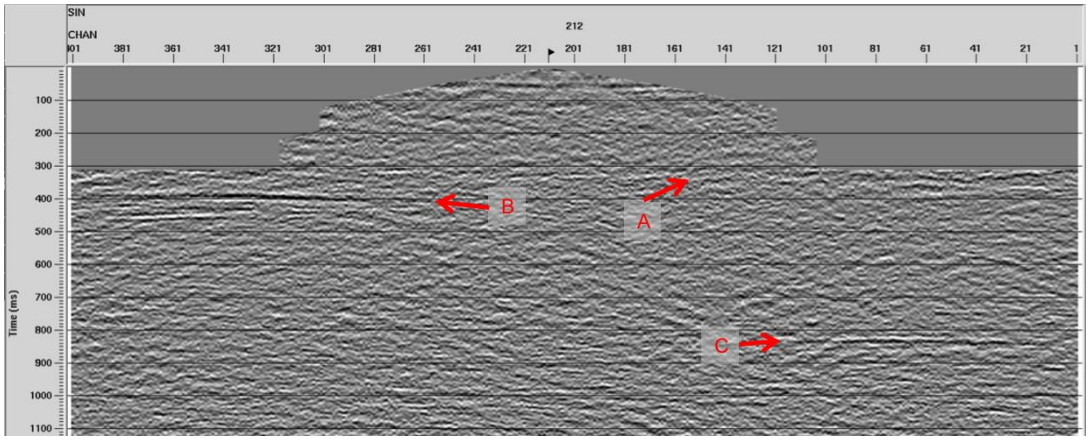

b)

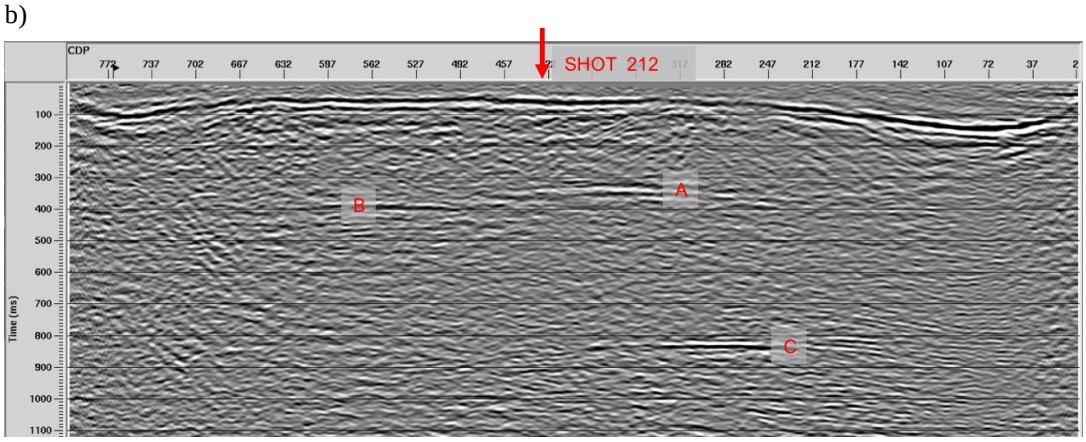

Figure 3-25 (a) NMO corrected SUS shot gather (optimal pre-processing), (b) final stacked section based on pre-processing sequence optimised by SUS.

In hard rock environments and on conventional shots, it is often very difficult to identify any reflectors that can be more easily identified in stacked section (or NMO corrected SUS shots). This being so, it is critical that a stacked result is checked when carrying out parameter testing for pre-processing.

Chapter 4 3D/3C Roy Hill Case Study

4.1 Synthetic Study

4.1.1 Introduction

The Roy Hill 3D/3C field data, recorded in the Pilbara, Western Australia (WA), were made available to study their potential for hard rock characterisation and mineral exploration.

A high-resolution 3C/3D survey focussed on a hard rock target had never been acquired prior to the Roy Hill survey. Only A 3C/3D semi-regional survey had been conducted in Canada (White et al., 2012). This being so, processing and analysis flows have never been standardised. Hence, the first step in this project was to design a processing flow to tackle the complexity of the survey. It was decided to test a full range of processing steps, ultimately to be tested on the field data, using a 3D synthetic model representative of the hard rock environment in the area of interest.

Processing was carried out using Landmark SeisSpace® seismic processing software.

4.1.2 High Resolution P and S Velocity Model Building

The most usual approach when constructing a 3D hard rock model is to create geological surfaces and structures. However, it was decided to employ a more time consuming and more seismic-like approach using the following steps:

1. Data were input from previous studies carried in the Kevista area including a vertical component 3D PSTM volume and a sparse 3D interval velocity field (derived from multiple iterations of migration velocity analysis).
2. Sparse spike acoustic impedance inversion was run to obtain coefficients of the reflections (Figure 4-1c). The low frequency component of the inversion was derived from the interval velocity field (Figure 4-1e). Densities and S-wave velocities were calculated using equations 4-1 and 4-2 (Mavko et al., 2009)).

$$\rho = 1843 + 0.137V_P, \tag{4-1}$$

$$V_S = 255 + 0.503V_P. \tag{4-2}$$

3. The Pseudo Acoustic Impedance (PAI) was then calculated (Figure 4-1d) using the Sparse spike section. The interval velocities were smoothed (Figure 4-1e)

and used with the migrated seismic volume (Figure 4-1a) to obtain a sparse reflectivity volume (Figure 4-1c) and instantaneous amplitudes (Figure 4-1b) using a Hilbert transform.

The most significant amplitudes were then detected by automatically searching for local maxima. The sign was determined from the polarity of the real part of the complex trace.

Using the reflectivity section, velocities and densities, the PAI was calculated using a recursive formula (4-5) which was derived as follows:

$$R_{(n+1,n)} = \frac{Z_{n+1} - Z_n}{Z_{n+1} + Z_n}, \tag{4-3}$$

where $R_{(n+1,n)}$ is the reflection coefficient and Z_n and Z_{n+1} are the acoustic impedances of two neighbouring layers calculated from a product of the velocity and density of each layer equation (4-4).

$$Z_n = \rho_n V_n. \tag{4-4}$$

For Z_{n+1}:

$$Z_{n+1} = Z_n \frac{1 + R_{(n+1,n)}}{1 - R_{(n+1,n)}}. \tag{4-5}$$

In order to perform this recursive calculation, it was necessary to provide an initial acoustic impedance value. The P velocity model is taken from PSTM processing while the density was calculated using equation 4-1.

4. The PAI volume which contains both the high and low frequency components was smoothed and was then used in conjunction with the interval velocity volume (equation 4-6) to obtain a high-resolution velocity model.

$$V_n = \frac{Z_n}{\rho_n}. \tag{4-6}$$

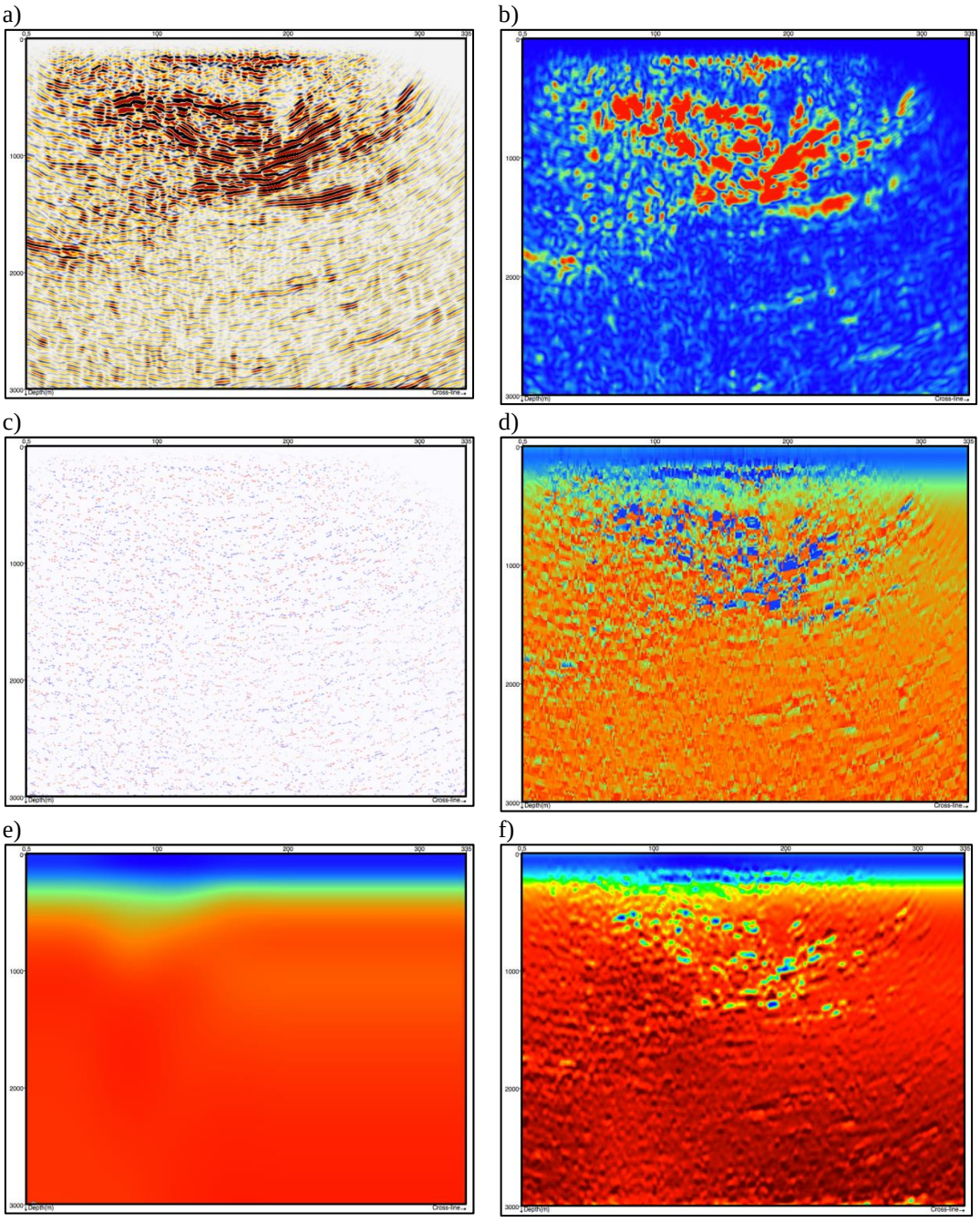

Figure 4-1 Velocity model building procedure based on Pseudo Acoustic Impedance (PAI). Example for inline 100: a) PSTM seismic section from previous studies, b) Calculated Instantaneous attribute (envelope) section, c) Sparse spike section produced from instantaneous attribute section, d) Calculated PAI, using sparse spike section and interval velocity model, e) Smoothed interval velocity model derived from PSTM data d) and Velocity model (V_P) used for modelling. f) Final high-resolution interval velocity model in depth.

The high resolution (P) interval velocity volume used for forward modelling is shown in Figure 4-2a. The RMS velocity volume used as a stacking velocity is shown in Figure 4-2b.

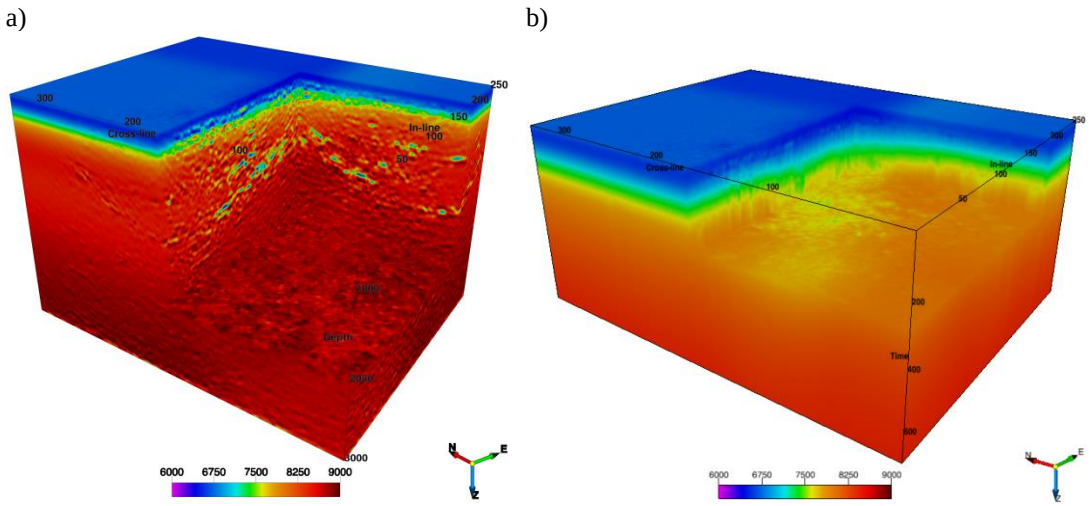

Figure 4-2 a) High resolution P interval velocity volume in depth and b) P RMS velocity volume in time.

4.1.3 3D/3C Elastic Finite Difference (FD) Modelling

Numerical experiments were carried out using a 3D elastic time-domain finite-difference parallel solver (SOFI3D) (Bohlen, 2002). The computation was carried out on a cluster system. The code utilised for the modelling solves the elastic wave equation by discretising the velocity-stress formulation on a standard staggered grid (Virieux, 1986; Levander, 1988). The staggered-grid coordinate utilised is shown in Figure 4-3.

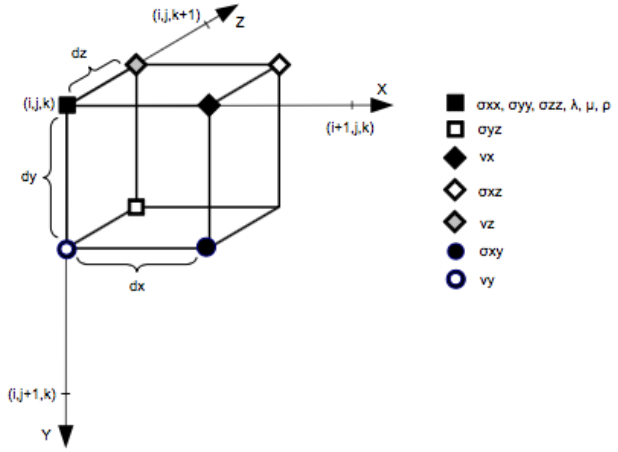

Figure 4-3 Staggered-grid coordinate used by SOFI3D (Bohlen et al., 2015).

When a force f is applied (set in motion) the wave propagation can be written as first order differential equations:

$$\rho \frac{\partial v_i}{\partial t} = f_i + \frac{\partial \tau_{ij}}{\partial x_j},$$
$$\frac{\partial \tau_{ij}}{\partial t} - \lambda \frac{\partial \Theta}{\partial t} \delta_{ij} + 2\mu \frac{\partial \varepsilon_{ij}}{\partial t} = 0, \quad (4\text{-}7)$$
$$\frac{\partial \varepsilon_{ij}}{\partial t} = \frac{1}{2}\left(\frac{\partial v_i}{\partial x_j} + \frac{\partial v_j}{\partial x_i}\right),$$

where ρ is density, λ and μ are lamè parameters, Θ is the trace of the stress tensor, τ_{ij} is an element of stress tensor and ε_{ij} is an element of strain tensor. The formulation uses the particle velocity ($v = \frac{\partial u}{\partial t}$) as the wave parameter. Since only first order derivatives are used this solution is faster and more stable than standard 2nd order formulations traditionally used (Kelly et al., 1976).

To solve equations 4-7, off-diagonal stress components and velocities are calculated on a half grid shifted to the original system while diagonal stress components (σ_{ii}) and model parameters (λ, μ and ρ) are localised on full grid points. The code uses staggered grids to reduce the computation time and increase the precision of the solution (Bohlen et al., 2015).

To solve the series of differential equations (equations 4-7), two recursive steps were performed. The first step used spatial stress derivatives and the velocity updates were calculated. The second step used spatial velocity derivatives and the Generalised Hooke's Law to calculate the stress value updates. The sum of all the updated values for all time steps provide an approximate solution to velocity-stress formulation. The unwanted reflections from the model boundaries were damped over 30 grid points by multiplying the amplitudes using a slowly decaying exponential factor (Bohlen et al., 2015)).

The code utilised is efficient, fast and accurate in modelling the wave propagation in a complex media allowing production of 3D models. Prior to the final code execution to create a model with 3960 input shots, a comprehensive test stability test was conducted and the 3D shot-receiver geometry checked and verified.

The "acquisition geometry" used for the numerical modelling experiment is shown in Table 4-1.

Table 4-1 Acquisition parameters used in modelling

Main data acquisition parameters	
Geometry	3D
Sample rate	1 ms
Recording length	2 s
Receiver type	3C
Receiver spacing	15 m
Shot point spacing	15 m
Source type	Vertical force source
Shots	3960
Number of shot lines	12
Shot line spacing	300 m
Active Channels	4144
Number of receiver lines	16
Receiver line spacing	150 m

4.1.4 3D/3C Data Processing

SeisSpace® (a software package provided by Haliburton) was used to process the 3D data. The first quality control (QC) step was to generate a fold of coverage map (Figure 4-4). This showed that the maximum fold was 200.

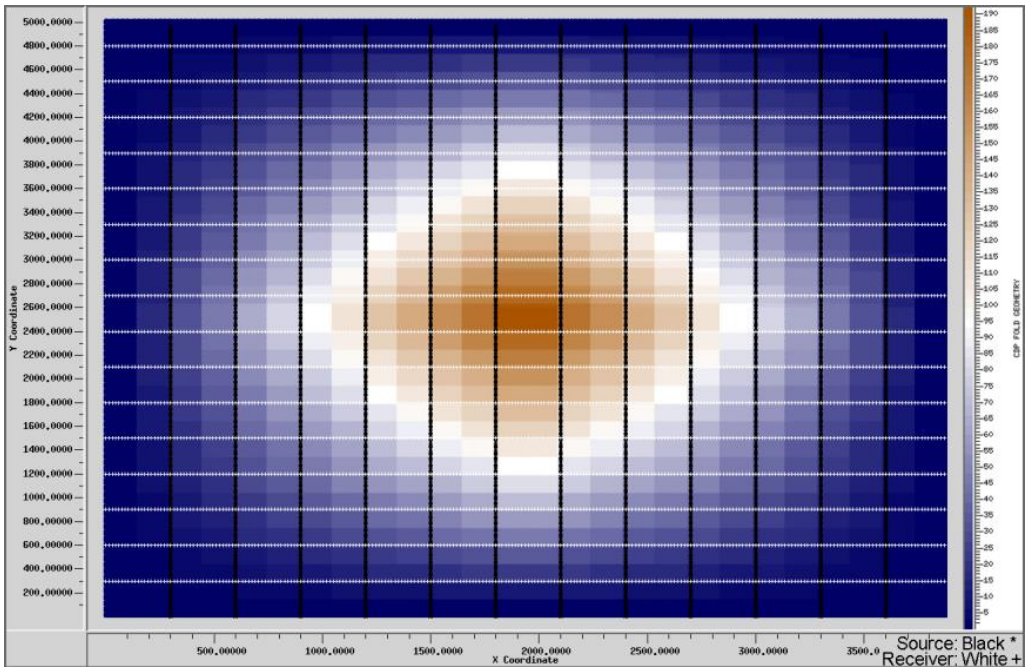

Figure 4-4 Fold of coverage overlain on acquisition geometry. Horizontal white and + are the receiver stations. Vertical black and * are the source stations.

An example of a 3D/3C shot record from a single source with 16 receiver lines is shown in Figure 4-5 for the vertical (Z), horizontal inline (X), and horizontal crossline (Y) components.

a)

b)

c)

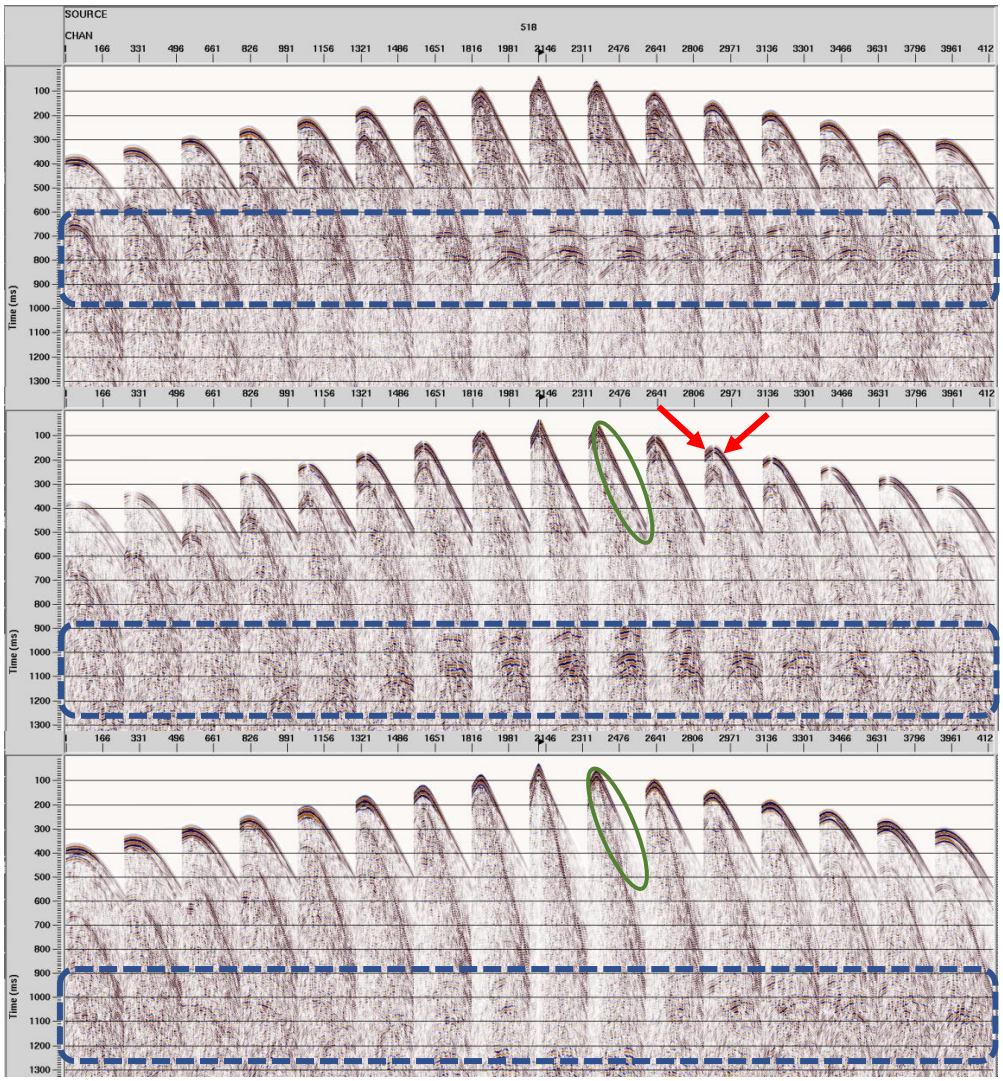

Figure 4-5 An example from a shot record with 16 receiver lines from the 3D/3C modelled data, a) Z, b) X and c) Y components. The main events occur in the hlighlighted blue boxes. Note that these events occur later in the horizontal components (X and Y) as Vs is lower than Vp. The P-wave first arival is recorded for both horizontal components as it is high energy, but it is usually more pronounced for the X compared to the Y. This is the case for the exampe above (green ellipsoid). A polarity reversal is identifiable for the X data either side of the shot location as shown by red arrows.

The vertical component of the modelled data (Z) was processed using the steps shown in Table 4-2. The processing flow for both horizontal components is also shown in Table 4-2

Table 4-2 Vertical and horizontal components processing flows.

	Vertical Processing
1	SEGY files Input
2	Data select and Shot QC
3	3D Geometry
4	Pre-processing
5	Velocity Transfer
6	Stack

	Horizontal Processing
1	SEGY files Input
2	Data select and Shot QC
3	3D Geometry
4	Fixing the polarity
5	Pre-processing
6	Initial estimation of PS RMS velocity
7	PS binning (ACP/CCP)
8	ACP/CCP-Stack

Figure 4-6 shows an example shot gather a) before and b) after vertical pre-processing. High frequency surface waves are identifiable on all shots (highlighted by red arrows) before pre-processing. These events masked underlying primary energy in some areas as shown inside the blue dashed rectangle. The surface waves were successfully removed by targeting their relatively slow velocity using a trace mixing approach. Spiking deconvolution was then run using a 60 ms operator and 0.1 percent pre-whitening and a 1000 ms design window (between 5 Hz and 120 Hz) to attenuate multiples and relatively low frequency remnant surface waves. Deconvolution was followed by the application of a band pass (BP) filter 6-14-70-120 Hz. Further pre-processing was not required as the modelled data were free of ambient noise.

Figure 4-7 shows a gather from the same shot as the one in Figure 4-6. However, a) before and b) are after X component pre-processing.

a)

b)

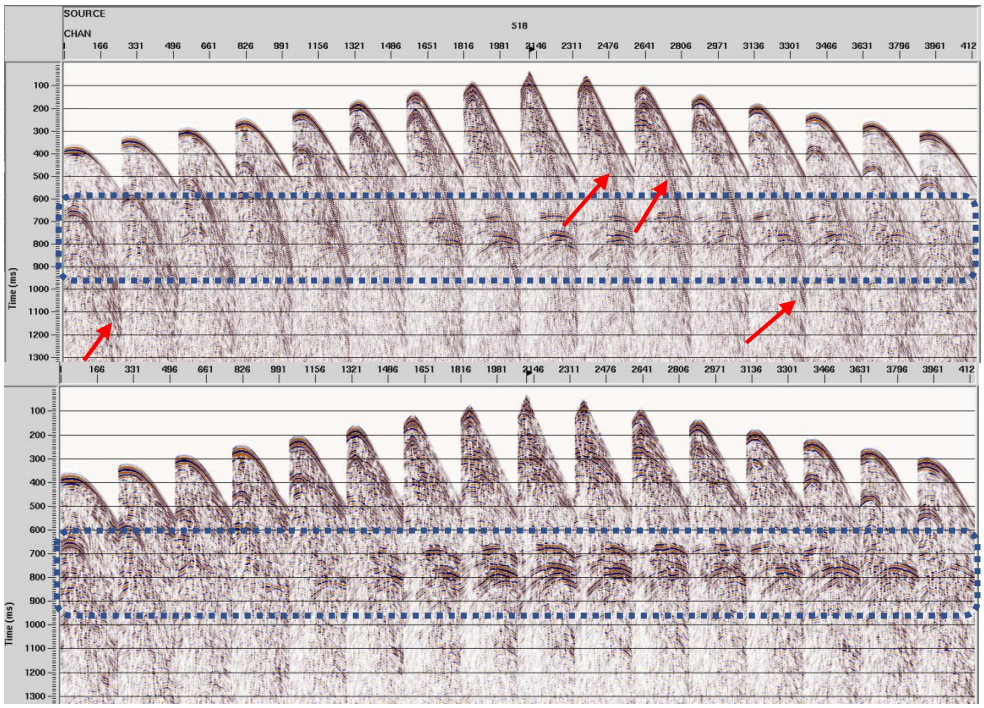

Figure 4-6 Example Z component shot gather a) before and b) after pre-processing. A package of high frequency surface waves is visible (highlighted by red arrows). Note that the reflection package (denoted by blue dashed rectangle) is enhanced after pre-processing.

a)

b)

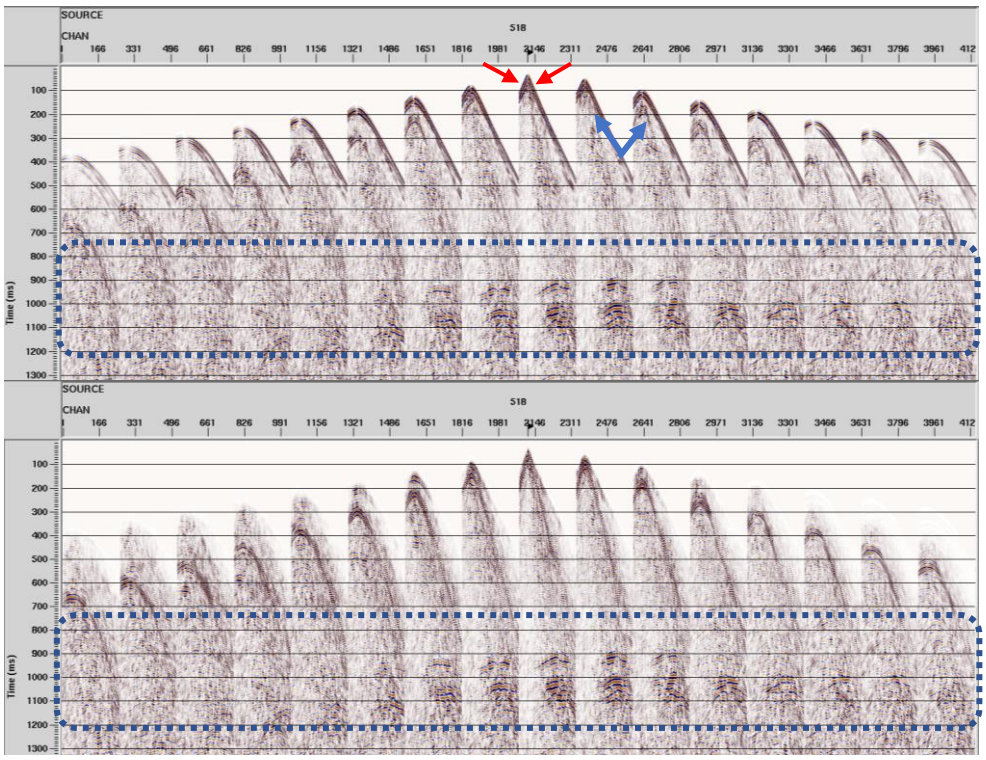

Figure 4-7 Example X component shot gather (for the same shot as Figure 4-6). a) before and b) after pre-processing. Polarity reversal near the shot position is identifiable (example shown by red arrows). Some residual of P energy is also highlighted by blue arrows on the raw shot. Note that the reflection package (denoted by blue dashed rectangle) is enhanced after the pre-processing.

Chair displays of the 3D stack amplitude volumes for the Z, X and Y components are shown in Figure 4-8, Figure 4-9 and Figure 4-10 respectively.

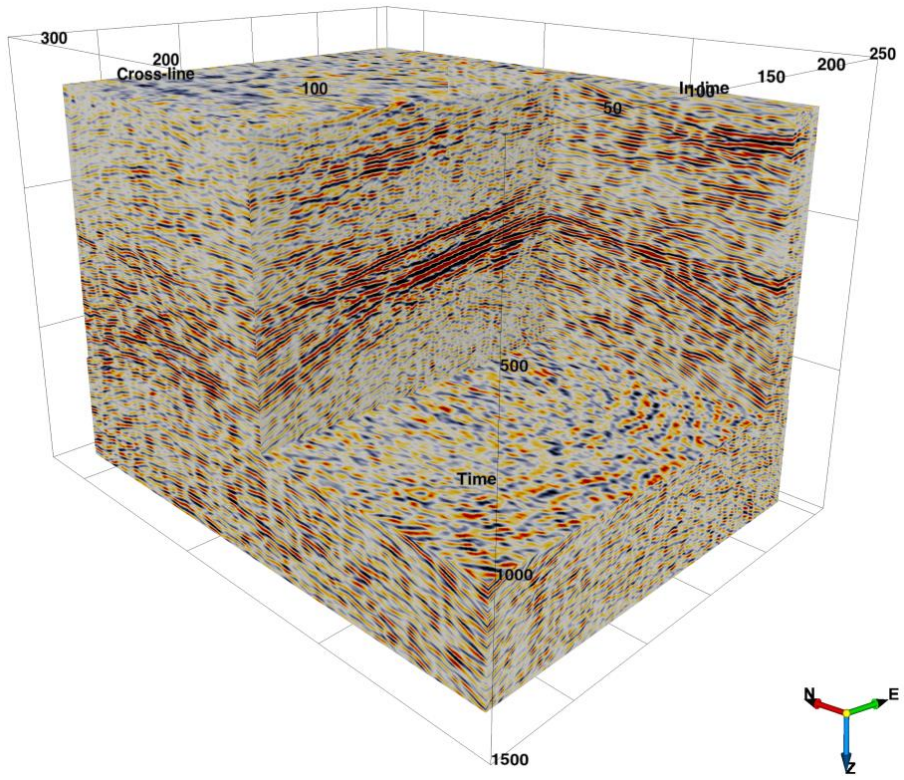

Figure 4-8 Chair display of 3D stack amplitude volume for vertical component (Z) in time.

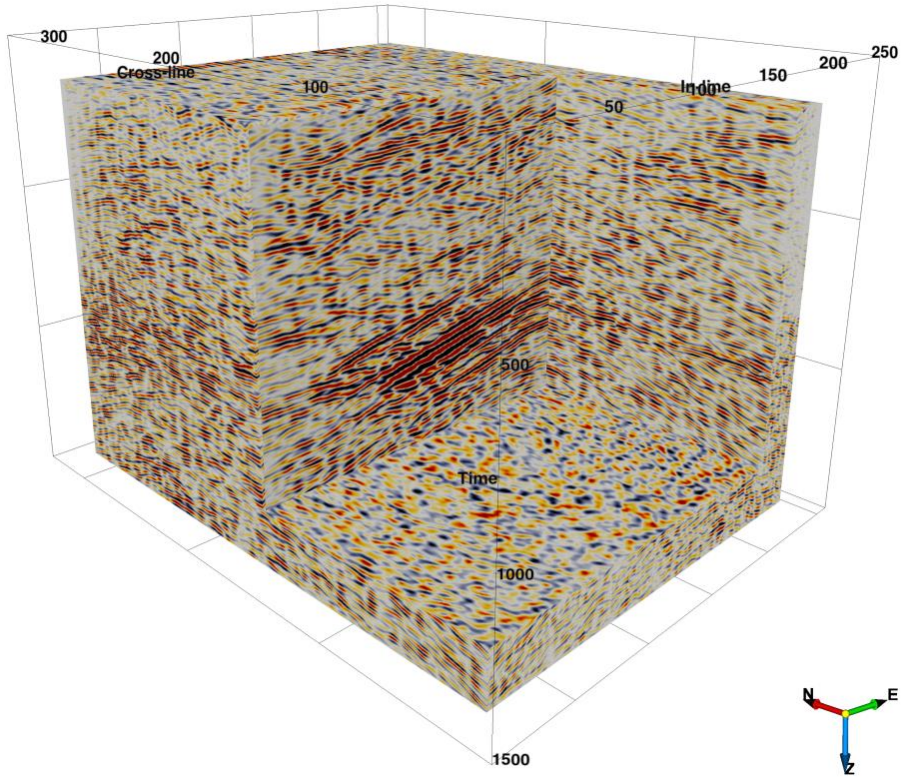

Figure 4-9 Chair display of 3D stack amplitude volume for horizontal X component in time.

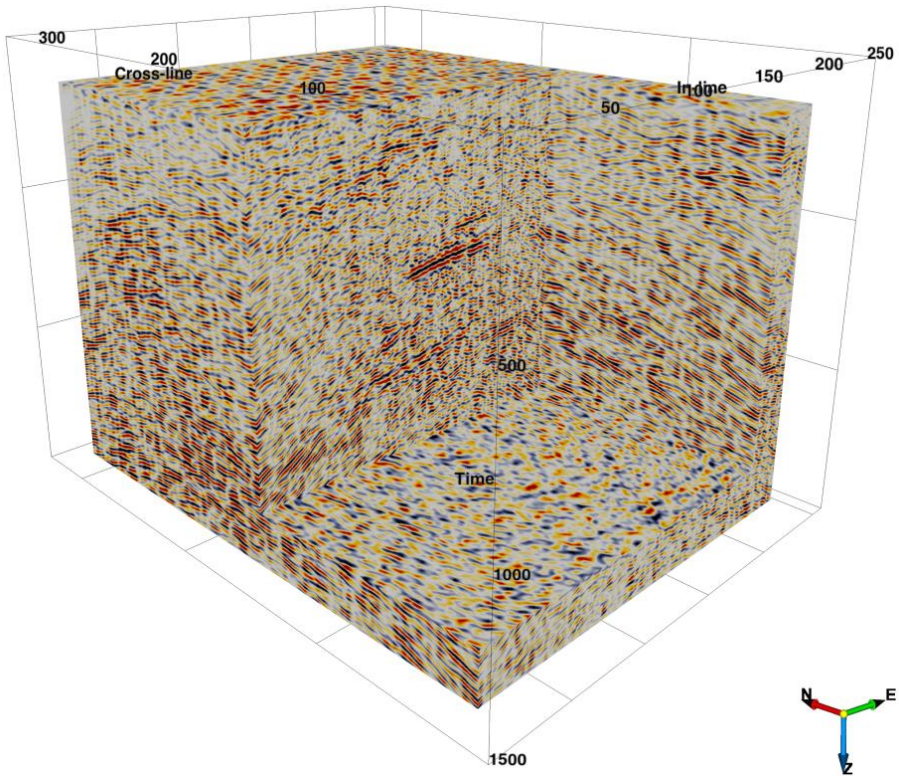

Figure 4-10 Chair display of 3D stack amplitude volume for horizontal Y component in time.

The concept of creating a geological model (high resolution velocity model) based on PAI inversion produced encouraging results showing a close resemblance to field data. Optimising the processing flow using modelled data proved to be an important learning step and helped reduce the time to process the field data.

4.2 Field Data, 3D/3C Seismic Processing of Roy Hill Project

4.2.1 3D Seismic Survey over Iron Ore Deposits

The Roy Hill iron ore deposit is located on the northern side of the Fortescue Valley in the Pilbara, Western Australia. The mineralised sections typically exhibit low densities and low seismic velocities due to vugose porosity (dry with mega-size pores that are often connected). Such a system produces significant scattering of seismic energy. In a search for the best methodology to explore these vast iron ore reserves several seismic trials were conducted between 2006 and 2017.

For this study the data from a 3D/3C survey shot in 2016 have been utilised. The acquisition parameters are given in Table 4-3.

Table 4-3 3D-3C data Acquisition parameters for Roy Hill project.

Main data acquisition parameters	
Date	2016
Geometry	3D
Sample rate	1 ms
Recording length	3 s
Geophones	3C
Receiver spacing	3 m
Receiver lines	7 Lines
Shot spacing	3 m
Shot lines	Unconventional
Source	45k Weight drop
Number of shots	1110
Number of live channels	678
CDP Binning	3m x 3m
Inline	74
Crossline	106
Data format	SEGD

The Sercel Unite wireless recording system with 3C geophones were used for the survey. The survey layout is shown in Figure 4-11. The number of shots was limited to 1110 in a highly irregular pattern due to access restrictions.

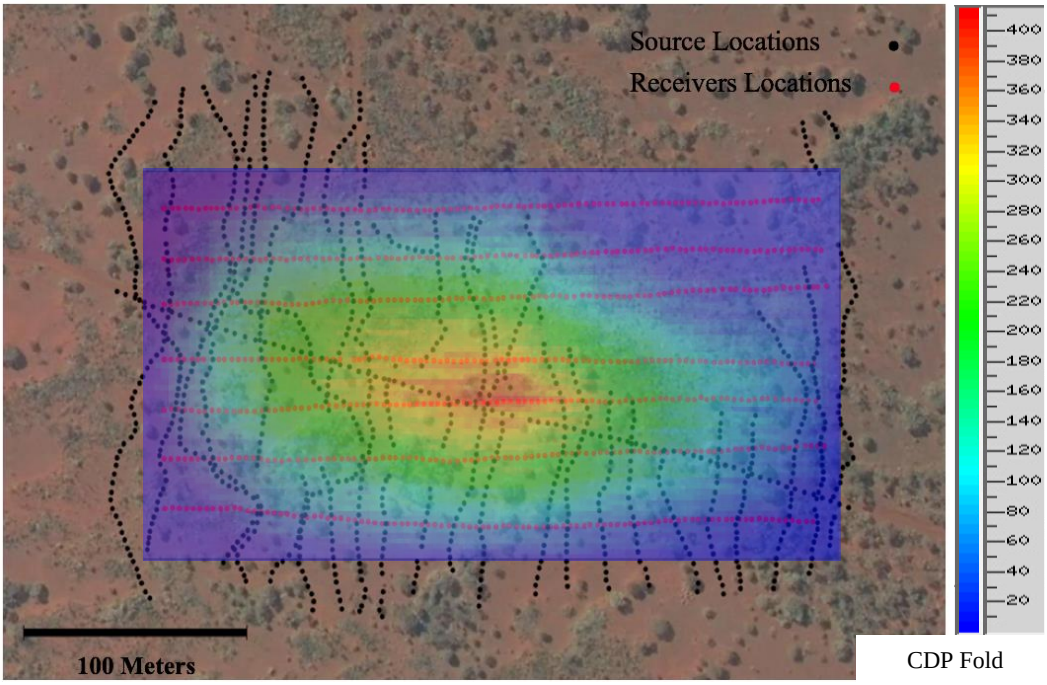

Figure 4-11 Roy Hill 3D survey: red dots are receiver locations and black dots are shot locations. Significant acquisition foot print may be anticipated as a result of the restricted shooting pattern. The irregular shooting will also give to a highly irregular fold of coverage, none-uniform azimuthal distributions and variable signal to noise ratio (SNR) throughout the survey area.

An example shot gather for a single receiver line (vertical (Z) component) is shown in Figure 4-12. In Figure 4-13, the horizontal components are shown for the equivalent shot gather. Reflectors of interest are indicated by arrows. It is interesting to note that after noise attenuation, the SNR for the horizontal components matched or exceeded that of the vertical component data.

4.2.2 Data Processing

The field data were reformatted using the SeisSpace® software package and output in internal format. After assigning the geometry to each trace, the three components were separated. Most effort after this was devoted to SNR improvement. The input data quality was poor with significant contamination by high amplitude coherent noise.

The three components shared the same geometry and similar processing steps. However, some differences in the processing sequence were needed for the horizontal components due to the presence of mix-modes (PS) and different S-wave polarisation directions.

The S-wave velocity is usually around half of (or less) the P-wave velocity. This being so, travel time delays in the near surface weathered layer are much greater for the shear modes (not converted one way or both ways) through the near surface (regolith) when compared to P-wave travel time delays. Hence, S-wave statics are very large compared to P-wave statics. To determine S-wave statics it requires picking and analysis of the shear head waves. Shear head waves are notoriously difficult to pick as they occur as secondary events not the first breaks as is the case for P-head waves.

As a result of the low and irregular fold for this survey, every effort was made to retain as many traces as possible for stacking. Hence QC for editing purposes was only conducted after application of deconvolution and filtering. This being so, strong, narrow frequency band noise caused by nearby machinery such as moving vehicles, generators, working machinery and drilling rigs was particularly important to attenuate.

The processing flow used for horizontal Components is shown in Table 4-4 An example of a single receiver line before and after application of P-wave pre-processing is shown in Figure 4-12.

Table 4-4 3D-3C data horizontal processing flow for Roy Hill project.

Horizontal Components Schematic Processing Flow
1. Segy_in
2. Geometry
3. Receiver orientation and rotation
4. Pre-processing
5. Construct PS velocity from P velocity
6. CCP Binning
7. NMO
8. STACK 3D
9. PS to P Time transfer
10. Migration

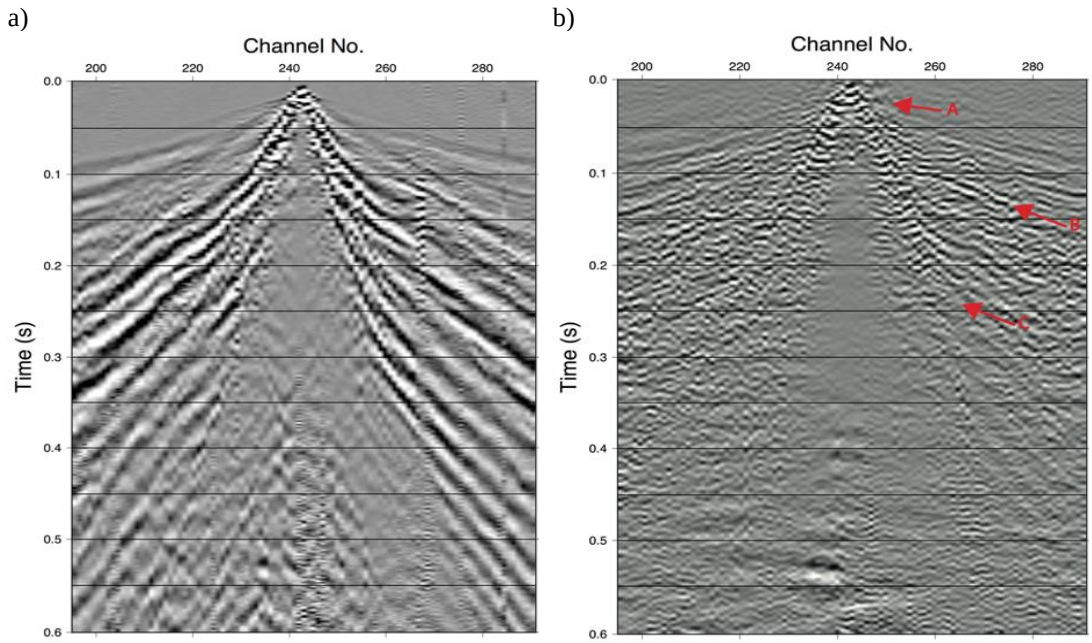

Figure 4-12 A shot gather (single receiver line): (a) Raw vertical component and (b) Pre-processed vertical component. Arrows (A, B, and C) shows reflectors of interest to this study.

4.2.3 Horizontal Components - Processing Flow

Receiver orientation and rotation is one of the first steps in addition to conventional P-wave processing for converted wave processing. Trace headers (populated as part of the geometry assignment process) containing the source–receiver azimuth and inclination were used to rotate the horizontal components in a way that one component (radial) pointed towards the source and the other component (transverse) was perpendicular to that direction. As the radial component is aligned with the source, the polarity issue will be automatically fixed using rotation and orientation.

The next step was to compute travel time delays through the regolith. For the PS mode (downgoing P-mode and upgoing S-mode), the source statics were assumed to be the same as for the vertical component that is P-wave down, while the receiver statics were calculated from the vertical component values using an assumption of $V_P/V_S = 1.6$, the case for SV wave up through the regolith to the receiver.

All shot gathers were checked for various types of coherent noise. Initially, low velocity surface waves characterised by relatively high amplitudes in the low to mid frequency ranges were attenuated by employing median mix-subtraction in F-K space. After suppressing surface waves, spectral whitening, air wave attenuation and band

pass filtering (5-15-90-120 Hz) were applied. No further pre-processing was run. An example of shot records for a single receiver line before and after pre-processing is shown in Figure 4-13.

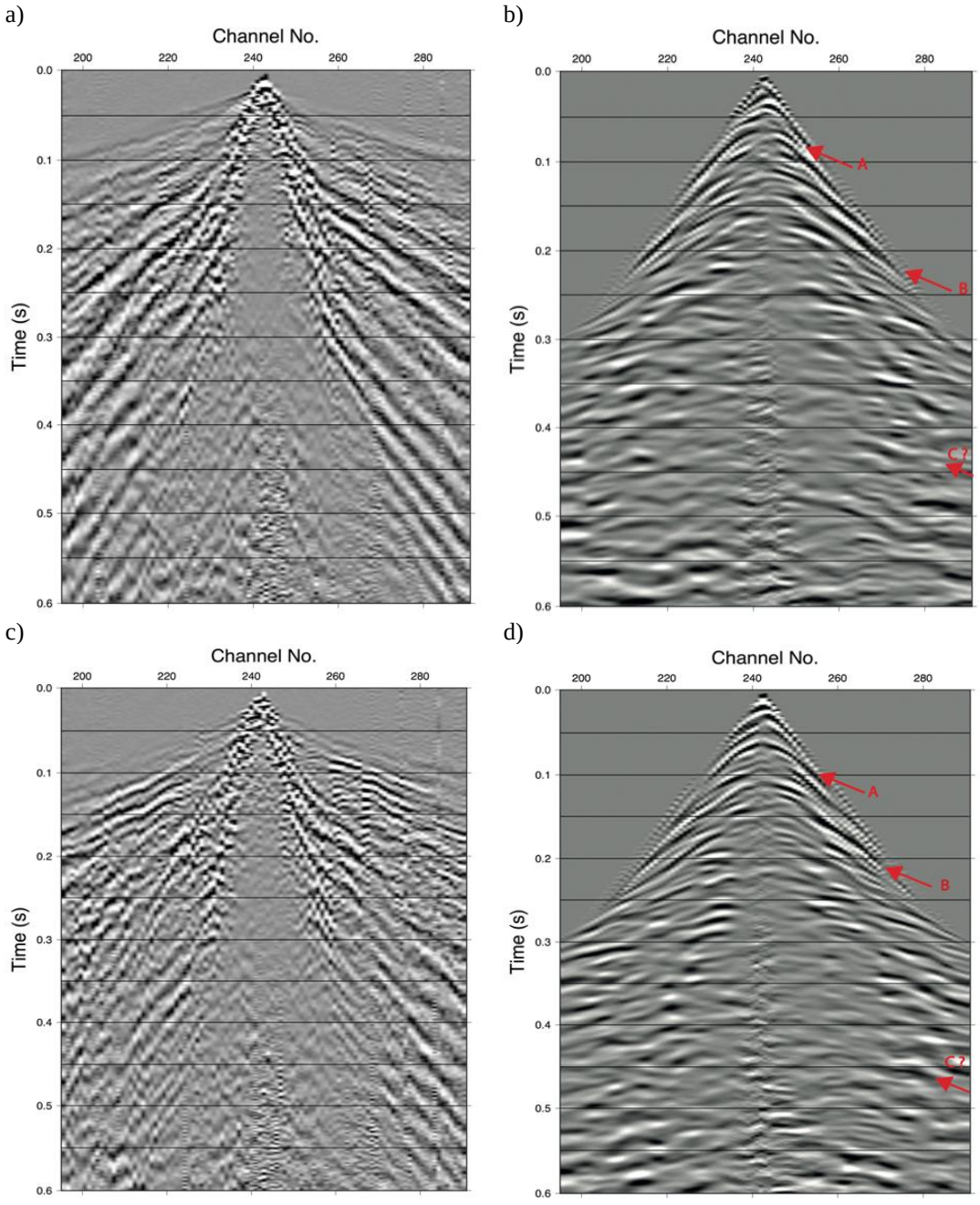

Figure 4-13 Example shot gather (single receiver line) for horizontal components: (a) raw, (b) pre-processed inline (X component), (c) raw and (d) pre-processed crossline (Y component). Red arrows denote reflectors of interest.

It has already been discussed above, that PS converted waves do not conform to the Common Mid-Point (CMP) method used for the processing of P-wave data. Instead of

CMP binning, a CCP binning process was used (assuming there is a change of mode between the down going and up going wavefields). A schematic definition of CCP and its relation to CMP is shown in Figure 4-14. Bin numbers and coordinates were copied to the trace headers (replacing the CDP numbers and coordinates used for P-wave processing).

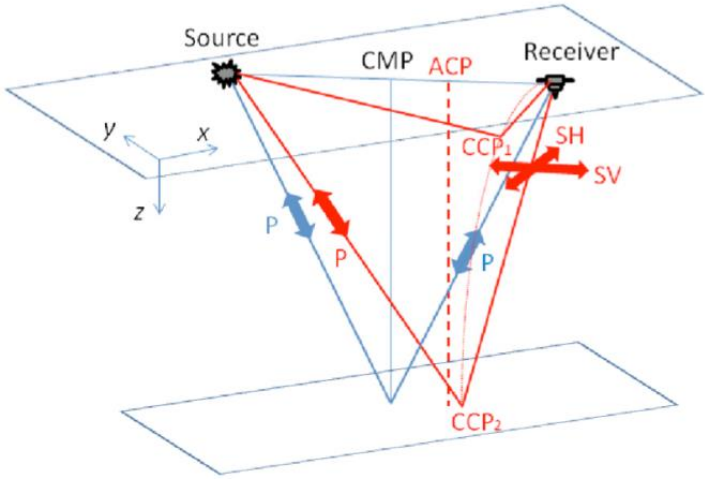

Figure 4-14 Ray diagram for P-SV wave conversion. The red line represents a PS-wave reflection, and the blue line a P-wave reflection. Arrows show the directions of particle motion. The CCP is offset from the CMP towards the receiver, and the dotted line represents a continuum of CCPs in depth. The dashed line indicates the Asymptotic Conversion Point (ACP) that can be used to approximate the CCP (after SeisSpace® documentation).

After CCP binning, interactive velocity analysis was carried out on supergathers (every 25th CDP) using a guide function which was calculated using the P-wave velocities and the constant V_P/V_S ratio.

A 3D volume for each component was created using the flow shown in Table 4-4. For the shear components a 500ms window AGC was applied pre-stack to increase the SNR. Post stack, to further enhance the SNR, F-XY deconvolution (multidirectional) was applied across a frequency range of 5-120 Hz. A very mild 2D spatial filter was then applied to reduce random noise and/or strong noise bursts in the data using an alfa-trim mode with a 3-trace by 3-sample operator. An example of a converted wave stack for in-line 25 (before and after conversion to P-time) is shown in Figure 4-15. Transformation into P-time domain utilised the constant V_P/V_S ratio (Figure 4-15b). Conversion to P-time is needed for direct comparison with the P-wave stack to better evaluate the quality of the results achieved with converted wave processing. When the

data were compared, several patchy reflectors were identified. It was decided that further analysis would be required to improve these events.

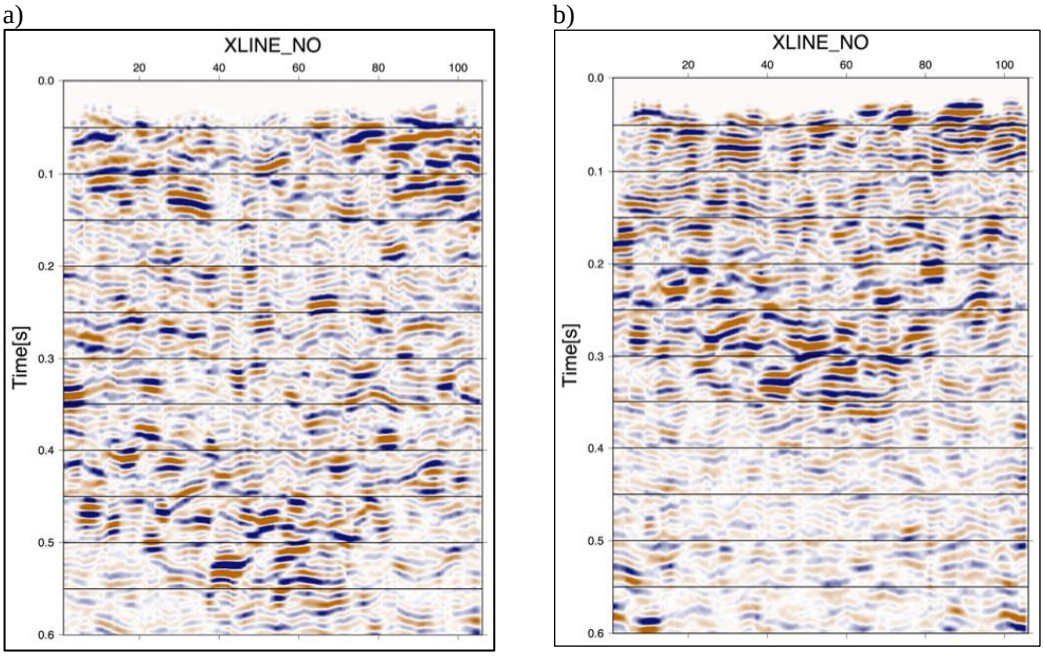

Figure 4-15 X component stack section for in-line 25: (a) S-wave time, and (b) transformed to P-wave time.

4.2.4 Three-component Processing Results

The final S-wave volumes were migrated using Stolt-FK migration. A smooth version of the scaled P-wave RMS velocity field was used for the migration. An example of the results achieved for the horizontal X-component is shown in Figure 4-16. Good continuity was achieved for the X-component. However, a poorer result was achieved for the Y component (Figure 4-17). The sections shown in Figure 4-16 and Figure 4-17 can be compared to the P-wave section (Figure 4-18) by effectively dividing the S-time by 2. The best continuity is identifiable from the P component result with the X component exhibiting poorer continuity and the Y-component exhibiting the poorest continuity. The poorer quality of the X and Y component results may be related to an inferior S-wave static solution or to the elastic properties of the rocks.

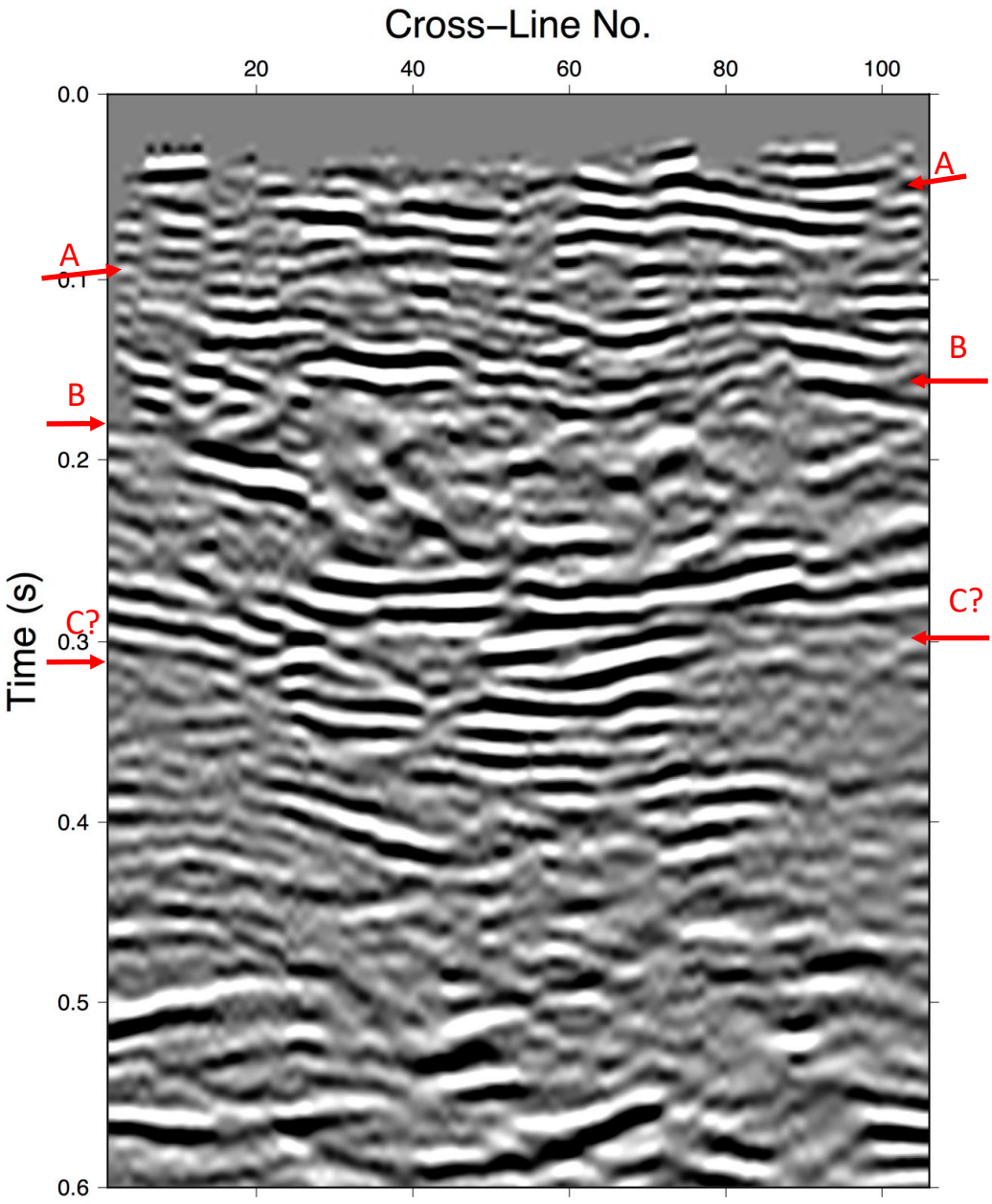

Figure 4-16 Inline 25: Migrated section (horizontal inline (X) component). Arrows (A, B, and C) denote target reflectors.

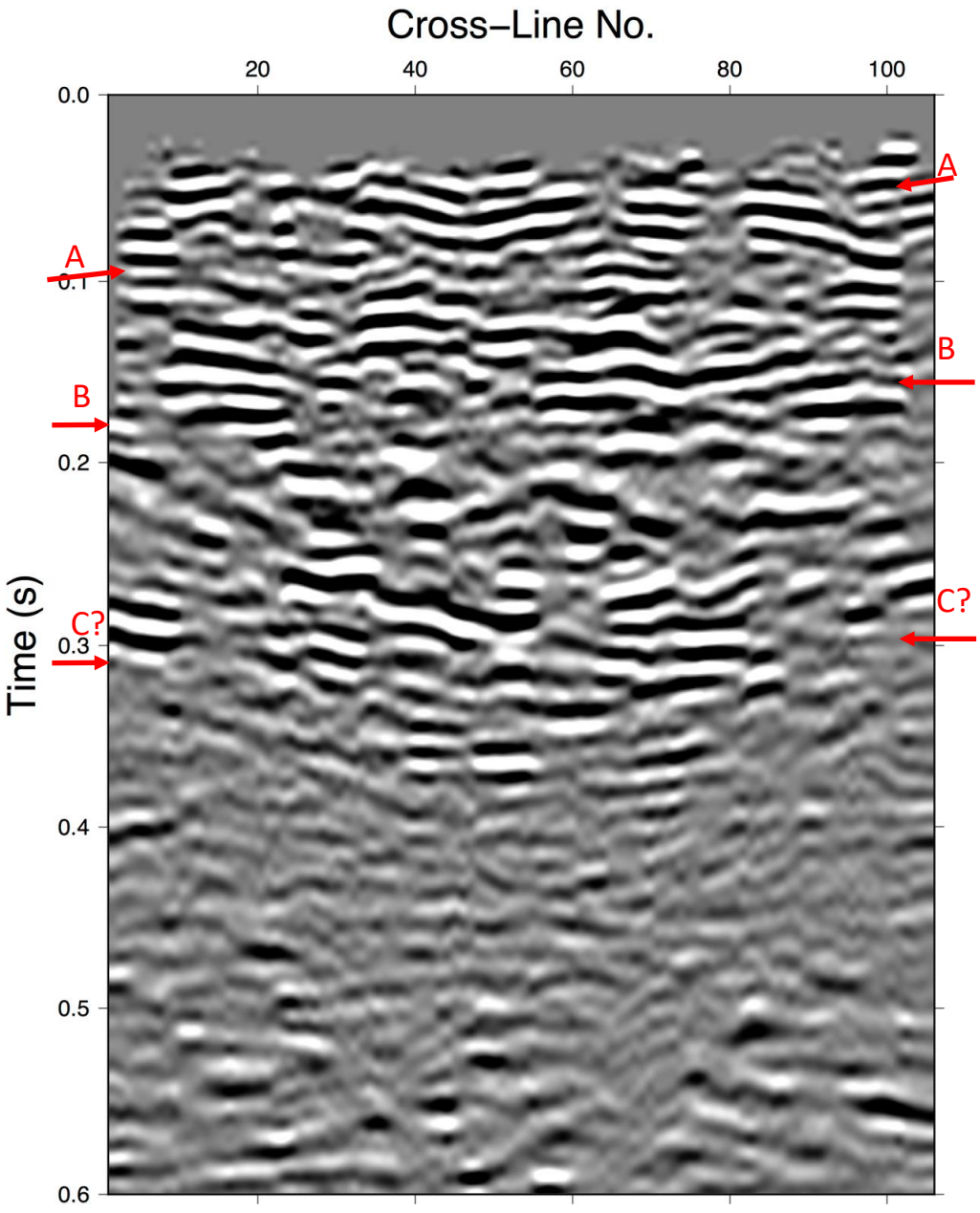

Figure 4-17 Inline 25: Migrated section horizontal (Y) component. Arrows (A, B, and C) mark target reflectors.

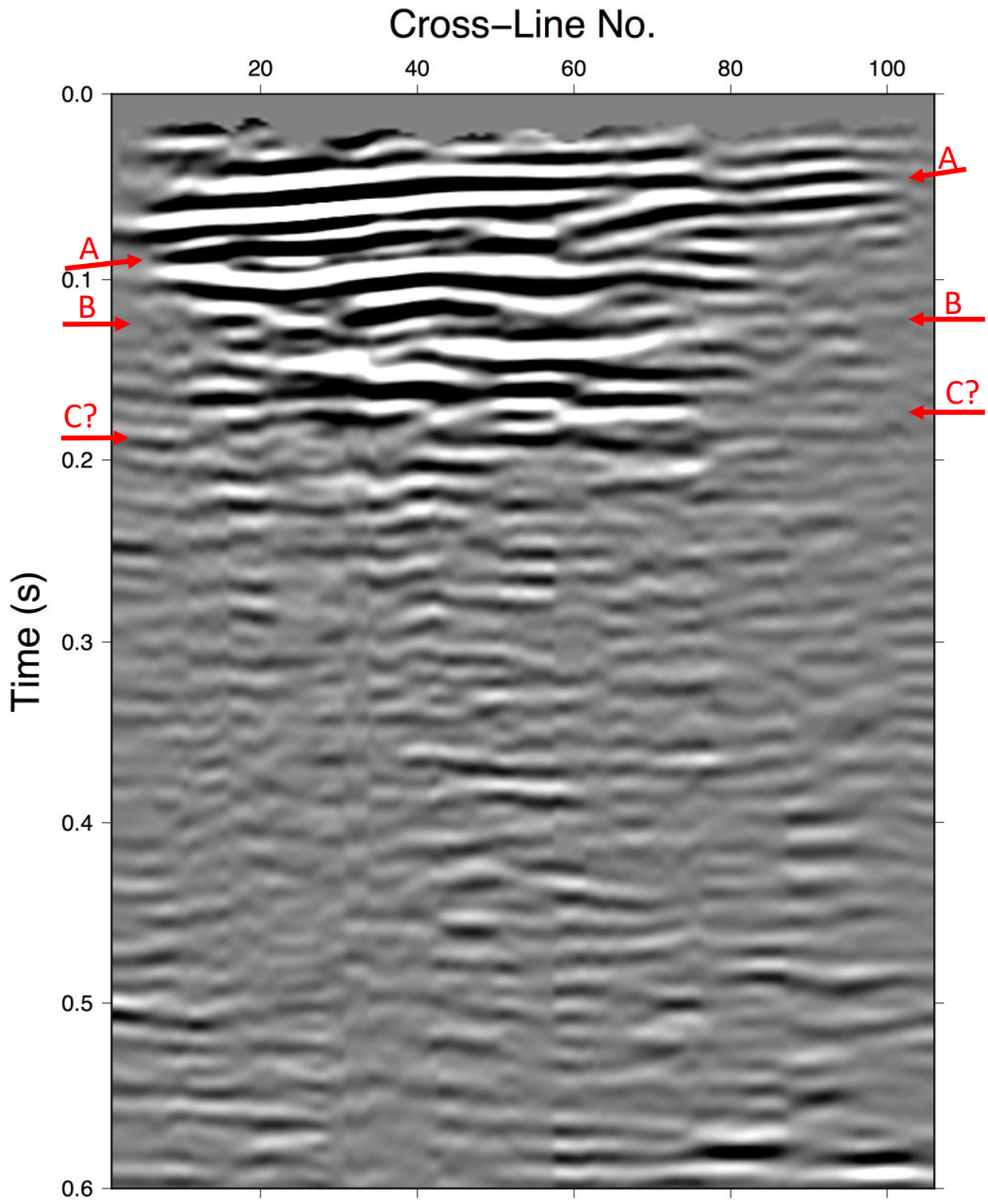

Figure 4-18 Inline 25: Migrated P-wave section, Arrows (A, B, and C) show target reflectors.

Chair display of the 3D migrated amplitude volumes for the horizontal inline (X), and crossline (Y) components in time and converted to depth are presented in Figure 4-19 and Figure 4-20. The vertical component is shown in Figure 4-21 for comparison purposes. As expected, the shear wave data exhibits significantly higher resolution than the P-wave data. The X and Y cubes are quite similar. Some minor differences can be observed, perhaps due to a presence of a weak anisotropy. To fully evaluate these results borehole information is required. The geometry of the P- and S-wave reflections is different. This could be attributed to a highly heterogeneous environment

perhaps associated with rock alterations to which S-waves could be more sensitive than P-waves.

a)

b)

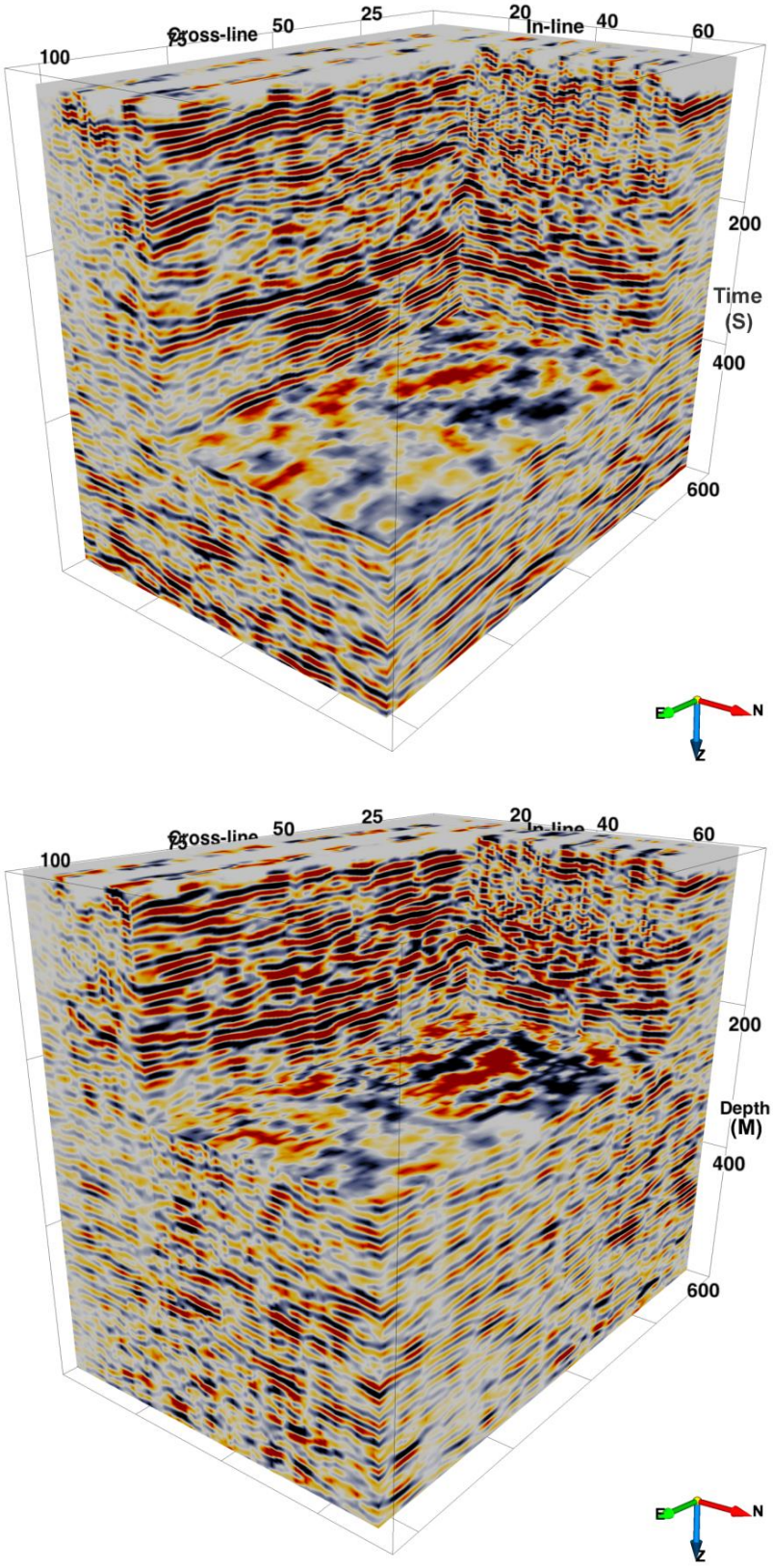

Figure 4-19 Chair display of 3D migrated amplitude cubes for horizontal inline component (X) (a) in time and (b) converted to depth.

a)

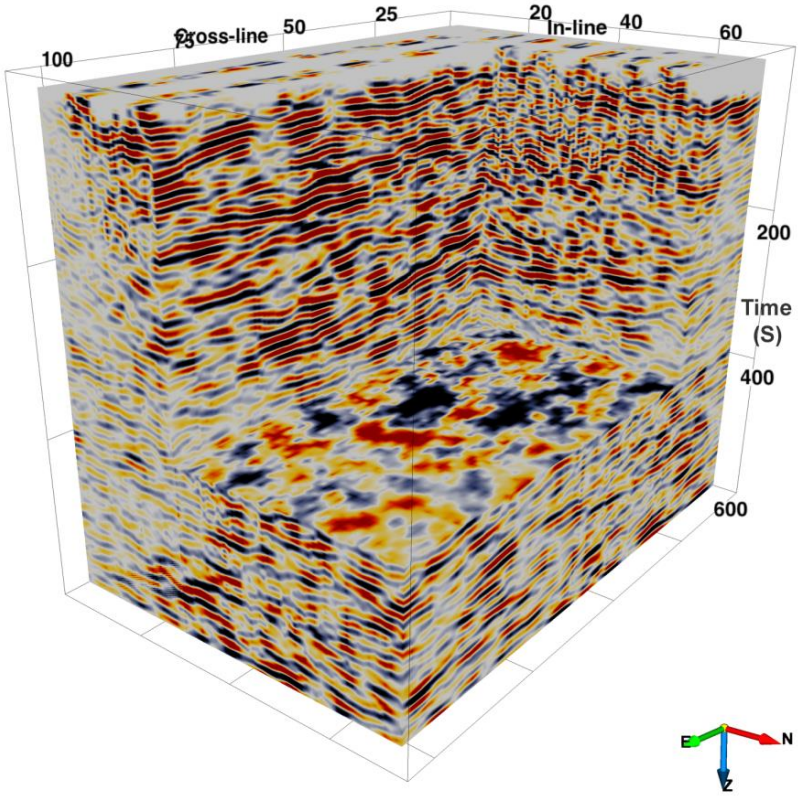

b)

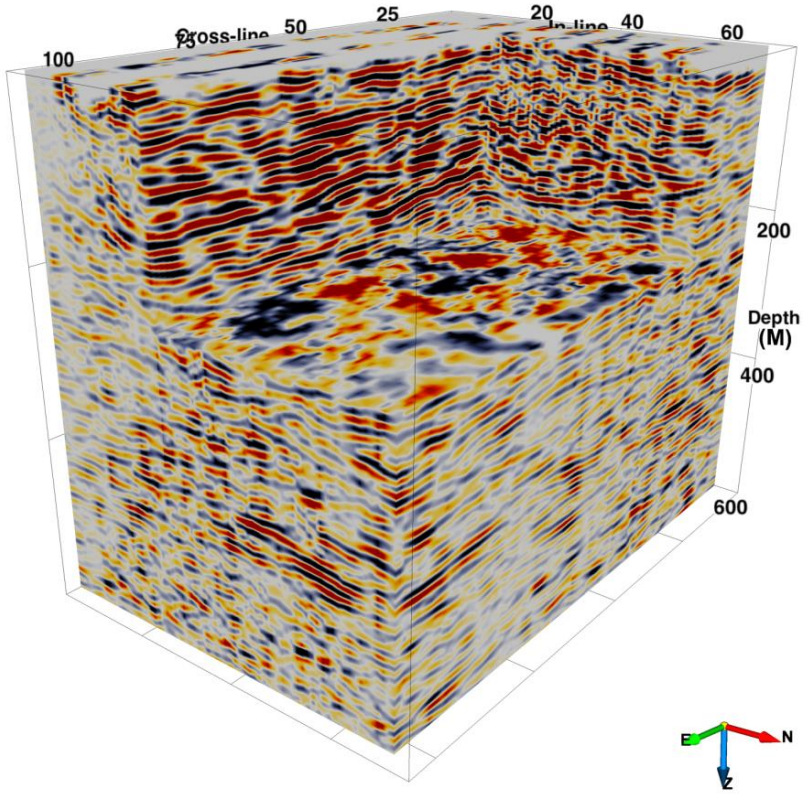

Figure 4-20 Chair display of 3D migrated amplitude cubes for horizontal crossline component (Y) (a) in time and (b) converted to depth.

a)

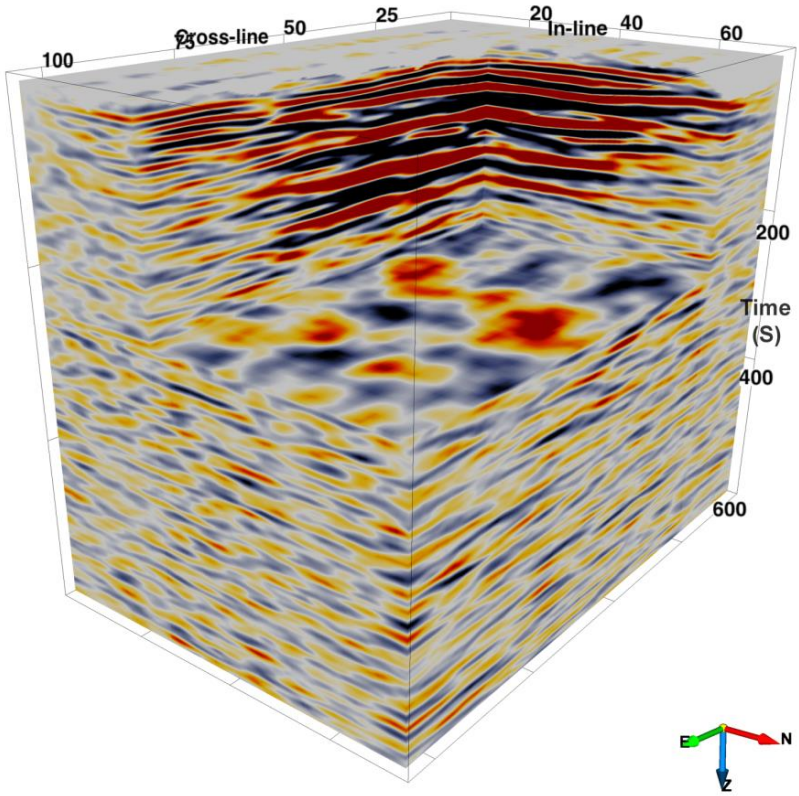

b)

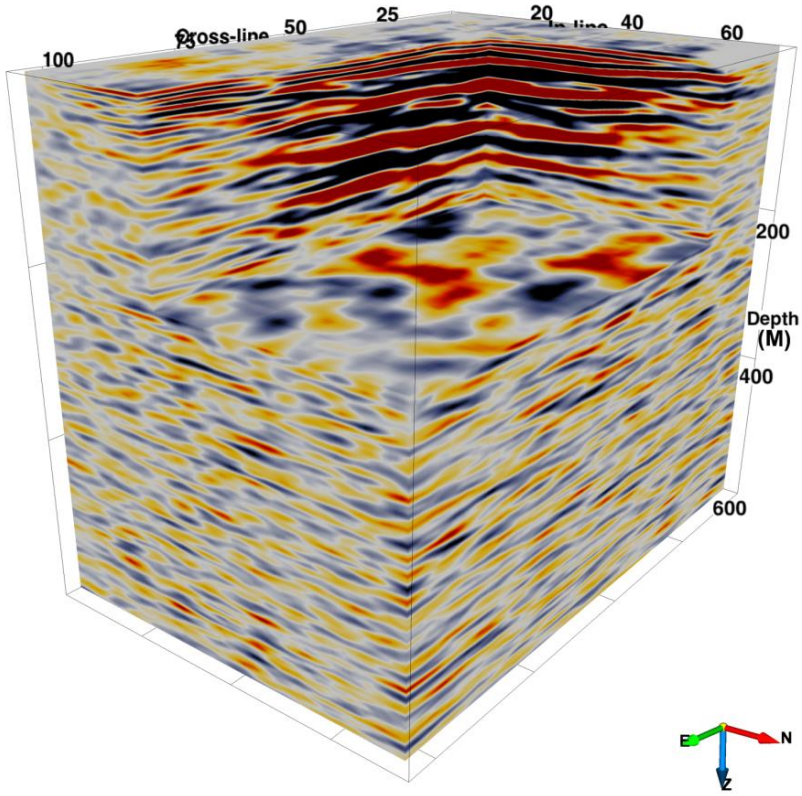

Figure 4-21 Chair display of 3D migrated amplitude cubes for vertical component (Z) (a) in time and (b) converted to depth.

4.2.5 Additional Processing of S-wave Data

To check whether the subsurface properties affected the parameters of the polarisation planes, and to QC the horizontal component rotation step, Polarisation Panel Analysis (PPA) (Urosevic, 2000) was run. PPA consists of successive post-stack migrations of both horizontal components through a range of polarisation angles. The best image is usually obtained for a polarisation angle α for one shear component, while an identical image should be present for 90+α on the other shear component. The difference between the two migrations is an effective way to verify the successful component separation with respect to in situ medium symmetry. The output using this approach is shown in Figure 4-22. The idea behind such analysis is to infer dominant stress direction by matching the best in-line to the poorest cross-line image or to the best cross-line image for inline angle + 90 degrees. If such orthogonality exists, the dominant stress direction is established. This is not precise but it provides some idea of the azimuthal anisotropy if present. From the Figure 4-22, one interpretation is that the dominant stress direction is estimated between 30-60^{o} for the deep reflectors around 400-600 ms. The splitting of the shear waves is weak and as a consequence, anisotropy is low in strength suggesting that its effect onto the processing is not of the first degree of importance. There is no information available onshore about the dominant horizontal stress direction, but 30-60 degree roughly agrees with offshore stress direction along the same parallel.

To eliminate subjectivity when determining the best rotation-angle, an additional technique was developed as part of this project. Each constant rotation angle panel was investigated (trace by trace and sample by sample) to create two output sections. The first section showed the maximum amplitude of any scanned panel (Figure 4-23), while the other section (Figure 4-24) showed the value of the rotation angle of the specific panel that produced the maximum amplitude. The maximum amplitude section provides a virtual seismic section that contains all the important features of the subsurface geological response. The rotation angle section provides the “polarisation angle” attribute that contains information about the dominant shear wave direction. When considering that the stress distribution can change around faults and can as a consequence affect the splitting of S-waves, this tool is very useful to delineate/detect significant geological structures. For the purposes of interpretation/understanding of reflectors and their ability to change polarisation as a consequence of their geological

properties, a composite image was produced, where the maximum amplitude section was overlain by the rotation angle section (Figure 4-25). Such analysis could be used to confirm the presence of structures and a local stress reorientation related caused by them.

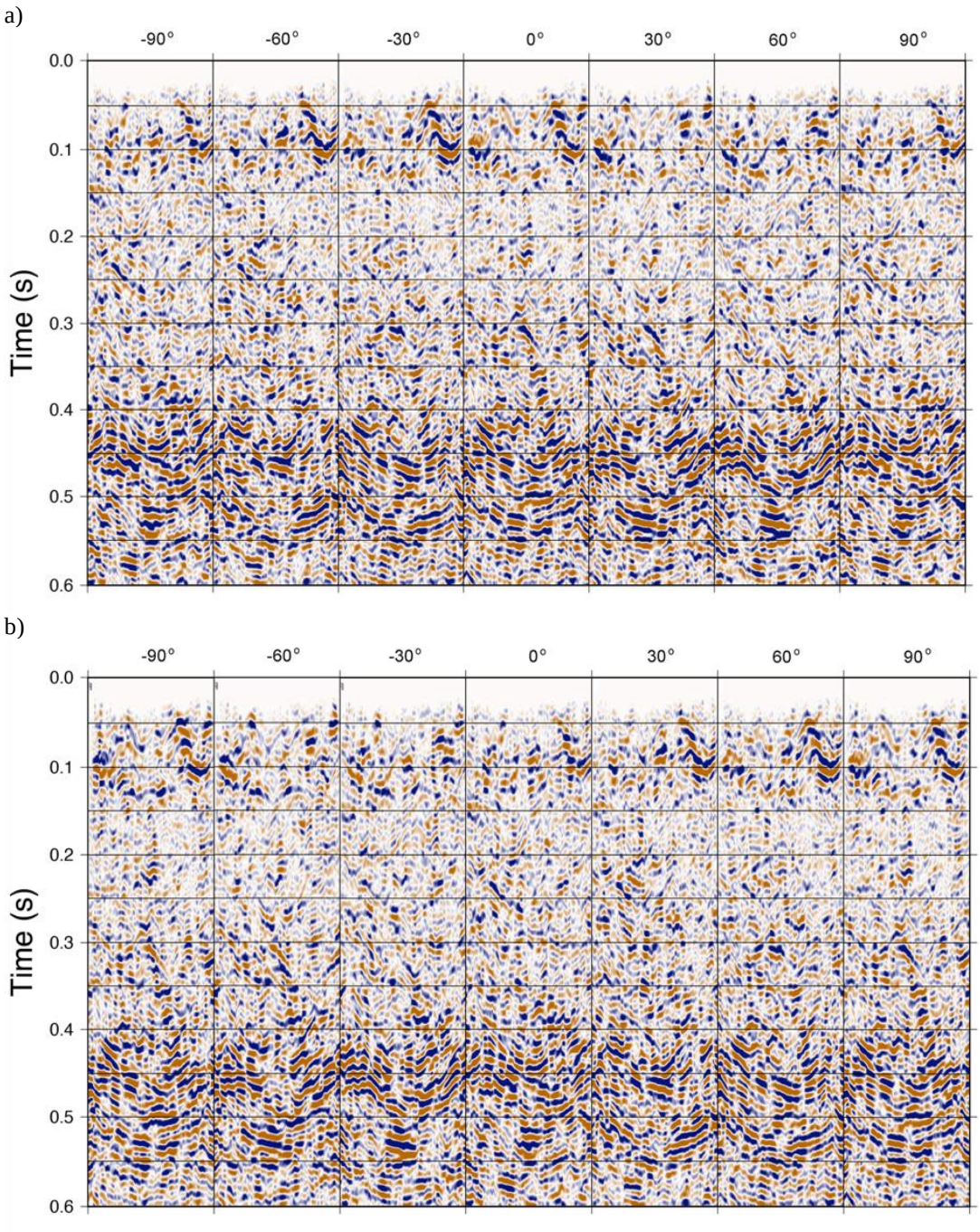

Figure 4-22 Constant angle rotation panels for inline 25: (a) inline (X) component and (b) crossline (Y) component. Inline panels of -90, -60, -30, and 0 degrees are similar to the equivalent crossline panels

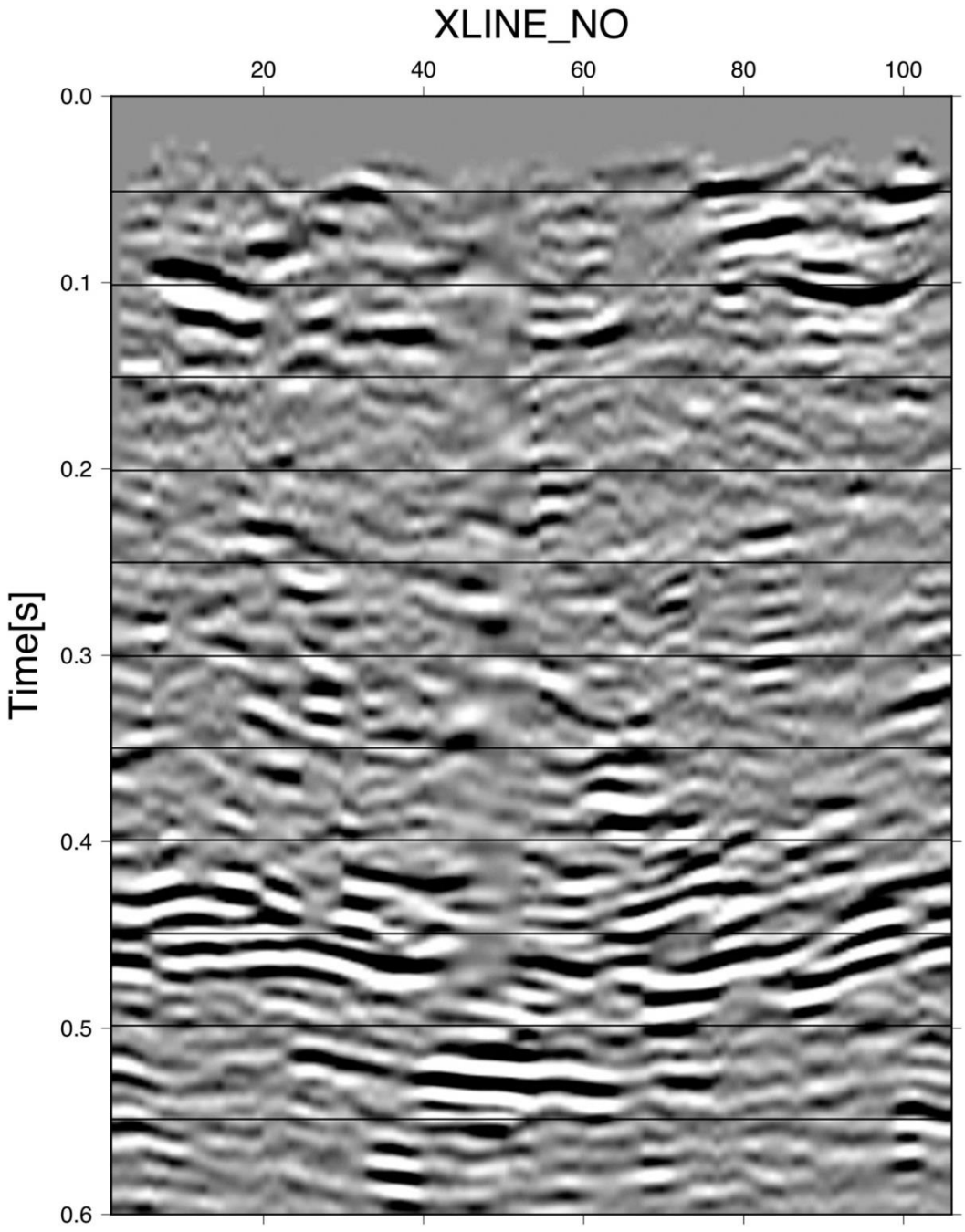

Figure 4-23 Maximum sample value section extracted from polarisation panel analysis sections.

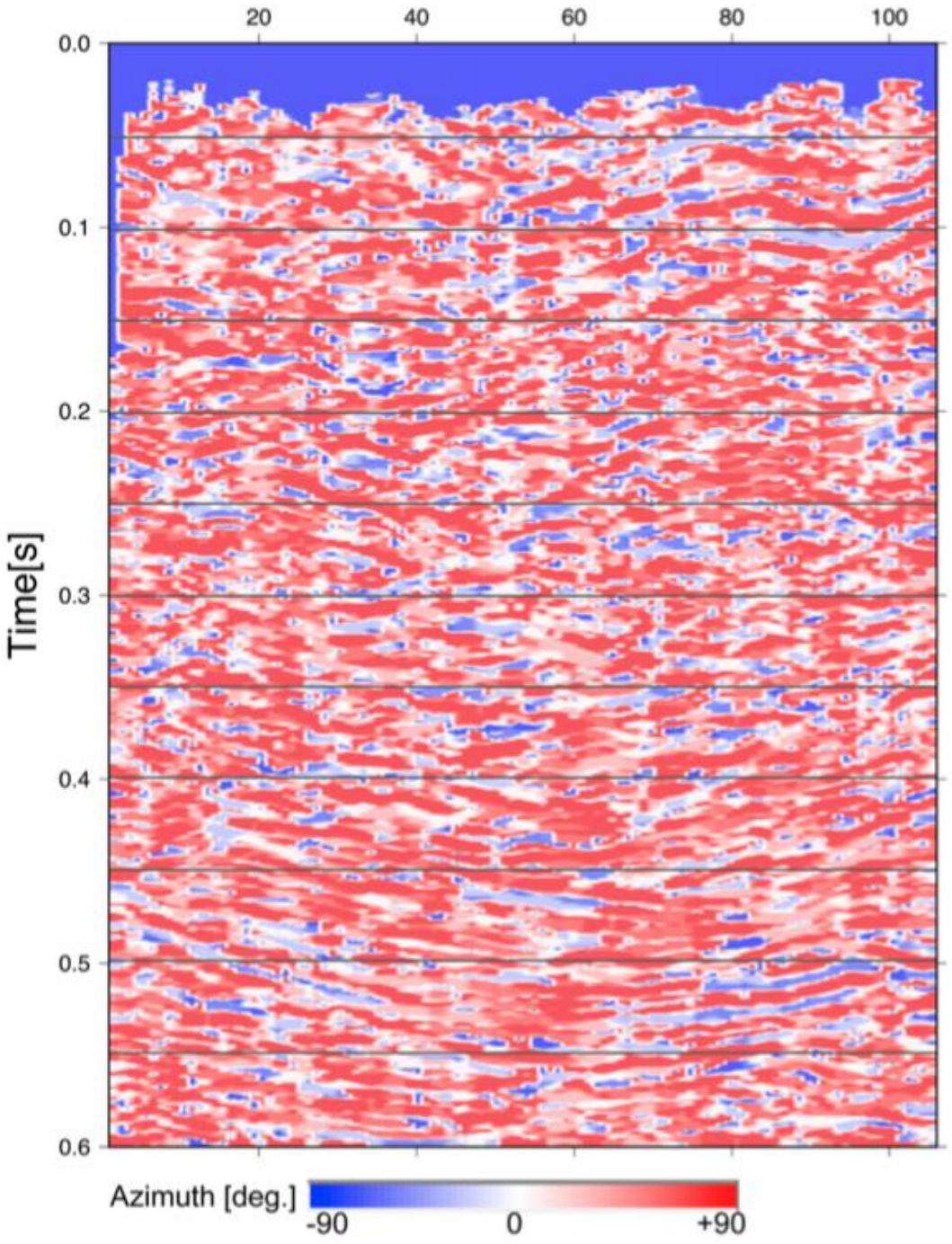

Figure 4-24 Angle of rotation attribute section based on the maximum sample value.

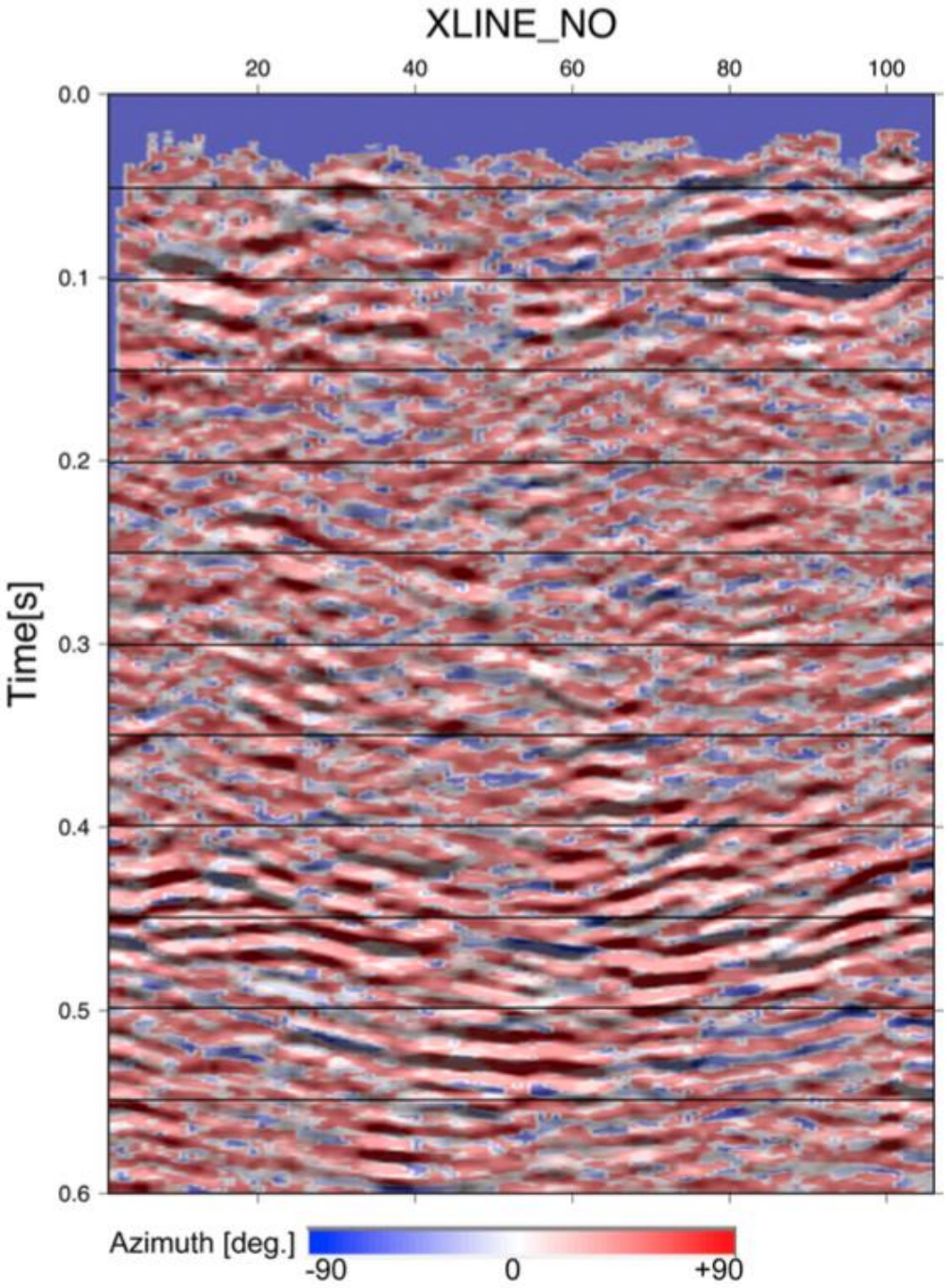

Figure 4-25 Composite display of maximum sample value seismic section and angle of rotation attribute section.

4.2.6 Discussion – S-wave Receiver Static Correction

After obtaining the final 3D migrated P and PS volumes (converted to depth), it was noted that reference reflection on the P crossline data was stable and coincided in depth with the known geology of the region, while the same reflection on the PS crossline data was less stable with deviations in depth almost certainly a result of improperly resolved receiver static corrections. For soft rock environments, this problem can be

resolved by calculating the receiver static corrections using common receiver gathers. However, this is not possible in hard rock environments and it is recommended to perform corrections on the final product. This being so, it was decided to run an additional step using the Multichannel Analysis of Surface Waves (MASW) method to obtain a more precise estimation of the V_P/V_S ratio (Figure 4-26). A reference horizon was picked from the P section (red dotted line in Figure 4-28a) and a corresponding one picked from the PS section (purple line in Figure 4-27a). The difference between the two was calculated in depth and time and applied to the PS migrated section (Figure 4-27). The improvement in the continuity and dip of the shallow reflectors should be highlighted.

The accuracy of hand-picked S-wave refractions or S-wave reflector could be problematic due to low SNR. V_S was estimated in this case, which also could cause further errors. Normally the residual static calculation can resolve these problems to some extent and improve the coherency but as it is explained in section 2.3.2, the calculation of residual statics is also affected by variations in the CCP coordinates with depth. This could be one of the reasons that only the continuity and dip of the shallow reflectors are improved.

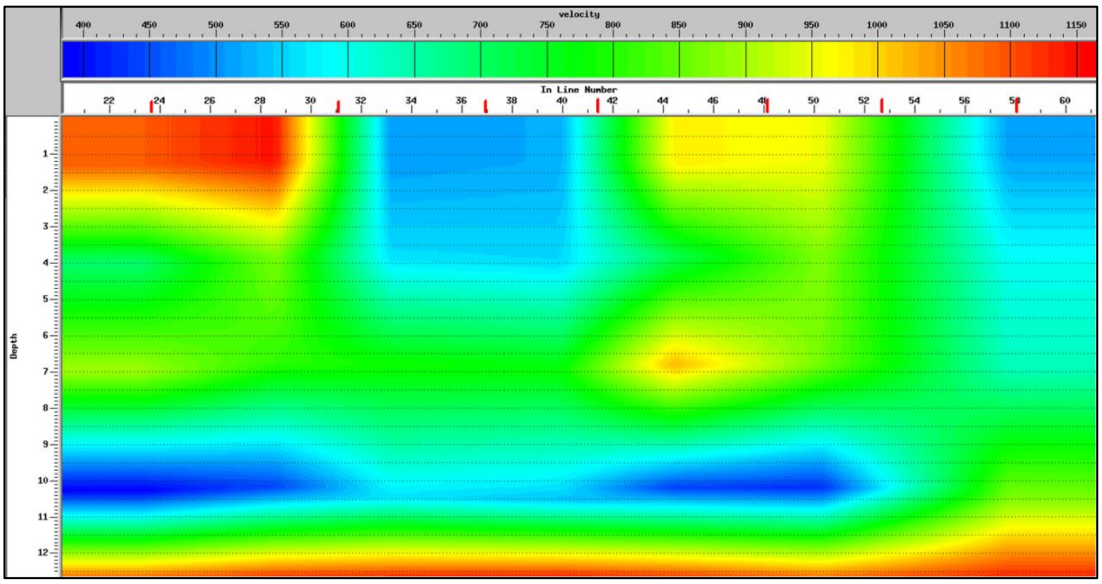

Figure 4-26 S interval velocity model in depth derived from Multichannel Analysis of Surface Waves (MASW) used as an initial model to calculate VP/VS. This ratio was used to calculate S receiver static values.

Figure 4-28a shows a P migrated section while Figure 4-28b shows a migrated converted wave (PS) section (previously converted to P time) after applying the receiver statics correction. A reflector clearly identifiable from the PS section does not occur on the P section. This difference is evidence that the generation of a PS volume is very important in a hard rock environment – certainly for the area under investigation for this project. As there are no available case histories or literature that suggest how to overcome basic issues in converted wave processing, further investigations and tests (fieldwork/numerical modelling) would be of a great benefit to produce even better results.

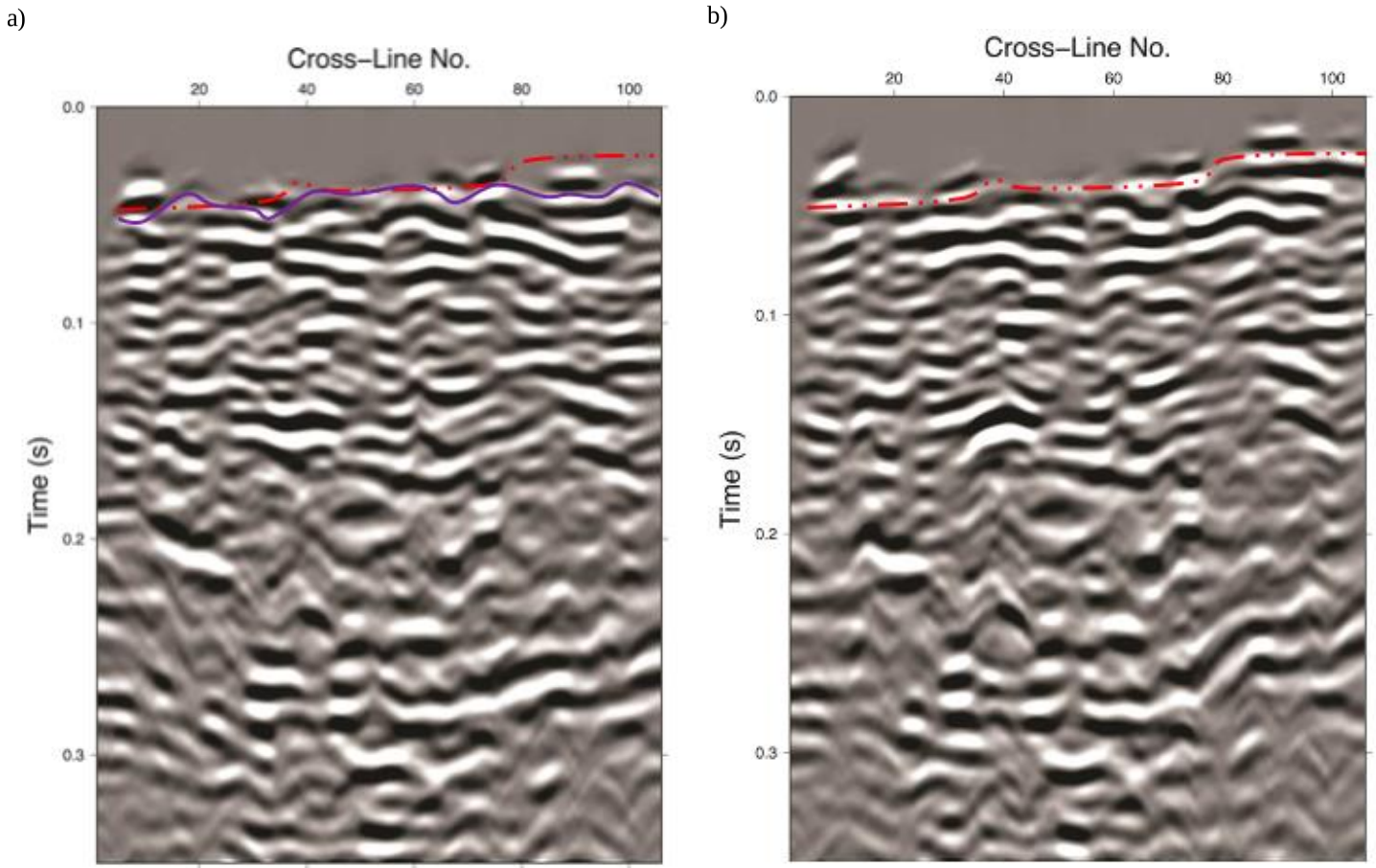

Figure 4-27 Inline 25: Migrated section horizontal inline (X) component converted to P-time (a) before and (b) after application of the hand-picked S statics. Note the improvement in the continuity and dip of the shallow reflectors in (b) compared to (a). The red dashed line is the picked horizon from the P-wave section and the purple line is the same horizon picked from the X-component data.

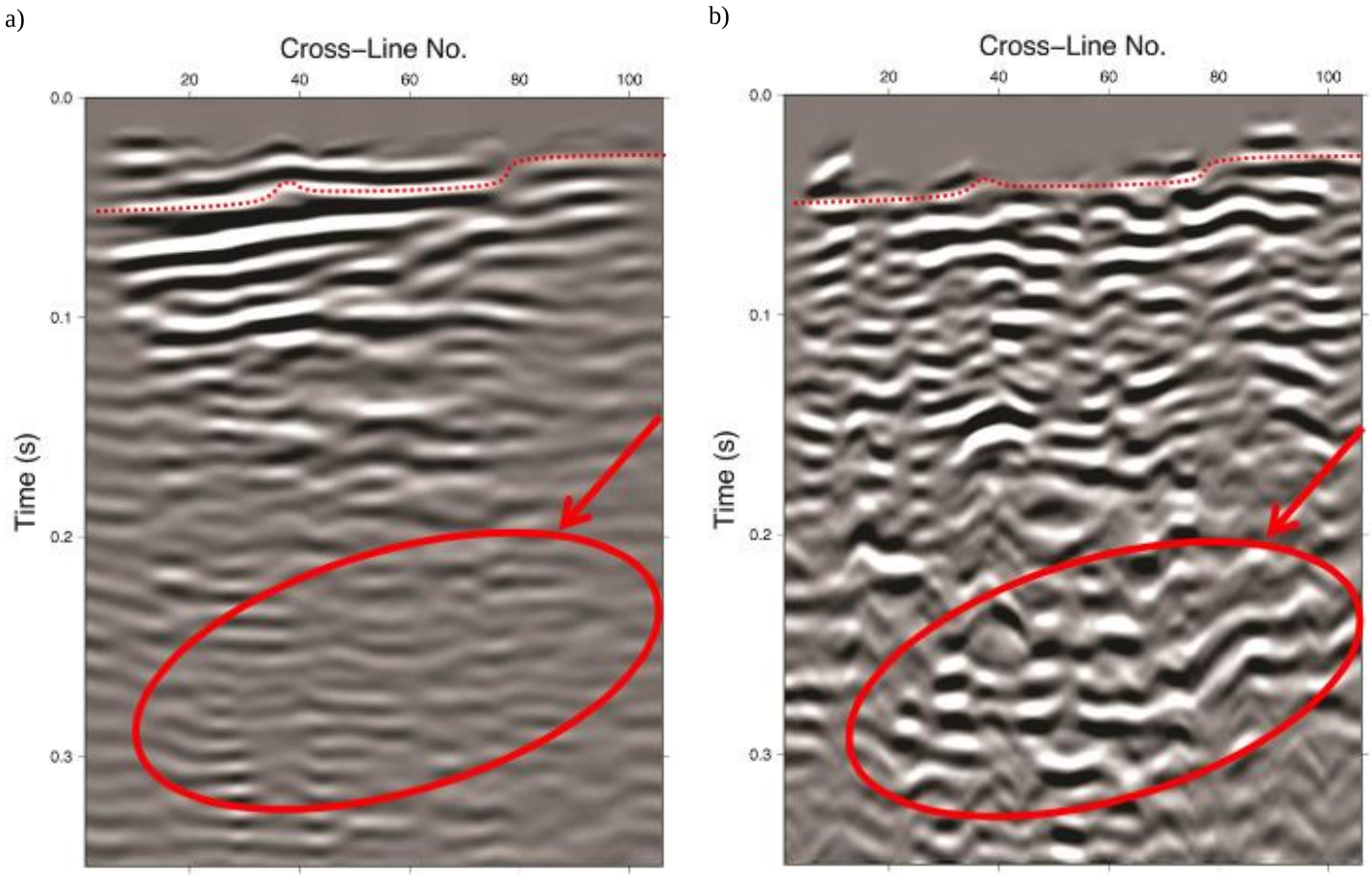

Figure 4-28 Inline 25: Migrated section a) vertical component and (b) horizontal inline (X) component converted to P-time**.** Note the horizon highlighted by a red dashed line and the package highlighted by the red ellipse. The static issue is still visible in horizontal component specially in the highlighted package.

Chapter 5 Final Discussion, Conclusions and Recommendations

5.1 Final Discussion

Exploration in hard rock environments using seismic methods is gaining momentum and more and more promising case histories are being published (Urosevic et al., 2017). However, correlating conventional seismic images to lithology is not straightforward. Additional measurements and calibrations are required. Unfortunately, borehole velocity measurements (Full Wave Sonic (FWS)) are a rarity in mineral exploration. In the absence of logs like FWS, at least measurements on core samples are needed to correlate seismic to lithology. Unfortunately, very often correlation of seismic is attempted against the proposed geological model which can be the source of misunderstanding.

The issues faced are significant with the two most important relating to the following:

- Resolution,
- Relating rock types or rock alteration to seismic events.

The seismic wavelength for P-wave data in a hard rock environment is typically 120-140 m while the Fresnel zone is in the order of 250 m and greater. Most features we are attempting to identify using the seismic data are often much smaller. Concentrated ore deposits such as the VMS deposits of Kambalda in Australia are often of a similar extent to the nominal size of Fresnel zone but in terms of vertical resolution is an order of magnitude thinner than the dominant wavelength (Urosevic et al., 2012). Moreover, seismic P-wave amplitudes or velocities are not readily interpretable in terms of lithology. In some cases, they are indeed indicative of the lithology. This can be utilised only after very thorough calibration. In general, there may be many different lithologies possessing very similar P-wave seismic velocities, hence more information is needed to discriminate between them. This can be S-wave velocities, amplitudes or other seismic attributes. For example, Table 3-1 shows anomalous P and S wave velocities in certain depth interval, which coincides with increased zinc content.

Some of the above issues, could be possible to address by the application of multi-component seismology. This may provide us with additional information for the following reasons:

- S-wave, due to lower velocity and thus shorter wavelength, often produce superior resolution data to P-wave,
- P- and S-wave velocities and particularly V_P/V_S ratio provide additional parameter for rock characterisation.

Unfortunately, what acts against these potential advantages of the application of multi-component seismology is its high cost and long delivery time for the results. In case of no budget constraints, application of dual sources would resolve statics issues much better and most likely produces better S-wave images than what was produced in this thesis. However, the reality of the hard rock seismic exploration is that the current costs for acquiring a line or a square kilometre of reflection seismic is more likely to go down rather than going up. Consequently, the most probable mode of the multi-component seismology will be using P-wave source and 3C receivers, as are the cases presented in this work. While this simple mode of data acquisition makes multi-component surveys more economically viable, processing is far more difficult and if no good calibration is available, interpretation will be even harder. This is extending the delivery time which erodes the confidence of mine geologists towards the use of such "higher order" seismic.

After analysing examples from West and South Australia, it can be concluded that the successful application of a simplified version of multi-component seismology is dependent on the geological setting. The occurrence of a high velocity contrast between weathered and fresh rock will result in significant P- to S-wave conversion and as a consequence will allow for the computation of a good quality S-wave refraction static solution and subsequent S-wave reflection stack. Even though achieving a high-quality converted wave result represents a far greater challenge than achieving an equivalent P-wave result, it has two major advantages over P-waves:

a) S-wave velocities are easier to correlate directly with rock properties as they only depend on μ whereas P-wave velocities depend upon $\lambda + 2\mu$,

b) S-waves have two different modes (SV and SH). The two modes can provide additional information about the subsurface that could be of particular importance when investigating rock alterations often related to mineralisation.

5.2 Conclusions

The main objective of this research was to understand and evaluate the potential and applicability of multi-component seismic for exploration of mineral resources. The method was tested by analysing all stages of a multi-component survey from survey design and acquisition to data processing analysis and interpretation.

Two multi-component surface seismic field data sets were acquired: a 2D (MSDP10) and a 3D (Roy Hill). The author participated in the acquisition of the data and at the time of writing this thesis has been the only person who has conducted subsequent analysis and interpretation. It should be noted that both data sets were acquired in suboptimal conditions.

For the MSDP10 survey, the combination of a weight drop source for the geological setting did not favour a multi-component survey. Even though the processing carried out was complex, the results achieved were encouraging.

The Roy Hill survey was acquired in an area that was highly heterogeneous and absorptive and as a consequence not ideal for investigation by any geophysical method. Further complications resulted from a highly irregular acquisition geometry giving rise to very inconsistent coverage and fold. Even with these complications, the study of the data successfully proved the applicability of multi-component seismology. The results achieved are positive, and further work with better survey optimisation is hoped to be conducted in the near future.

This study was conducted through two steps:

1. A learning processs using modelled data to determine the best approach and hence processing sequence to analyse a multi-component wavefield,
2. Analysis of the field data utilising lessons learnt from the modelled data.

As it was mentioned in chapter 2, each body wave mode provides different information (contained in the reflected wavefield) about the subsurface geology. In practice due to various issues with S-wave processing and generally low SNR of this mode, significant differences between the final images of different modes are expected, certainly much more than those images produced by simplified synthetic models.

Even though the field data had a much lower signal to noise ratio than the modelled

data, the analysis carried out using the modelled data proved to be very effective approach to define the best C–wave algortihms and interpretation techniques for the field data. This strategy will be more effective in case good calibration of seismic to borehole data is available.

Processing of C-waves is complex. Many different conversion modes are possible and it is not obvious which one is favoured by the ground conditions. Borehole control and modelling may help resolving this issue.

To efficiently handle shear wave polarisation for the 3D dataset, a new approach for the rotation analysis was introduced. The new algorithm was successfully used to exclude acquisition imprint by subtracting the receiver azimuth from the angle of rotation. By using the resultant residual angles of rotation, zones with anomalous angles of rotation were correlated with subsurface geological structures where shear wave splitting has possibly affected the angle of rotation. This could have been verified, by analysing downhole logs, VSP or rock samples. However, only density and mineralisation logs were available for this project and it was not possible to confirm with any confidence that the anomalous rotations correlated with shear wave splitting.

In the 2D area, analysis of the seven downhole core samples provided by the Geological Survey of South Australia (GSSA) showed that there were differences between the measured V_P, V_S and the V_P/V_S ratio for the radial and axial measurements of the samples. This indicated anisotropy that looked to increase in strength with depth. It was also noted that in Poisson ratio correlated with a drop in V_P and V_S below 490m. This coincides with a mineralised zone (Fabris et al., 2017). The correlation is likely to be indicative of mineral alterations but further investigation and evaluation is required to confirm this. The limited data available from borehole MSDP10 highlighted the need for more comprehensive downhole data so that additional analyses can be carried out to correlate with the seismic data. Any resulting correlations can then be used for other datasets (such as the one from the Roy Hill survey) to greatly increase the confidence of the interpretation of analysis.

Polarisation Panel Analysis (Urosevic, 2000) was also evaluated to determine the fast shear direction and confirm the anisotropy. The two outputs from process provided a

virtual seismic section (containing potentially important features of the subsurface geology) and a "polarisation angle" attribute section (providing information about the dominant shear wave direction). When it is considered that stress distribution can change around faults, and as a result affect the splitting of S-waves, this tool is likely to be very useful to better define/image significant geological structures. To obtain a better understanding of polarisation changes and the nature of the reflectors and hence their geological properties, a composite image was successfully used, where the maximum amplitude section was overlain by rotation angle section.

One of the most challenging steps of the shear wave processing was generating a converted wave statics solution. Different mode conversion options were considered, each with a different choice of time delay computation. To compute S-wave statics in a conventional way it is necessary to pick first S-wave arrival times. These are particularly hard to pick as they do not occur as first arrivals but occur in the "middle" of a shot record. It was decided to use a combination of Multichannel Analysis of Surface Waves (MASW) and picked horizons (as a reference) to compute 3D statics. This proved to be the most successful approach for the 3D dataset.

From the case studies analysed, the following can be concluded:

I) For the case of a heterogeneous regolith with a strong velocity contrast with the underlying rock, the use of a P-wave source and 3C receivers is very likely to provide equally good PP and PSSP modes. Acquisition costs will be only a marginally higher but the potential benefit of 3C seismic for rock characterisation may be significant.

II) Where a mild or low velocity contrast occurs between the regolith and underlying rock as encountered in the MDPS10 area, a combination of a P-wave source and 3C receivers is not favourable option. An S-wave source is recommended to take advantage of the additional information from 6C or 9C recording. However, this will make both acquisition and processing costs much higher than those currently accepted in the mineral sector.

III) More development of converted wave processing in hard rocks is required to standardise the processing sequence by acquiring and analysing more surveys in different geological settings.

From this study, it can be concluded that the multi-component seismic method has a high potential for mineral exploration by determining different properties of complex geology that occur in hard rock environments. In particular, measurements of the full wavefield is likely to play a key role in understanding the seismic response of rock alterations which are of great interest in mineral exploration. However, at present the potential of multi-component seismology needs to be further evaluated through hopefully many new case histories. That will enable the survey design, the data processing sequence and QC to be used and standardised for mineral exploration.

5.3 Recommendations and Future Work

3C seismic data acquisition requires proper planning and design as well as constant monitoring and QC of the recorded data. As the velocity of the S-waves is lower compared to the P-waves, spatial sampling (distance between receivers) must be evaluated with respect to the S-wave velocity profile in order to avoid spatial aliasing. The recording time for each shot must be long enough for S-wave imaging and determination of the V_P/V_S ratio. When processing the 3C data, achieving a good SNR is very important. To achieve that, a high energy source is required and the survey must be designed to achieve good coverage and high fold data.

Different types of sources generate different types of P and S radiation patterns. The consistency of the source radiation pattern is further affected by variable near surface conditions. Both factors will affect image quality. This being so, field tests should be carried out in order to optimise P and S energy in terms of their ratio balance and detectability when using a 3C recording system. When the source parameters have been determined the far field energy should be checked and frequency content monitored.

Even though a “pure” P-wave source such as vibroseis is generally not recommended, it can still produce a significant amount of S-wave energy in favourable conditions in a hard rock environment. For example, in Yilgarn craton in WA, where the regolith is thin and heterogeneous and has a high contrast in elastic properties with underlying rock. These conditions also occur in the Kambalda region in WA, and it is recommended that further testing of multi-component seismology takes place in this area.

References

Adam, E., G. Perron, G. Arnold, L. Matthews, and B. Milkereit. 2000, 3-D seismic imaging for VMS deposit exploration, Matagami, Quebec, SEG Technical Program Expanded Abstracts 2000: Society of Exploration Geophysicists. 1093-1096.

Ahmadi, P., and A. Malehmir. 2013, Elastic Anisotropy of Deformation Zones-From Lab Measurements to Real Seismic Data, an Example from Eastern Sweden. Paper read at 75th EAGE Conference & Exhibition incorporating SPE EUROPEC 2013.

Aki, K., and P. Richards. 1980, Quantitative seismology: Theory and methods. San Francisco.

Alford, R. 1986, Shear data in the presence of azimuthal anisotropy: Dilley, Texas, SEG Technical Program Expanded Abstracts 1986: Society of Exploration Geophysicists. 476-479.

Allen, S., C. Simpson, J. McPhie, and S. Daly. 2003, Stratigraphy, distribution and geochemistry of widespread felsic volcanic units in the Mesoproterozoic Gawler Range Volcanics, South Australia. Australian Journal of Earth Sciences, 50, no. 1,97-112.

Bansal, R., and J. Gaiser. 2013, An introduction to this special section: Applications and challenges in shear-wave exploration. The Leading Edge, 32, no. 1,12-12.

Bellefleur, G., A. Malehmir, and C. Müller. 2012, Elastic finite-difference modeling of volcanic-hosted massive sulfide deposits: A case study from Half Mile Lake, New Brunswick, Canada. Geophysics, 77, no. 5,WC25-WC36.

Bellefleur, G., L. Matthews, B. Roberts, B. McMonnies, M. Salisbury, G. Perron, D. Snyder, and J. McGaughey. 2004a, Downhole seismic imaging of the Victor kimberlite, James Bay Lowlands, Canada: A feasibility study, SEG Technical Program Expanded Abstracts 2004: Society of Exploration Geophysicists. 1229-1232.

Bellefleur, G., C. Müller, D. Snyder, and L. Matthews. 2004b, Downhole seismic imaging of a massive sulfide orebody with mode-converted waves, Halfmile Lake, New Brunswick, Canada. Geophysics, 69, no. 2,318-329.

Berson, I. S. 1957, High-frequency seismic: Moscow. the USSR Academy of Science (in Russian).

Bierbaum, S. J., and S. A. Greenhalgh. 1998, A high-frequency downhole sparker sound source for crosswell seismic surveying. Exploration Geophysics, 29, no. 3/4,280-283.

Bohlen, T. 2002, Parallel 3-D viscoelastic finite difference seismic modelling. Computers & Geosciences, 28, no. 8,887-899.

Bohlen, T., D. De Nil, K. Daniel, and S. Jetschny. 2015, SOFI3D, seismic modeling with finite differences 3D-elastic and viscoelastic version, User's Guide. Karlsruhe Institute of Technology, Karlsruhe.

Bohlen, T., C. Müller, B. Milkereit, D. Eaton, and M. Salisbury. 2003, Elastic seismic wave scattering from massive sulfide orebodies: on the role of composition and shape. Hardrock seismic exploration: SEG, 70,89.

Brodic, B. 2017, Three-component digital-based seismic landstreamer: Methodologies for infrastructure planning applications, Acta Universitatis Upsaliensis.

Campbell, G. 1994, Geophysical contributions to mine-development planning: a risk reduction approach. Paper read at Fifteenth CMMI Congress.

Campbell, G., J. Crotty, D. Ross-Watt, and P. Robinson. 1990, 3-D seismic mapping for mine planning purposes at the South Deep Prospect. Paper read at Proceedings International Deep Mining Conference: SAIMM Symposium Series S1O.

Campbell, G., and D. Peace. 1984, Seismic reflection experiments for gold exploration, Wits Basin, Republic of South Africa. Paper read at 46th Meeting and Technical Exhibition. European Association of Exploration Geophysicists, London (June 19–22).

Cao, S., and S. Greenhalgh. 1997, Cross-well seismic tomographic delineation of mineralization in a hard-rock environment. Geophysical Prospecting, 45, no. 3,449-460.

Chopra, S., and R. Stewart. 2010, Introduction to this special section: multicomponent seismic. The Leading Edge, 29, no. 10,1210-1211.

Cosma, C. 1983, Determination of rock mass quality by the crosshole seismic method. Bulletin of the International Association of Engineering Geology, 26, no. 27,219-226.

Cosma, C., P. Heikkinen, and J. Keskinen. 2003, Multiazimuth VSP for rock characterization of deep nuclear waste disposal sites in Finland, Hardrock seismic exploration: Society of Exploration Geophysicists. 207-226.

Cosma, C., P. Heikkinen, J. Keskinen, and N. Enescu. 2001, VSP in crystalline rocks—from downhole velocity profiling to 3-D fracture mapping. International Journal of Rock Mechanics and Mining Sciences, 38, no. 6,843-850.

Cosma, C., A. Wolmarans, and N. Enescu. 2005, Kimberlite delineation by seismic side-scans from boreholes. Paper read at 67th EAGE Conference & Exhibition.

Crampin, S. 1981, A review of wave motion in anisotropic and cracked elastic-media. Wave motion, 3, no. 4,343-391.

Crampin, S. 1985, Evaluation of anisotropy by shear-wave splitting. Geophysics, 50, no. 1,142-152.

Dewey, J., and P. Byerly. 1969, The early history of seismometry (to 1900). Bulletin of the Seismological Society of America, 59, no. 1,183-227.

Dobrin, M. B. 1951, Dispersion in seismic surface waves. Geophysics, 16, no. 1,63-80.

Drummond, B. J., B. R. Goleby, A. Owen, A. Yeates, C. Swager, Y. Zhang, and J. Jackson. 2000, Seismic reflection imaging of mineral systems: Three case histories. Geophysics, 65, no. 6,1852-1861.

Duff, D., C. Hurich, and S. Deemer. 2012, Seismic properties of the Voisey's Bay massive sulfide deposit: Insights into approaches to seismic imaging. Geophysics, 77, no. 5,WC59-WC68.

Duncan, G., M. Downey, L. Leung, and P. Harman. 1989, The development of cross hole seismic techniques and case studies. Exploration Geophysics, 20, no. 1/2,127-130.

Durrheim, R. 1986, Recent reflection seismic developments in the Witwatersrand basin. Reflection seismology: A global perspective, 13,77-83.

Dzunic, A. M., P. Ahmadi, M. Madadi, and A. Bona. 2016, Introducing 3rd dimension into 2D reflective seismic exploration in the complex hard rock environment. ASEG Extended Abstracts, 2016, no. 1,1-4.

Eaton, D. W., E. Adam, B. Milkereit, M. Salisbury, B. Roberts, D. White, and J. Wright. 2010, Enhancing base-metal exploration with seismic imagingThis article is one of a series of papers published in this Special Issue on the theme Lithoprobe—parameters, processes, and the evolution of a continent. Canadian Journal of Earth Sciences, 47, no. 5,741-760.

Eaton, D. W., B. Milkereit, and M. H. Salisbury. 2003, Hardrock seismic exploration: Mature technologies adapted to new exploration targets, Foreword to hard rock seismic exploration: Society of Exploration Geophysicists.

Evans, B., M. Urosevic, and A. Taube. 2003, Using surface-seismic reflection to profile a massive sulfide deposit at Mount Morgan, Australia, Hardrock seismic exploration: Society of Exploration Geophysicists. 157-163.

Fabris, A. J., L. Tylkowski, J. Brennan, R. Flint, B., A. Ogilvie, S. McAvaney, M. Werner, M. Pawley, C. Krapf, A. Burtt, C., R. Rowe, C. Henschke, N. Chalmers, C., S. Rechner, I. Hardwick, and J. Keeling. 2017, Mineral Systems Drilling Program in the southern Gawler Ranges, South Australia, Report Book 2016/00030 Department for the Premier and Cabinet.

Falkovskiy, A. F., J., Robert; Angelovich, Steve 2015, A Simple Method for Computing Conversion Point Coordinates: Application to 3D CCP Binning. GeoConvention 2015: New Horizons.

Farfour, M., and W. J. Yoon. 2016, A review on multicomponent seismology: A potential seismic application for reservoir characterization. Journal of advanced research, 7, no. 3,515-524.

Frappa, M., and C. Molinier. 1993, Shallow seismic reflection in a mine gallery. Engineering Geology, 33, no. 3,201-208.

Friedel, M., M. Jackson, D. Scott, T. Williams, and M. Olson. 1995, 3-D tomographic imaging of anomalous conditions in a deep silver mine. Journal of applied geophysics, 34, no. 1,1-21.

Friedel, M., D. Scott, M. Jackson, T. Williams, and S. Killen. 1996, 3-D tomographic imaging of anomalous stress conditions in a deep US gold mine. Journal of applied geophysics, 36, no. 1,1-17.

Fromm, G., H. Kreyt, and B. Wiest. 1985, Static and dynamic corrections, in Dohr, G. Ed., : Seismic Shear Waves.: Seismic shear waves: Handbook of geophysical exploration, 15a, no. Geophysical Press.

Gaiser, J. 2016, 3C Seismic and VSP: Converted waves and vector wavefield applications: Society of Exploration Geophysicists.

Gamburtsev, G., Y. Riznichenko, and I. Berson. 1952, Correlation method of refraction waves. The USSR Academy of Science, Moscow (in Russain).

Garotta, R. 1999, Shear waves from acquisition to interpretation: Society of Exploration Geophysicists.

Gendzwill, D. 1990, High-resolution seismic reflections in an underground mine, SEG Technical Program Expanded Abstracts 1990: Society of Exploration Geophysicists. 397-398.

Goleby, B., R. Korsch, T. Fomin, B. Bell, M. Nicoll, B. Drummond, and A. Owen. 2002, Preliminary 3–D geological model of the Kalgoorlie region, Yilgarn Craton, Western Australia, based on deep seismic-reflection and potential-field data. Australian Journal of Earth Sciences, 49, no. 6,917-933.

Green, A., and J. Mair. 1983, Subhorizontal fractures in a granitic pluton: Their detection and implications for radioactive waste disposal. Geophysics, 48, no. 11,1428-1449.

Greenhalgh, S., B. Zhou, and S. Cao. 2003, A crosswell seismic experiment for nickel sulphide exploration. Journal of Applied Geophysics, 53, no. 2-3,77-89.

Greenhalgh, S. A., I. M. Mason, and C. Sinadinovski. 2000, In-mine seismic delineation of mineralization and rock structure. Geophysics, 65, no. 6,1908-1919.

Gustavsson, M., H. Israelson, S. Ivansson, P. Moren, and J. Pihl. 1984, An experiment with the seismic crosshole method in an iron mine. The Leading Edge, 3, no. 11,143-145.

Hardage, B. A., M. V. DeAngelo, P. E. Murray, and D. Sava. 2011, Multicomponent seismic technology: Society of Exploration Geophysicists.

Hardage, B. A., and D. Wagner. 2014, Generating direct-S modes with simple, low-cost, widely available seismic sources. Interpretation, 2, no. 2,SE1-SE15.

Harman, P., L. Leung, and M. Downey. 1987, Cross-hole seismic survey for mineral exploration in the west Kimberley area, Western Australia. Exploration Geophysics, 18, no. 2,80-83.

Inazaki, T. 2012, Delineation of detailed structure in Holocene unconsolidated sediments using S-wave type Land Streamer. Paper read at 74th EAGE Conference and Exhibition-Workshops.

Juhlin, C. 1995, Imaging of fracture zones in the Finnsjön area, central Sweden, using the seismic reflection method. Geophysics, 60, no. 1,66-75.

Juhlin, C., S. Kashubin, J. Knapp, V. Makovsky, and T. Ryberg. 1995, EUROPROBE seismic reflectionprofiling in the Urals: The ESRU project.

Juhlin, C., J. Lindgren, and B. Collini. 1991, Interpretation of seismic reflection and borehole data from Precambrian rocks in the Dala Sandstone area, central Sweden. First Break, 9, no. 1,24-36.

Juhlin, C., and M. B. Stephens. 2006, Gently dipping fracture zones in Paleoproterozoic metagranite, Sweden: Evidence from reflection seismic and cored borehole data and implications for the disposal of nuclear waste. Journal of Geophysical Research: Solid Earth, 111, no. B9.

Kearey, P., M. Brooks, and I. Hill. 2013, An introduction to geophysical exploration: John Wiley & Sons.

Kelly, K., R. Ward, S. Treitel, and R. Alford. 1976, Synthetic seismograms: a finite-difference approach. Geophysics, 41, no. 1,2-27.

Krapf, C. B. E., M. X. Werner, M. J. Pawley, and S. O. c. McAvaney. 2016, Surface Geology of Six Mile Hill – Mineral Systems Drilling Program Special Map Series, 1:75 000 scale.: DIGIMAP 00088. Department of State Development, South Australia.

Krawczyk, C. M., U. Polom, S. Trabs, and T. Dahm. 2012, Sinkholes in the city of Hamburg—New urban shear-wave reflection seismic system enables high-resolution imaging of subrosion structures. Journal of Applied Geophysics, 78,133-143.

Levander, A. R. 1988, Fourth-order finite-difference P-SV seismograms. Geophysics, 53, no. 11,1425-1436.

MA Zai-Tian, C. J.-Z., WANG Jia-Lin, et al. 1997, Survey of Computational Geophysics. Shanghai. Tongji University Press.

MacBeth, C., and X.-Y. Li. 1996, Linear matrix operations for multicomponent seismic processing. Geophysical Journal International, 124, no. 1,189-208.

Mair, J., and A. Green. 1981, High-resolution seismic reflection profiles reveal fracture zones within a ‘homogeneous’ granite batholith. Nature, 294, no. 5840,439.

Malehmir, A., M. Bastani, C. M. Krawczyk, M. Gurk, N. Ismail, U. Polom, and L. Persson. 2013, Geophysical assessment and geotechnical investigation of quick-clay landslides–a Swedish case study. Near Surface Geophysics, 11, no. 3,341-350.

Malehmir, A., and G. Bellefleur. 2009, 3D seismic reflection imaging of volcanic-hosted massive sulfide deposits: Insights from reprocessing Halfmile Lake data, New Brunswick, Canada. Geophysics, 74, no. 6,B209-B219.

Malehmir, A., G. Bellefleur, and C. Müller. 2010, 3D diffraction and mode-converted scattering signatures of base metal deposits, Bathurst Mining Camp, Canada. first break, 28, no. 12,41-45.

Malehmir, A., R. Durrheim, G. Bellefleur, M. Urosevic, C. Juhlin, D. J. White, B. Milkereit, and G. Campbell. 2012a, Seismic methods in mineral exploration and mine planning: A general overview of past and present case histories and a look into the future. Geophysics, 77, no. 5,WC173-WC190.

Malehmir, A., C. Juhlin, C. Wijns, M. Urosevic, P. Valasti, and E. Koivisto. 2012b, 3D reflection seismic investigation for open-pit mine planning and exploration in the Kevitsa Ni-Cu-PGE deposit, northern Finland: Geophysics.

Malehmir, A., S. Wang, J. Lamminen, B. Brodic, M. Bastani, K. Vaittinen, C. Juhlin, and J. Place. 2015, Delineating structures controlling sandstone-hosted base-metal deposits using high-resolution multicomponent seismic and radio-magnetotelluric methods: a case study from Northern Sweden. Geophysical Prospecting, 63, no. 4,774-797.

Malinowski, M., and D. White. 2011, Converted wave seismic imaging in the Flin Flon mining camp, Canada. Journal of Applied Geophysics, 75, no. 4,719-730.

Matthews, L. 2002, Base metal exploration: Looking deeper and adding value with seismic data. Canadian Society of Exploration Geophysicists Recorder, 27,37-43.

Mavko, G., T. Mukerji, and J. Dvorkin. 2009, The rock physics handbook: Tools for seismic analysis of porous media: Cambridge university press.

Miles, D. R. 1988, Three-component seismic data: Researcher's toy or interpreter's tool? : The Leading Edge, 7, no. 11,28-31.

Milkereit, B., E. Berrer, A. R. King, A. H. Watts, B. Roberts, A. Erick, D. W. Eaton, J. Wu, and M. H. Salisbury. 2000, Development of 3-D seismic exploration technology for deep nickel-copper deposits—A case history from the Sudbury basin, Canada3-D Seismic Exploration Technology. Geophysics, 65, no. 6,1890-1899.

Milkereit, B., and D. Eaton. 1998, Imaging and interpreting the shallow crystalline crust. Tectonophysics, 286, no. 1-4,5-18.

Milkereit, B., D. Eaton, J. Wu, G. Perron, M. H. Salisbury, E. Berrer, and G. Morrison. 1996, Seismic imaging of massive sulfide deposits; Part II, Reflection seismic profiling. Economic Geology, 91, no. 5,829-834.

Milkereit, B., A. Green, and t. S. W. Group. 1992, Deep geometry of the Sudbury structure from seismic reflection profiling. Geology, 20, no. 9,807-811.

Mutyorauta, J. 1987, High resolution seismic reflection, an exploration tool within an underground environment (example from Zimbabwe). Journal of African Earth Sciences (1983), 6, no. 1,109-115.

Muyzert, E. 2000, Scholte wave velocity inversion for a near surface S-velocity model and PS-statics, SEG Technical Program Expanded Abstracts 2000: Society of Exploration Geophysicists. 1197-1200.

Nelson, R. 1984, Seismic reflection and mineral prospecting. Exploration Geophysics, 15, no. 4,229-250.

Noponen, I., P. Heikkinen, and S. Mehrotra. 1979, Applicability of seismic reflection sounding in regions of Precambrian geology. Geoexploration, 17, no. 1,1-9.

Parker, A. J. F., R. B.; Daly, S. J.; Crooks, A. F.; Fairclough, M. C.; Jagodzinski, E. A. . 2005, YARDEA, South Australia. Sheet SI/53-3, International Index. 1:250 000 Geological Series - Explanatory Notes. Geological Survey of South Australia.

Perron, G., D. Eaton, B. Elliot, and D. Schmitt. 2003, Application of downhole seismic imaging to map near-vertical structures: Normétal (Abitibi Greenstone Belt), Québec. Hard rock seismic exploration: SEG,194-206.

Peterson, J. E., B. N. Paulsson, and T. V. McEvilly. 1985, Applications of algebraic reconstruction techniques to crosshole seismic data. Geophysics, 50, no. 10,1566-1580.

Polom, U., L. Hansen, G. Sauvin, J.-S. L'Heureux, I. Lecomte, C. M. Krawczyk, M. Vanneste, O. Longva, R. Miller, and J. Bradford. 2010, High-resolution SH-wave seismic reflection for characterization of onshore ground conditions in the Trondheim harbor, central Norway, Advances in near-surface seismology and ground-penetrating radar: Society of Exploration Geophysicists, American Geophysical Union, Environmental and Engineering Geophysical Society. 297-312.

Postma, G. 1955, Wave propagation in a stratified medium. Geophysics, 20, no. 4,780-806.

Pretorius, C., M. Gibson, and Q. Snyman. 2011, Development of high resolution 3D vertical seismic profiles. Journal of the Southern African Institute of Mining and Metallurgy, 111, no. 2,117-125.

Pretorius, C., A. Jamison, and C. Irons. 1989, Seismic exploration in the Witwatersrand basin, Republic of South Africa. Paper read at Proceedings of Exploration.

Pretorius, C., M. Muller, M. Larroque, and C. Wilkins. 2003, A review of 16 years of hardrock seismics on the Kaapvaal Craton, Hardrock seismic exploration: Society of Exploration Geophysicists. 247-268.

Pretorius, C. C., and W. F. Trewick. 1997, Application of 3D seismics to mine planning at Vaal Reefs Gold Mine, number 10 shaft, Republic of South Africa. Proceedings of Exploration 97, Fourth Decennial Interna- tional Conference on Mineral Exploration, Prospecting and Development Associates of Canada,399–408.

Price, T. O. 1974, Acoustical holography as a tool for geologic prediction. Paper read at Subsurface exploration for underground excavation and heavy construction.

Prodehl, C., and W. D. Mooney. 2012, Exploring the Earth's crust: history and results of controlled-source seismology. Vol. 208: Geological Society of America.

Pugin, A.-M., K. Brewer, T. Cartwright, S. E. Pullan, D. Perret, H. Crow, and J. A. Hunter. 2013, Near surface S-wave seismic reflection profiling–new approaches and insights. First Break, 31, no. 2,49-60.

Pugin, A. J., S. E. Pullan, and J. A. Hunter. 2010, Update on recent observations in multi-component seismic reflection profiling. Paper read at 23rd EEGS Symposium on the Application of Geophysics to Engineering and Environmental Problems.

Pugin, A. J.-M., S. E. Pullan, and J. A. Hunter. 2009, Multicomponent high-resolution seismic reflection profiling. The Leading Edge, 28, no. 10,1248-1261.

Pujol, J. 2003, Elastic wave propagation and generation in seismology: Cambridge University Press.

Reid, A. J., and M. Hand. 2012, Mesoarchean to mesoproterozoic evolution of the southern Gawler Craton, South Australia. Episodes, 35, no. 1,216-225.

Rüger, A. 1997, P-wave reflection coefficients for transversely isotropic models with vertical and horizontal axis of symmetry. Geophysics, 62, no. 3,713-722.

Salisbury, M. H., C. W. Harvey, L. Matthews, D. Eaton, and B. Milkereit. 2003, The acoustic properties of ores and host rocks in hardrock terranes. Hardrock seismic exploration, 10,9-19.

Schafer, A. W. 1993, Binning, static correction, and interpretation of P-SV surface-seismic data: Calgary.

Schmidt, G. 1959, Results of underground-seismic reflection investigations in the siderite district of the Siegerland. Geophysical Prospecting, 7, no. 3,287-290.

Schodde, R. 2017, Challenges of Exploring Under Deep Cover. AMIRA International's 11th Biennial Exploration Managers Conference 28th – 31st March 2017, Healesville Australia.

Schoenberg, M., and J. Protazio. 1990, “Zoeppritz” rationalized, and generalized to anisotropic media. The Journal of the Acoustical Society of America, 88, no. S1,S46-S46.

Shearer, P. M. 2009, Introduction to seismology: Cambridge University Press.

Sheriff, R. E. 2002, Encyclopedic dictionary of applied geophysics: Society of exploration geophysicists.

Shuck, E. L. 1993, Multicomponent, three-dimensional seismic characterization of a fractured coalbed methane reservoir, Cedar Hill Field, San Juan County, New Mexico. Colorado School of Mines, Golden, CO (United States).

Shuck, E. L., T. L. Davis, and R. D. Benson. 1996, Multicomponent 3-D characterization of a coalbed methane reservoir. Geophysics, 61, no. 2,315-330.

Shuey, R. 1985, A simplification of the Zoeppritz equations. Geophysics, 50, no. 4,609-614.

Sinadinovski, C., S. A. Greenhalgh, and l. Mason. 1995, Three-dimensional reflector imaging of in-mine high frequency crosshole seismic data. Exploration Geophysics, 26, no. 2/3,325-330.

Snyder, D. B., P. Cary, and M. Salisbury. 2009, 2D-3C high-resolution seismic data from the Abitibi Greenstone Belt, Canada. Tectonophysics, 472, no. 1-4,226-237.

Spathis, A., D. Blair, and J. Grant. 1985, Seismic pulse assessment of the changing rock mass conditions induced by mining. Paper read at International Journal of Rock Mechanics and Mining Sciences & Geomechanics Abstracts.

Stewart, R. R. 2009, The measure of full motion: multicomponent seismic exploration and its value, SEG Technical Program Expanded Abstracts 2009: Society of Exploration Geophysicists. 4243-4248.

Stewart, R. R., J. E. Gaiser, R. J. Brown, and D. C. Lawton. 2002, Converted-wave seismic exploration: Methods. Geophysics, 67, no. 5,1348-1363.

Stewart, R. R., J. E. Gaiser, R. J. Brown, and D. C. Lawton. 2003, Converted-wave seismic exploration: Applications. Geophysics, 68, no. 1,40-57.

Stolz, E., M. Urosevic, and K. Connors. 2004, Reflection seismic surveys at St Ives gold mine, WA. ASEG Extended Abstracts, 2004, no. 1,1-4.

Tertyshnikov, K. 2014, Seismic imaging in hard rock environments, Curtin University.

Tessmer, G., and A. Behle. 1988, Common reflection point data-stacking technique for converted waves. Geophysical prospecting, 36, no. 7,671-688.

Thomsen, L. 1986, Weak elastic anisotropy. Geophysics, 51, no. 10,1954-1966.

Thomsen, L. 1988, Reflection seismology over azimuthally anisotropic media. Geophysics, 53, no. 3,304-313.

Thomsen, L. 1999, Converted-wave reflection seismology over inhomogeneous, anisotropic media. Geophysics, 64, no. 3,678-690.

Thomsen, L. A. 1990, Method of seismic surveying for resolving the effects of formation anisotropy in shear wave reflection seismic data. Google Patents.

Tsvankin, I. 2012, Seismic signatures and analysis of reflection data in anisotropic media: Society of Exploration Geophysicists.

Urosevic, M. 2000, A study of seismic wave propagation as applied to seismic imaging in the southern Sydney basin: Curtin University of Technology.

Urosevic, M. 2013, What can seismic in hard rocks do for you? : ASEG Extended Abstracts, 2013, no. 1,1-4.

Urosevic, M., G. Bhat, and M. H. Grochau. 2012, Targeting nickel sulfide deposits from 3D seismicreflection data at Kambalda, Australia. Geophysics, 77, no. 5,WC123-WC132.

Urosevic, M., A. Bona, S. Ziramov, R. Pevzner, A. Kepic, A. Egorov, J. Kinkela, D. Pridmore, and J. Dwyer. 2017, Seismic for mineral resources – a mainstream method of the future. Exploration ’17, DMEC Decennial Mineral Exploration Conferences.

Urosevic, M., and B. Evans. 1996, The role of three-component surface seismic in long-wall mine planning, SEG Technical Program Expanded Abstracts 1996: Society of Exploration Geophysicists. 642-645.

Urosevic, M., and B. Evans. 2000, Surface and borehole seismic methods to delineate kimberlite pipes in Australia. The Leading Edge, 19, no. 7,756-758.

Urosevic, M., and B. J. Evans. 1998, Seismic methods for the detection of kimberlite pipes. Exploration Geophysics, 29, no. 4,632-635.

Urosevic, M., A. Kepic, E. Stolz, C. Juhlin, and B. Milkereit. 2007, Seismic exploration of ore deposits in Western Australia. Paper read at Exploration in the new millennium: Proceedings of the Fifth Decennial International Conference on Mineral Exploration.

Urosevic, M., and J. McDonald. 1985, Physical modeling of anisotropic media, SEG Technical Program Expanded Abstracts 1985: Society of Exploration Geophysicists. 369-372.

Urosevic, M., S. Sheppard, D. Johnson, and A. Kepic. 2009, Seismic Exploration of Nickel Deposits – Lake Lefroy, Kambalda, WA. In 20th International Geophysical Conference and Exhibition, Adelaide, Australia.

Urosevic, M., N. Stoltz, and S. Massey. 2005, Seismic Exploration for Gold in a Hard Rock Environment–Yilgarn Craton, Western Australia. Paper read at 67th EAGE Conference & Exhibition.

Vavryčuk, V., and I. Pšenčik. 1998, PP-wave reflection coefficients in weakly anisotropic elastic media. Geophysics, 63, no. 6,2129-2141.

Virieux, J. 1986, P-SV wave propagation in heterogeneous media: Velocity-stress finite-difference method. Geophysics, 51, no. 4,889-901.

White, D., D. Secord, and M. Malinowski. 2012, 3D seismic imaging of volcanogenic massive sulfide deposits in the Flin Flon mining camp, Canada: Part 1—Seismic results. Geophysics, 77, no. 5,WC47-WC58.

Williams, N., R. Lane, and P. Lyons. 2004, Regional constrained 3D inversion of potential field data from the Olympic Cu-Au province, South Australia. Preview, 109,30-33.

Wong, J. 2000, Crosshole seismic imaging for sulfide orebody delineation near Sudbury, Ontario, Canada. Geophysics, 65, no. 6,1900-1907.

Wong, J., P. Hurley, and G. West. 1983, Crosshole seismology and seismic imaging in crystalline rocks. Geophysical Research Letters, 10, no. 8,686-689.

Wong, J., P. Hurley, and G. West. 1984, Crosshole audiofrequency seismology in granitic rocks using piezoelectric transducers as sources and detectors. Geoexploration, 22, no. 3-4,261-279.

Xu, K., and S. Greenhalgh. 2010, Ore-body imaging by crosswell seismic waveform inversion: A case study from Kambalda, Western Australia. Journal of Applied Geophysics, 70, no. 1,38-45.

XU, S. Y., and Z. T. MA. 2002, A fast and efficient common conversion point stacking technique for converted waves. Chinese Journal of Geophysics, 45, no. 4,580-592.

Yilmaz, Ö. 2001, Seismic data analysis: Processing, inversion, and interpretation of seismic data: Society of exploration geophysicists.

Zhang, Y., and E. A. Robinson. 1992, Stacking P-SV converted wave data with raypath velocity, SEG Technical Program Expanded Abstracts 1992: Society of Exploration Geophysicists. 1214-1217.

Zoeppritz, K. 1919, On the reflection and propagation of seismic waves at discontinuities. Erdbebenwellen VII B,66-84.

Every reasonable effort has been made to acknowledge the owners of copyright material. I would be pleased to hear from any copyright owner who has been omitted or incorrectly acknowledged.